

University of Nebraska - Lincoln

DigitalCommons@University of Nebraska - Lincoln

---

Theses, Dissertations, and Student Research from  
Electrical & Computer Engineering

Electrical & Computer Engineering, Department of

---


12-2010

# Generalized Ellipsometry on Sculptured Thin Films made by Glancing Angle Deposition

Daniel Schmidt

University of Nebraska-Lincoln, [schmidt@huskers.unl.edu](mailto:schmidt@huskers.unl.edu)

Follow this and additional works at: <http://digitalcommons.unl.edu/elecengtheses>

 Part of the [Electromagnetics and Photonics Commons](#), [Nanoscience and Nanotechnology Commons](#), and the [Nanotechnology Fabrication Commons](#)

---

Schmidt, Daniel, "Generalized Ellipsometry on Sculptured Thin Films made by Glancing Angle Deposition" (2010). *Theses, Dissertations, and Student Research from Electrical & Computer Engineering*. 15.  
<http://digitalcommons.unl.edu/elecengtheses/15>

This Article is brought to you for free and open access by the Electrical & Computer Engineering, Department of at DigitalCommons@University of Nebraska - Lincoln. It has been accepted for inclusion in Theses, Dissertations, and Student Research from Electrical & Computer Engineering by an authorized administrator of DigitalCommons@University of Nebraska - Lincoln.

# **Generalized Ellipsometry on Sculptured Thin Films made by Glancing Angle Deposition**

by

Daniel Schmidt

A DISSERTATION

Presented to the Faculty of  
The Graduate College at the University of Nebraska  
In Partial Fulfillment of Requirements  
For the Degree of Doctor of Philosophy

Major: Interdepartmental Area of Engineering  
(Electrical Engineering)

Under the Supervision of Professors Eva Schubert and Mathias Schubert

Lincoln, Nebraska

December 2010

# Generalized Ellipsometry on Sculptured Thin Films made by Glancing Angle Deposition

Daniel Schmidt, PhD  
University of Nebraska, 2010

Advisers: Eva Schubert and Mathias Schubert

In this thesis, physical properties of highly optically and magnetically anisotropic metal sculptured thin films made by glancing angle deposition are presented. Predominantly, the determination of optical and magneto-optical properties with spectroscopic generalized Mueller matrix ellipsometry and homogenization approaches is discussed. Nomenclatures are proposed to unambiguously identify the sculptured thin film geometry.

Generalized ellipsometry, a non-destructive optical characterization technique, is employed to determine geometrical structure and anisotropic dielectric properties of highly spatially coherent three-dimensionally nanostructured thin films in the spectral range from 400 to 1700 nm. The analysis of metal slanted columnar thin films (F1-STFs) deposited at glancing angle ( $\theta_i = 85^\circ$ ) revealed monoclinic optical properties of such nanostructures, and the optical response can be modeled with a single homogeneous biaxial layer. This homogeneous biaxial layer approach is universally applicable to F1-STFs and effective optical properties of the nanostructured thin films are attained.

More complex sculptured thin films, which can be engineered by a dynamic in-situ substrate rotation, may be considered as cascaded F1-STFs. A piecewise homogeneous biaxial layer approach is described, which allows for the determination of principal optical constants of chiral multi-fold and helical sculptured thin films. For optical analysis, complex sculptured thin films can be virtually separated into their F1-STF building blocks. It is confirmed that such sculptured thin films have modular optical properties. This characteristic can be exploited to predict the optical response of sculptured thin films grown with arbitrary sequential substrate rotations.

Magneto-optical generalized ellipsometry in the polar and longitudinal Kerr geometry is utilized to determine the spectral magneto-optical response of Co F1-STFs and estimate the magnetization direction. Kerr effect measurements and calculations reveal a strong azimuthal dependence with peak Kerr rotation one order of magnitude larger than what has been reported for solid Co thin films. The concept of generalized ellipsometry in conjunction with a three-dimensional vector magnet is introduced and first measurement results presented.

## Acknowledgements

I am greatly indebted to my advisers Dr. Eva Schubert and Dr. Mathias Schubert for educating, encouraging, and challenging me, for many helpful discussions, suggestions, and manifold support throughout the course of this work.

I would like to thank Dr. Tino Hofmann for many enlightening discussions, for sharing his experimental expertise, and for his diverse support within the last four years.

Further, I would like to thank Dr. Natale Ianno and Dr. Sy-Hwang Liou for serving as committee members.

I am indebted to Dr. Olle Inganäs for his kind invitation to Linköping University, Sweden. Especially, I would like to thank Dr. Christian Müller for sparing no efforts in supporting the hybridization experiments. Many thanks also to Dr. Hans Arwin for providing measurement time, for helpful discussions, and support in Linköping. I am thankful for the nice hospitality and all people adding to that.

I would like to thank very much

- Dr. John Woollam and the J. A. Woollam Company for very generous instrumental support and especially Dr. Craig Herzinger for customizing the analysis software and many helpful discussions,
- Benjamin Booso and Dr. Andrew Sarangan for the great collaboration,
- Dr. Ralf Skomski for many helpful discussions with respect to magnetic properties of nanostructures,
- Dr. Beri Mbenkum and Dr. Thomas Oates for providing prepatterned substrates,
- Kah Mok and Dr. Heidemarie Schmidt for conducting VMOGE measurements,
- Dr. Han Chen for his help with the scanning electron microscope,

- the UNL Chemistry/Physics & Astronomy Instrument Shop for manufacturing parts,
- and my colleagues Dr. Mario Saenger, Venkata Voora, Brian Rodenhäusen, Stefan Schöche, Eric Montgomery, Philipp Kühne, Brian Bell, Ann Kjerstad, Alex Boosalis, and Dr. Ravi Billa for many helpful discussions, diverse support, and many nice hours!

Finally, I would like to thank Veronica Barra and my parents, Ria and Günter Schmidt, for their encouragement, love, and support during the past four years while I was working on this thesis. Thank you!

# Contents

<b>Abstract</b>	<b>ii</b>
<b>Acknowledgements</b>	<b>iii</b>
<b>List of Symbols and Acronyms</b>	<b>ix</b>
<b>1 Introduction</b>	<b>1</b>
<b>2 Fabrication of Sculptured Thin Films</b>	<b>5</b>
2.1 Glancing Angle Deposition . . . . .	5
2.1.1 Organized In-plane Growth . . . . .	7
2.1.2 Proposed Sculptured Thin Film Nomenclature . . . . .	9
2.2 Ultrahigh Vacuum Glancing Angle Deposition System . . . . .	9
2.2.1 Design Considerations . . . . .	9
2.2.2 Deposition System . . . . .	10
2.2.2.1 Load-lock Chamber and Sample Transfer System . . . . .	12
2.2.2.2 Deposition Chamber . . . . .	12
2.2.2.3 Electron-beam Evaporation System . . . . .	13
2.2.2.4 Sample Manipulator . . . . .	14
2.2.2.5 Deposition Controller . . . . .	16
<b>3 Characterization Methods</b>	<b>17</b>
3.1 Structural Properties . . . . .	17
3.1.1 Scanning Electron Microscopy . . . . .	17
3.1.2 X-ray Diffraction . . . . .	18
3.2 Spectroscopic Ellipsometry . . . . .	19
3.2.1 Definition of the Optical Constants . . . . .	20
3.2.2 Jones and Mueller Matrix Presentation . . . . .	21
3.2.3 Generalized Ellipsometry . . . . .	24

---

3.2.4	Anisotropic Dielectric Function Tensor . . . . .	24
3.2.4.1	General Description . . . . .	24
3.2.4.2	Orthogonal Rotations . . . . .	25
3.2.4.3	Bond Polarizability Model . . . . .	25
3.2.4.4	Connection between Intrinsic Polarizabilities and Di- electric Tensor . . . . .	30
3.2.5	Light Propagation in Layered Anisotropic Media . . . . .	31
3.2.6	Ellipsometry Model Description for Sculptured Thin Films . . .	34
3.2.6.1	Homogeneous Biaxial Layer Approach . . . . .	34
3.2.6.2	Anisotropic Bruggeman Effective Medium Approximation	35
3.2.6.3	Piecewise Homogeneous Biaxial Layer Approach . . . . .	37
3.2.7	Ellipsometry Data Analysis . . . . .	39
3.2.7.1	Wavelength-by-Wavelength Analysis . . . . .	39
3.2.7.2	Parameterized Model Dielectric Function Analysis . . .	40
3.2.7.3	Ellipsometry Test Functions . . . . .	41
3.2.7.4	Multi-Sample and Multi-Sample-Configuration Analysis	42
3.2.7.5	Difference Spectra Analysis . . . . .	43
3.2.8	Experimental Setup . . . . .	43
3.3	Magneto-Optical Generalized Ellipsometry . . . . .	44
3.3.1	Magneto-Optical Dielectric Tensor . . . . .	45
3.3.2	Primary Magneto-Optical Effects . . . . .	45
3.3.3	Kerr Rotation and Kerr Ellipticity . . . . .	47
3.3.4	Magneto-Optical Generalized Ellipsometry Model Description . .	47
3.3.5	Experimental Setup . . . . .	47
3.3.5.1	Magneto-Optical Kerr-Effect Configuration . . . . .	47
3.3.5.2	Octupole Vector-Magnet Setup . . . . .	49
<b>4</b>	<b>Experimental Parameters</b>	<b>52</b>
4.1	Sculptured Thin Film Deposition . . . . .	52
4.2	Hybridization . . . . .	53
4.3	Generalized Ellipsometry . . . . .	53
<b>5</b>	<b>Structural Properties of Metal Sculptured Thin Films</b>	<b>55</b>
5.1	Scanning Electron Microscopy Micrograph Analysis . . . . .	55
5.1.1	Flat Substrates . . . . .	55
5.1.2	Prepatterned Substrates . . . . .	57

---

5.2	Column Tilt Evaluation . . . . .	57
5.3	Determination of Structural Parameters by Ellipsometry Data Analysis . . . . .	58
5.4	X-ray Diffraction Analysis . . . . .	59
5.5	Summary . . . . .	60
<b>6</b>	<b>Optical Properties of Metal Sculptured Thin Films</b> . . . . .	<b>61</b>
6.1	Monoclinicity of Metal F1-STFs . . . . .	61
6.1.1	Optical Constants . . . . .	62
6.1.2	Monoclinicity . . . . .	66
6.1.3	Summary . . . . .	67
6.2	Universality of Metal F1-STFs . . . . .	67
6.2.1	Titanium F1-STFs . . . . .	68
6.2.2	Superalloy (Ni <sub>80</sub> Fe <sub>15</sub> Mo <sub>5</sub> ) F1-STFs . . . . .	69
6.2.3	Summary . . . . .	72
6.3	Modularity of Complex Sculptured Thin Films . . . . .	73
6.3.1	Chevron-like Sculptured Thin Films (2F2-STFs) . . . . .	73
6.3.2	L-shape Sculptured Thin Films (2F4-STFs) . . . . .	76
6.3.3	U-shape Sculptured Thin Films (3F4-STFs) . . . . .	79
6.3.4	Helical Sculptured Thin Films (H-STFs) . . . . .	82
6.3.5	Summary . . . . .	87
6.4	Host Variation . . . . .	87
6.4.1	Environmental Influences . . . . .	87
6.4.2	Hybridization by Polymer Infiltration . . . . .	88
6.4.3	Summary . . . . .	92
6.5	Effective Medium Approximations for F1-STFs . . . . .	93
6.5.1	Cobalt F1-STF . . . . .	93
6.5.2	Titanium F1-STF . . . . .	95
6.5.3	Superalloy F1-STF . . . . .	95
6.5.4	Summary . . . . .	97
6.6	Literature Discussion . . . . .	97
6.6.1	Early Optical Investigations on Sculptured Thin Films . . . . .	97
6.6.2	Effective Medium Approximations for F1-STFs . . . . .	98
6.6.3	Optical Properties of Complex and Hybrid STF's . . . . .	99



---

<b>7 Magneto-Optical Properties of Co F1-STFs</b>	<b>101</b>
7.1 Polar Kerr Effect Geometry . . . . .	101
7.1.1 Experiment . . . . .	101
7.1.2 Giant Magneto-Optical Polarizability . . . . .	102
7.1.3 Giant Kerr Rotation . . . . .	104
7.2 Longitudinal Kerr Effect Geometry . . . . .	104
7.2.1 Experiment . . . . .	104
7.2.2 Estimation of Magnetization Direction . . . . .	105
7.3 Octupole Vector-Magnet . . . . .	108
7.3.1 Experiment . . . . .	109
7.3.2 Results . . . . .	110
7.4 Summary . . . . .	111
7.5 Literature Discussion . . . . .	112
<b>8 Summary and Outlook</b>	<b>114</b>
<b>References</b>	<b>117</b>
<b>List of Own Publications</b>	<b>127</b>

# List of Symbols and Acronyms

## Roman Symbols

<b>A</b>	unitary rotation matrix
<b>a, b, c</b>	major polarizability axes
<b>A, B</b>	incident and emergent plane wave components
<b>A<sub>j</sub></b>	amplitude of the <i>j</i> th oscillator
<b>C</b>	covariance matrix
<b>c<sub>t</sub></b>	continuous rotation time (deposition)
<b>D</b>	displacement
<b>d</b>	thickness
<b>D<sub>P</sub></b>	degree of polarization
<b>E</b>	electric field
<b>E<sub>c</sub></b>	center energy
<b>f</b>	frequency
<b>f<sub>U</sub>, f<sub>L</sub></b>	frequency of loaded and unloaded quartz crystal
<b>f<sub>v</sub></b>	void fraction (EMA theories)
<b>H</b>	magnetic field
<b>I</b>	intensity
<b>J</b>	Jones matrix
<b>k</b>	wavevector

---

$k$	extinction coefficient
$\mathbf{L}_a, \mathbf{L}_f$	ambient and exit partial transfer matrix
$L$	confidence limit
$L_j^D$	depolarization factor along $j$ (EMA theories)
$\mathcal{M}$	magnetization
$\mathbf{M}$	Mueller matrix
$m_j$	magnetization dependent component along $j$
$m_{\text{eff}}$	electron effective mass
$m_{j0}$	offset parameter along $j$
$N$	complex-valued refractive index
$n$	refractive index
$N_V$	volume-density
$N_M, S_M, C_M$	isotropic Mueller matrix quantities
$\mathbf{P}$	polarization field
$P$	pitch
$P_a$	absolute pressure
$p_t$	pause time (deposition)
$q$	elementary charge
$q_k$	eigenvalues
$r_t$	stepwise rotation time (deposition)
$R_{ij}$	reflectivities
$r_{ij}$	anisotropic Fresnel reflection coefficient
$S_j$	Stokes vector element
$\mathbf{T}$	transfer matrix

---

$\mathbf{T}_p$	partial transfer matrix
$\mathbf{U}$	direct structure (projection) matrix
$x, y, z$	Cartesian coordinates
$Z$	$Z$ -ratio

### Greek Symbols

$\alpha'$	absorption coefficient
$\alpha, \beta, \gamma$	unit cell angles
$\boldsymbol{\alpha}$	curvature matrix
$\Delta$	delta matrix
$\boldsymbol{\varepsilon}$	dielectric function tensor
$\varepsilon_0$	vacuum permittivity
$\varepsilon_j$	major dielectric function along $j$
$\varepsilon_K$	Kerr ellipticity
$\varepsilon_{\text{off}}$	offset parameter
$\eta$	parameter correlation coefficients
$\gamma$	broadening
$\mu$	free-charge carrier mobility
$\mu_q$	shear modulus of quartz crystal
$\omega$	angular frequency
$\phi$	sample in-plane (azimuthal) angle
$\phi_m$	azimuth angle of magnetic field direction (VMOGE)
$\varphi, \theta, \psi$	Euler angles
$\Phi_a$	(ambient) angle of incidence

---

$\Psi, \Delta$	ellipsometric parameters
$\rho$	ellipsometric ratio
$\rho_q$	density of quartz crystal
$\theta_B$	Bragg angle
$\varrho_j$	major polarizability along $j$
$\sigma$	standard deviation
$\sigma+, \sigma-$	right- and left-handed circularly polarized light
$\sigma_0$	DC conductivity
$\tau$	relaxation time
$\theta_i$	incident particle flux
$\theta_m$	polar angle of magnetic field direction (VMOGE)
$\theta_K$	Kerr rotation
$\theta_{j0}$	offset parameter along $j$
$\chi$	susceptibility tensor
$\Xi$	electromagnetic eigenmodes
$\xi$	mean square error
$\varnothing_h$	radius of helix

### Operators

$\{\cdot\}^*$	complex conjugate
$\text{Im}\{\cdot\}$	imaginary part of
$\{\cdot\}^{-1}$	inverse
$\text{Re}\{\cdot\}$	real part of
$\{\cdot\}^T$	transpose

**Acronyms**

AB-EMA	anisotropic Bruggeman effective medium approximation
CCD	charge-coupled device
DC	direct current
EMA	effective medium approximation
FE	field emission
GE	generalized ellipsometry
GLAD	glancing angle deposition
hcp	hexagonal close-packed
MDF	model dielectric function
MOGE	magneto-optical generalized ellipsometry
MOKE	magneto-optical Kerr effect
MSE	mean square error
P3DDT	poly(3-dodecylthiophene)
PVD	physical vapor deposition
SEM	scanning electron microscopy
SE	spectroscopic ellipsometry
STF	sculptured thin film
UHV	ultrahigh vacuum
VMOGE	vector magneto-optical generalized ellipsometry
WBW	wavelength-by-wavelength
XRD	x-ray diffraction

# Chapter 1

## Introduction

Nanotechnology in the 21st century enabled revolutions in the fields of information technology, cellular, and molecular biology with profound impact on our economy and society. Progress in the interdisciplinary field of nanotechnology allowed for miniaturization of electronic components leading to portability of affordable products with improved functionality. Engineering research in nanotechnology provided and continues to provide the key component for further technological enhancements.

Today's nanotechnology is mostly a planar (two-dimensional) technology. Another technology leap is foreseen with appropriate utilization of the third dimension employing self-assembled nanostructures as building blocks. Sophisticated techniques and growth processes lead to self-organized three-dimensional nanostructures and novel materials and phenomena are incorporated into next generation micro- and nanosystems. The fabrication of metallic nanostructures with tailored geometry and material is one of the central challenges of nanotechnology because geometrical and material parameters are responsible for the optical, electrical, mechanical, chemical, or magnetic properties of such structures.

Amongst the emerging technologies for fabrication of metallic nanostructures is a physical vapor deposition process called glancing angle deposition. The particular growth geometry combined with dynamic substrate movement allows for in-situ sculpturing of self-organized highly spatially coherent three-dimensional achiral and chiral geometries at the nanoscale from virtually any material. Such engineered nanostructured materials, termed sculptured thin films, constitute a new realm of solid state materials, and carry a huge potential for applications in the fields of nano-photonics<sup>1</sup>, nano-electromechanics<sup>2</sup>, nano-magnetics<sup>3</sup>, nano-electromagnetics<sup>4</sup>, and nano-sensors<sup>5,6</sup>. For example, tailored effective optical constants by controlling porosity and shape of the nanostructured films are highly desirable for many applications such as broadband antireflection coatings<sup>7,8</sup>, omnidirectional reflectors<sup>9,10</sup>, Bragg reflectors<sup>11,12</sup>, optical

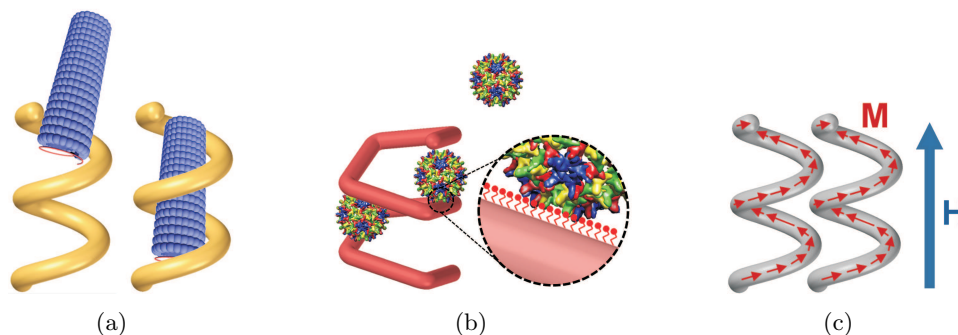


**Figure 1.1:** Schematic illustration of novel application areas for sculptured thin films in sensing and detection, and nanomagnetism: (a) selective capsid (protein shell of virus) capturing in hollow-core nanohelices with matched dimensions, (b) viral attachment on bio-functionalized nanoscaffold surfaces, and (c) chiral magnetic domain alignment in ferromagnetic nanohelices [Capsid in (a) modified from<sup>23</sup>, and Hepatitis B virus in (b) adapted from<sup>24</sup>].

resonators<sup>13</sup>, light emitting diodes<sup>14</sup>, and optical interconnects<sup>15</sup>. The controllable porosity and the large surface area may also be considerably beneficial for existing technologies such as solar cells<sup>16,17,18</sup> and thin film batteries<sup>19</sup>. Ferromagnetic sculptured thin films, in particular, exhibit interesting magnetic phenomena due to anisotropic structure effects and hence can be exploited for new magnetic or magneto-optical storage media<sup>20</sup>.

An entire new material class is envisioned when combining the inorganic nanostructures with functionalized polymers or chemical and biological recognition elements thereby creating nanohybrid functional materials. The new nanohybrids are anticipated to offer unmatched tunability in terms of electronic, optical, mechanical, ferroelectric, magnetic, and magneto-optical properties, thereby opening the door to a new family of sensing principles and, ultimately, new classes of ultra sensitive, broad range, portable, inexpensive sensors and detectors<sup>21,22</sup>.

Figure 1.1 depicts conceptualized areas of interest for sculptured thin films. Hollow-core nanohelices fabricated with an inner diameter matching dimensions of helical viral protein shells (capsids with typical diameters in the range of 5 to 30 nm) may become useful for purification and detection. Nanostructure surfaces can be coated with self-assembled monolayers and functional groups to facilitate viral attachment. The adsorbed biomaterial will change the anisotropic optical response of the functionalized hybrid nanostructures and can be detected by spectroscopic ellipsometry, for example. Nanomagnetism and the arrangement and switching of chiral magnetic fields is in the scope of interest also because ferromagnetic nanostructures might have the ability,



upon application of external magnetic fields, to control capture or release of modified adsorbates.

In order to systematically utilize sculptured thin films in future applications, however, physical properties of these nanosized objects need to be understood such that targeted geometry engineering with tailored properties from desired materials will be possible. Non-invasive and non-destructive optical techniques are preferred, however, due to the complexity of sculptured thin films, optical characterization is a challenge. Spectroscopic generalized ellipsometry within the Mueller matrix formalism is the most general polarization-dependent spectroscopic approach and an excellent tool to determine the dielectric function of complex optical systems. Generalized ellipsometry allows for characterization of sculptured thin films of arbitrary geometry and materials upon analyzing the anisotropic polarizability response. In conjunction with external magnetic fields and magnetized samples, magneto-optical generalized ellipsometry is capable of determining anisotropic magnetic and magneto-optical properties of sculptured thin films.

The present work elucidates fundamental optical and magneto-optical properties of complex sculptured thin films in the visible and near infrared spectral region and is organized as follows:

The physical vapor glancing angle deposition technique used for fabrication of the sculptured thin films is presented in Chap. 2. Furthermore, the chapter contains an extensive description of the in-house built deposition system and peripheral equipment.

Characterization techniques with a strong focus of spectroscopic generalized ellipsometry are presented in Chap. 3. Necessary mathematical formalisms to describe light propagation in stratified media are outlined and the treatment of the external electromagnetic plane wave response of an optical system using the Mueller matrix formalism is given here. Model approaches for analysis of ellipsometry data valid for complex sculptured thin films are discussed. Furthermore, the concept of magneto-optical generalized ellipsometry is presented and a novel octupole vector-magnet setup is introduced.

Chapter 4 summarizes the experimental parameters such as growth and measurement conditions for each sample. Selected structural properties of slanted columnar thin films (F1-STFs) from cobalt are discussed in Chap. 5.

Optical properties of metal sculptured thin films are discussed in Chap. 6. Metal F1-STFs are found to possess monoclinic optical properties. A model is proposed that explains the origin of the monoclinicity due to the specific spatial arrangement of the nanostructures. It is demonstrated that the homogeneous biaxial layer approach is an

universally valid approach for all F1-STFs. Subsequently, optical properties of more complex STFs are presented. It is discussed why the optical plane wave response of STFs can be reduced to the determination of the optical constants of the individual building blocks (F1-STFs). These building blocks can be assembled in a modular conception mimicking the true geometry, and the optical properties of the film can be predicted from this model arrangement. It is further discussed how optical properties of sculptured thin films are influenced upon ambient changes. Birefringence and dichroism changes are observed upon hybridization by infiltration of a conducting polymer into voids. The chapter ends with a comparison of results obtained with the homogeneous biaxial layer approach and anisotropic Bruggeman effective medium approximation calculations.

Experimental results of magneto-optical generalized ellipsometry in the traditional polar and longitudinal geometry are presented in Chap. 7. Giant Kerr rotation is measured for Co F1-STF and the combined measurements are used to predict the resulting sample magnetization direction upon application of an external magnetizing field. Preliminary vector-magneto-optical generalized ellipsometry investigations are discussed, which may give insight into domain switching behavior of complex STFs.

The present thesis is concluded with a summary of the fundamental findings and a brief outlook in Chap. 8.

## Chapter 2

# Fabrication of Sculptured Thin Films

### 2.1 Glancing Angle Deposition

Glancing angle deposition (GLAD) is a bottom-up fabrication technique that employs a physical vapor deposition (PVD) process at oblique angles where the trajectory of the incoming particle flux is not parallel to the substrate normal. The technique allows to engineer the columnar structure of PVD grown films and is today amongst the most promising self-organized fabrication processes in micro- and nanotechnology. The three-dimensionally shaped, highly orientationally coherent but randomly distributed nanostructured thin films are called sculptured thin films (STFs).

The first report on growth of metallic thin films by PVD at oblique angles with a stationary substrate was published more than 120 years ago. Kundt<sup>25</sup>, credited for growing the first slanted columnar thin films (F1-STFs, see Table 2.1), observed birefringence in his metal thin films and concluded that the optical anisotropy was due to the microstructure.

In 1950, König and Hellwig<sup>26</sup> recognized the self-shadowing mechanism responsible for a columnar microstructure developing during deposition at oblique angles. The incident atoms stochastically condense on the substrate and form nucleation clusters. At oblique angles, due to physical shadowing at the atomic scale, a competing three-dimensional growth of these clusters starts since no incoming particles can reach the geometrically shadowed area. Given favorable conditions, such as limited adatom mobility (surface diffusion) and collimated particle flux, the resulting thin film consists of self-organized, highly spatially coherent slanted nanocolumns. The columns are oriented toward the vapor source, however, the growth direction is not parallel to the incoming vapor flux but rather tilted toward the substrate normal<sup>27,28</sup>.

Another important step toward the emergence of three-dimensionally shaped thin films was reported by Young and Kowal<sup>29</sup> in 1959. The authors introduced a continuous

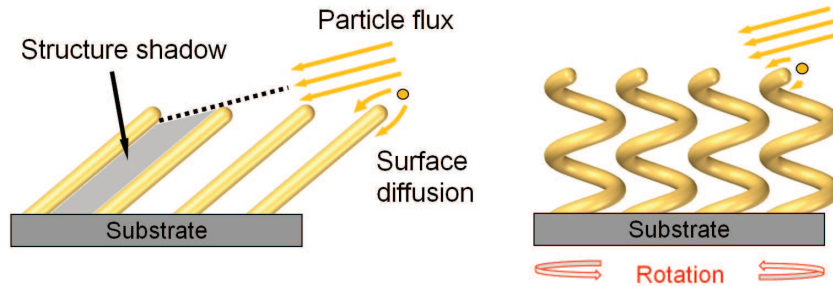


**Figure 2.1:** Schematic drawing of two representative GLAD situations in case of lateral ordering (deposited on patterned substrate). (left) With a steady substrate and an obliquely incident particle flux highly spatially coherent F1-STFs (slanted columns) will grow. (right) Slow and continuous substrate rotation, which is equivalent to a steady change in the direction of the incoming particle flux, results in H-STFs (hollow-core nanohelices).

substrate rotation around the substrate normal during deposition at incident angles of  $30^\circ < \theta_i < 60^\circ$  to realize chiral\* polarization filters. Substrate rotation is equivalent to a constant angular change of the incoming particle flux direction and hence equivalent to an apparent rotation of the vapor source around the substrate normal<sup>30,31</sup>. This changes the shadowing dynamics and the column growth follows the perceived change in source location.

Robbie *et al.*<sup>32</sup> demonstrated that at very oblique incident angles ( $\theta_i > 60^\circ$ ) highly porous nanostructured thin films can be fabricated with densities as low as 15% bulk and coined the term glancing angle deposition. At glancing angles of  $\theta_i > 80^\circ$  and in combination with a controlled substrate motion distinct nanostructures can be “sculpted” in-situ<sup>33</sup>. The GLAD process is schematically shown in Fig. 2.1.

Depending on the azimuthal substrate motion, different STF geometries and combinations thereof can be achieved: simple slanted columnar thin films (F1-STFs) will form at oblique angles with no substrate rotation. If the substrate is rotated stepwise at fixed growth intervals chevron-like (*IF2*-STFs;  $180^\circ$  steps)<sup>†</sup> or staircase-like with a square footprint (*IF4 $^\pm$* -STFs;  $90^\circ$  steps) can be fabricated, for example. Slow and continuous rotation will result in chiral hollow-core helical sculptured thin films (*tH $^\pm$* -STF) where the rotation speed determines the inner diameter of the H-STFs (Fig. 2.1). The pitch of the helices is a measure of the vertical periodicity and defined as the vertical distance between two adjacent windings. As the angular velocity of the sub-

\*The term chiral is derived from the Greek word for hand and is used to describe an object that is non-superposable on its mirror image.

<sup>†</sup>New nomenclatures are introduced for different sculptured thin film geometries. See Table 2.1.











strate rotation is increased the inner diameter and the pitch decreases until eventually solid-core screw-like structures will form. Yet faster rotation speed where the pitch becomes smaller than the column diameter will result macroscopically in the loss of the helical geometry, and the structure degenerates into vertically oriented columns (V-STFs)<sup>27,28</sup>. An additional degree of freedom can be introduced by also changing the deposition angle during growth, which alters the lateral density of the respective STF<sup>6,34</sup>.

Sculptured thin films by GLAD can be fabricated from a wide variety of materials, including insulators, metals, semiconductors, and organic materials, vaporized by sputtering<sup>35,36,37</sup>, pulsed laser deposition<sup>38</sup>, thermal or (most commonly) electron beam evaporation<sup>27,28,39,40</sup>. Electron-beam evaporation is particularly favorable since the impinging atoms have very low energy ( $< 1$  eV) and larger amounts of material can be vaporized at constant conditions compared to thermal evaporation. STFs are fabricated under low-atom-mobility conditions, where the sticking coefficient (ratio of adsorbed adatoms and total number of adatoms arriving within the same period of time) is essentially unity, and hence substrate temperatures of less than 10% of the melting point of the evaporant are desired for columnar growth<sup>27</sup>. Therefore STFs can be deposited on virtually any substrate material (e.g., glass and polymers) because the substrate can be kept at room-temperature.

### 2.1.1 Organized In-plane Growth

GLAD on flat substrates results in random in-plane distribution of nanostructures with a “quasi-periodic” topology because of an average intercolumnar spacing due to the shadowing characteristics<sup>41,42</sup>. The random in-plane distribution originates from the self-organized growth due to the stochastic condensation process on the substrate surface and the subsequent competing growth mechanism. Lateral coherence can be achieved when depositing on patterned substrates. Patch- or dot pattern, for example, may determine initial shadowing conditions and serve as nucleation and condensation seeds for the incoming particle flux<sup>43</sup>. Electron-beam lithography is a widespread method for pre patterning substrates, however, only small areas can be patterned (in the order of  $100 \times 100 \mu\text{m}^2$ ), it is costly, and the resulting seeds are  $> 20$  nm in diameter<sup>44,45,46,47</sup>. Self-assembly large-scale patterning techniques such as nanosphere or diblock-copolymer nanolithography are advantageous over electron beam lithography because smaller seed sizes can be achieved and yet they are more economical<sup>48,49,50,51,52,53</sup>.

**Table 2.1:** Proposed nomenclature for STFs derived from basic building block configurations, where the  $x$  in  $Fx$  stands for the number of equally spaced rotation steps within one full substrate turn and with same rotation sense during fabrication.  $l$  is an integer number ( $> 1$ ) and denotes the number of layers. Chiral STFs, starting with  $2F3^\pm$ -STF (three-fold symmetry, not shown here) and above, have to be additionally characterized by their handedness - indicated by a '+' for right-handed (clockwise) and a '-' for left-handed (counterclockwise). For helical (continuously rotated) STFs ( $H^\pm$ -STF),  $t$  indicates the number of turns.

Proposed Nomenclature	Chiral	Footprint	Example Geometry	Description
F1-STF	No			(slanted) columnar thin film
$l$ F2-STF	No			chevron or zig-zag; example shown: 3F2
$l$ F4 $^\pm$ -STF	Yes			four-fold staircase; example shown: 9F4 $^+$
$t$ H $^\pm$ -STF	Yes			helical thin film; example shown: 2H $^-$
V-STF	No			(vertical) columnar thin film

**Diblock-copolymer nanolithography.** Diblock-copolymer or micelle nanolithography is a self-assembly process to place metal nanodots in a regular pattern onto a flat substrate. Diblock copolymers comprise a polar and non-polar polymer block dissolved in a non-polar solvent. Once a certain concentration is reached these diblock copolymers aggregate into inverse micelles thereby forming a core-shell structure. The micelle nanoreactor permits selective dissolution of metal salt into the polar micelle core. A dip-coating process step with a flat substrate allows for surface coating of a regular monolayer of metal-loaded micelles. After solvent evaporation, the organic part of the film is selectively etched away by an oxygen plasma treatment leaving the inorganic nanodot pattern behind. The micelle diameter and hence interparticle spacing can be controlled by the size of the block copolymers whereas the nanodot size is predominantly controlled by the amount of metal salt added to the micelle solution<sup>49,50,53,54</sup>.

### 2.1.2 Proposed Sculptured Thin Film Nomenclature

In recent years reports on a wide variety of differently shaped STF's have been published and each research group has used their own terminology to describe the specific shape of the STF under investigation. Therefore, a universal nomenclature scheme for STF's based on their building blocks is proposed to unambiguously identify the STF geometry (Table 2.1). Further simplification for large  $Fx$ -STF's with many substrate rotations can be achieved by using the first unit as the building block and the number of repetitions as a subscript in analogy to structure formulas in organic chemistry: for example, a four-fold staircase with five full turns,  $20F4^+$ -STF, may be written as  $(4F4^+)_5$ . A combination of different geometries can be described by concatenation of individual building blocks. This nomenclature is used throughout this thesis.

## 2.2 Ultrahigh Vacuum Glancing Angle Deposition System

### 2.2.1 Design Considerations

There are basic requirements and aspects, for glancing angle deposition of high quality thin films with controlled nanostructure, which need to be considered when designing an ultrahigh vacuum (UHV) deposition chamber<sup>40</sup>:

1. Control of substrate rotation and tilt angle relative to the vapor source to allow synthesis of thin films with a specific nanostructure.
2. A highly collimated or point-like vapor source that can provide a narrow angular

distribution of flux arriving on the substrate. As geometrical shadowing is critical to the GLAD technique, directionality in the arriving vapor is necessary. A small source such as an evaporator is best and the geometry of the chamber is important (sufficient source-sample distance).

3. The deposition has to be performed in vacuum conditions with pressures below  $10^{-8}$  mbar ( $10^{-6}$  Pa) in order to minimize the effects of contamination and reduce scattering events to ensure a collimated particle flux.
4. Variable substrate temperature (heating and cooling) in order to enable variation of film nanostructure by controlling surface diffusion due to heat transfer during nucleation and growth.
5. The existence of a fast and easy transfer mechanism of specimens from atmospheric pressure to an UHV environment. An efficient UHV chamber design with load-lock chamber allows the introduction and removal of samples without venting and pumping the main chamber, saving considerable time and enhancing equipment lifetime (e.g., pumps and vacuum gauges) of the main chamber.
6. The deposition parameters should be controllable by computer and all process parameters should be monitored throughout the deposition process.
7. The system should be equipped with in-situ diagnostic tools and several additional ports for future improvements.

The chamber design, selection of pumping system, and provisions for incorporating various features and accessories were decided based on the above requirements. Care has been taken for the selection of UHV compatible materials in the construction of the system.

### 2.2.2 Deposition System

The custom-made UHV GLAD system is constructed from type 304 stainless steel. All demountable flange ports are of conflat type and used with oxygen-free high conductivity copper gaskets, except the load-lock chamber door, which is sealed by a rubber o-ring to allow fast sample in- and output. Attached vacuum components are specified as UHV compatible. The system consists of two main components: the load-lock chamber and the deposition chamber, which both are shown in Fig. 2.2. The entire



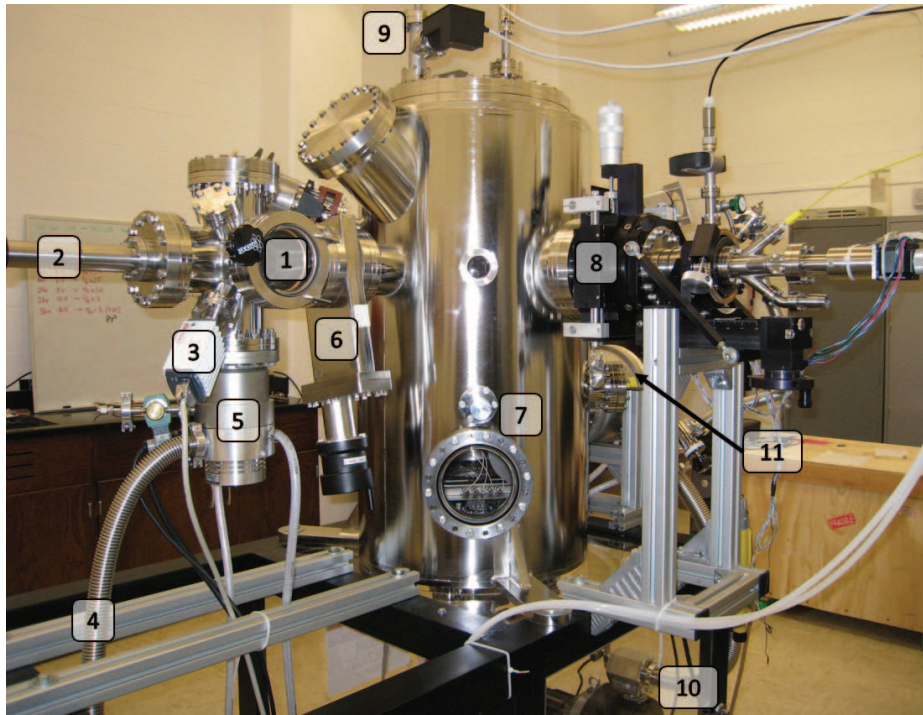


**Figure 2.2:** Photograph of the UHV GLAD system with: (1) door for sample in- and output, (2) magnetically-coupled linear-rotary feedthrough with sample transfer system, (3) vacuum gauge, (4) connection to roughening pump, (5) turbo pump, (6) gate valve to deposition chamber, (7) viewport with shutter and maintenance flange for e-beam evaporator system, (8) sample manipulator unit with stepper motor, (9) vacuum gauges, (10) roughening pump, and (11) turbo pump. Items (1)-(5) belong to the load-lock chamber whereas (7)-(11) are parts of the deposition chamber.

assembly is mounted on a steel frame with adjustable rubber feet. The sample transfer arm, which protrudes far from the deposition chamber, is actively supported by aluminum extrusions attached to the steel frame.

The employed electron-beam evaporation technique, utilizing constant electron bombardment for material heating, allows for vaporization of a solid material. Glancing angle deposition has been successfully demonstrated, in the UHV chamber described herein, by deposition of STFs from Al, Co, Si, Ti, and supermalloy ( $\text{Ni}_{80}\text{Fe}_{15}\text{Mo}_5$ ). During operation, a customized LabVIEW program is used to control the stepper motor driving the azimuthal sample rotation. The control software further logs various deposition parameters such as: electron-beam acceleration voltage, emission current and filament current; deposition chamber pressure (Penning transmitter readout); deposition rate and (reference) total film thickness.

### 2.2.2.1 Load-lock Chamber and Sample Transfer System

The load-lock chamber serves as an intermediate stage between atmospheric pressure and UHV conditions. It is used to introduce samples into the deposition chamber. Attached to the load-lock is a magnetically-coupled linear-rotary feedthrough with 750 mm linear travel distance and 360° continuous rotation, which holds the turn-to-lock sample platen transfer fork. This substrate carrier system allows for samples, mounted onto molybdenum platens, to be transferred to the sample manipulator with dock assembly inside the deposition chamber, once sufficiently low pressure is reached and the gate valve can be opened. With a 250 l/min dry scroll vacuum pump (Triscroll 300, Varian) and a water-cooled 145 l/s turbomolecular pump (Turbovac 151, Leybold) vacuum conditions of  $10^{-6}$  mbar can be achieved in less than 5 min, whereas the minimum pressure reachable without baking is  $10^{-8}$  mbar. A hot ion combi gauge (ITR 90, Leybold) is used to monitor the load-lock pressure. The gauge comprises a Bayard-Alpert hot cathode ionization measurement system (for  $P_a < 2 \times 10^{-2}$  mbar) and a Pirani gauge (for  $P_a > 5.5 \times 10^{-3}$  mbar). The load-lock is connected to a dry nitrogen gas cylinder through an inlet for venting to atmospheric pressure.

### 2.2.2.2 Deposition Chamber

The GLAD deposition chamber is of cylindrical shape with a height of 860 mm and diameter of 500 mm. It is equipped with a 4-pocket electron-beam evaporator (Telemark), a sample manipulator unit (Thermionics), a quartz crystal microbalance deposition rate controller (Inficon), electrical and motion feedthroughs, viewports with shutters, and optical ports for ellipsometer attachment. In order to achieve UHV conditions, a 500 l/min dry mechanical scroll pump (Triscroll 600, Varian) and a water-cooled 1100 l/s turbomolecular pump (Turbovac 1000 C, Leybold) are attached to the chamber. Within a short time (approx. 10 min) a pressure of  $P_a < 4 \times 10^{-2}$  mbar is reached with the scroll pump, which serves as a backing pump for the turbomolecular pump. The typical base pressure of the UHV system reached without bake-out and degas is  $10^{-8}$  mbar. After a first Ti evaporation\* the base pressure is  $< 10^{-9}$  mbar, and the pressure during further depositions, also of other materials, is always less than  $10^{-7}$  mbar. The pressure is monitored with two separate vacuum gauges: a transmitter based on the Pirani thermal conductivity principle (Thermovac TTR91, Leybold) for pressures in the range of  $5 \times 10^{-4} < P_a < 1000$  mbar and a Penning gauge (Penningvac

---

\*Ti serves as a getter material, i.e. it has the ability to collect free gases by adsorption, which improves the vacuum.

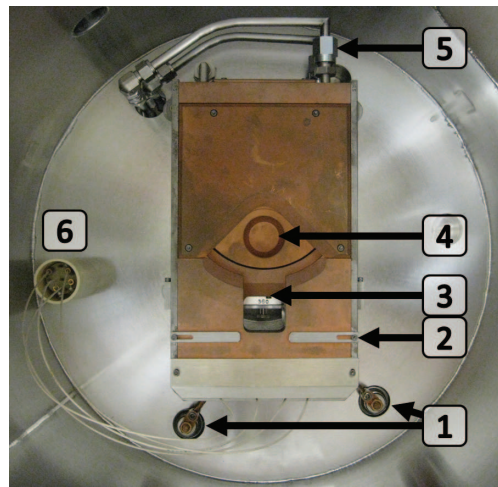


**Figure 2.3:** Top-view photograph of the electron-beam evaporator installed inside the deposition chamber. (1) high voltage leads and feedthroughs, (2) magnetic pole pieces (lens), (3) location of the filament (only indicated), (4) material pocket, (5) water-cooling pipes, (6) electrical feedthrough for electromagnet coils (beam sweep).

PTR225, Leybold) with a rugged cold cathode sensor for the lower and UHV range ( $1 \times 10^{-9} \dots 1 \times 10^{-2}$  mbar). The Penning transmitter can be coupled to the read-out of the Pirani gauge such that it will be automatically switched on (off) if the pressure is less (greater) than  $1 \times 10^{-3}$  mbar.

### 2.2.2.3 Electron-beam Evaporation System

The multipocket electron-beam evaporator (STIH-270-2CK, Temescal) is mounted on four 50 mm aluminum rods on the bottom of the deposition chamber. The distance between the source and the substrate is 460 mm. For this source-substrate distance the particle flux is sufficiently collimated for optimum shadowing characteristics at the sample. The evaporator, in general, provides a stable vapor flux with an over-cosine distribution and maximum divergence angle of  $3.1^\circ$  considering a point source and a 25 mm diameter substrate at normal incidence. The energy of a vaporized particle before it hits the target is less than 1 eV, which is one of the reasons for low adatom mobility of the condensed particles<sup>27</sup>.

The electron-gun has a water-cooled copper turret with four  $15 \text{ cm}^3$  material pockets, which can accommodate a crucible liner (graphite,  $\text{Al}_2\text{O}_3$ , or BN, for example) filled with the source material, in form of pellets or pieces. Only one crucible is in evaporation position, which reduces the risk of cross contamination, while the others are

covered by the crucible cover. An externally mounted turret source indexer (Model 379, Telemark), coupled to the bottom drive of the carousel through a rotary feedthrough allows for selection of the desired material pocket. Electrons are extracted from a hot tungsten filament (thermionic emission), accelerated in an electric field with a potential difference of up to 10 kV and then bent in a constant magnetic field by  $270^\circ$  to hit the material. The target is heated through this constant electron bombardment and eventually starts to evaporate. The electron beam with a maximum current of 800 mA can be focussed by moving two pole pieces constituting a magnetic lens (Fig. 2.3). Additionally, a pair of electromagnets can be controlled with a beam sweep module (Cheetah Digital, Telemark) to “write” an arbitrary pattern thereby achieving more homogenous material evaporation. The emission current can be controlled either manually or automatically to adjust constant desired deposition rates. The substrate is shielded from the evaporation source by a manual shutter, which can be opened once a stable particle flux is established.

An issue associated with the current electron-beam evaporation source is a correlation between trough filling fraction and nanostructure geometry. During deposition and over several runs the filling level decreases, which results in changing source conditions affecting the evaporation cone and therefore the growth conditions on the substrate. Investigations within the course of this work have shown that the slanting angle, for example, can be influenced by changing the size of the evaporation source.

#### 2.2.2.4 Sample Manipulator

The sample manipulator unit (Thermionics) as one of the most important parts of a GLAD system, has to be capable of providing customized azimuthal substrate rotation and control over an adjustable tilt angle  $\theta_i$  (Fig. 2.4). The sample manipulator is mounted on a horizontal  $(x, y, z)$  stage:  $(x, y)$  can be adjusted with two micrometer screws with a maximum travel of  $\pm 25$  mm, whereas the 100 mm ( $z$ ) movement is achieved with a gearbox drive (pre-loaded screw and worm shaft). The  $(x, y, z)$  degrees of freedom are required to place the sample above the center of the source material and to adjust the sample transfer position such that the transfer fork meets the dock on the manipulator side to pass the sample platen via turn-to-lock. The sample dock is a copper ring (part of the water cooled all-copper ball bearing actuation) with three molybdenum clips on the perimeter for holding the molybdenum sample platen, and is capable of customized azimuthal rotation around the substrate normal with simultaneous cooling or heating. This sample in-plane rotation is automated by a geared,

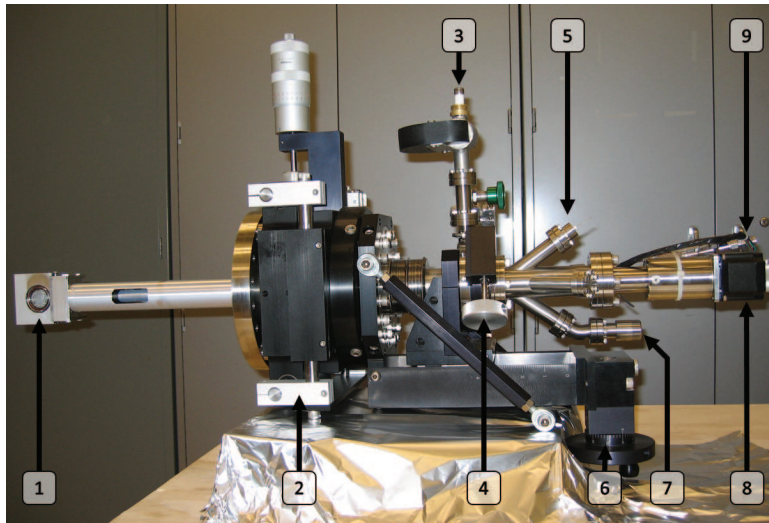


**Figure 2.4:** Photograph of the sample manipulator unit. (1) water-cooled gear-box with sample dock assembly and nude filament radiant resistive heater, (2)  $(x, y)$  stage with  $\pm 25$  mm travel, (3) ion pump on second stage of differentially pumped rotary platform, (4) adjustment wheel for polar sample rotation (determines  $\theta_i$ ), (5) connection to two type K thermocouples for substrate temperature monitoring/control, (6) drive for 100 mm  $z$ -movement, (7) connection for resistive heater power supply, (8) computer controlled stepper motor for sample azimuthal rotation, (9) water pipe in/outlets.

computer controlled stepper motor and enables controlled growth of arbitrary STFs geometries. Inside the copper ring and hence right behind the platen is a nude tungsten filament radiant resistive heater laid out in a “back-and-forth” pattern and specified for operation up to  $1200\text{ }^\circ\text{C}$  at maximum current of 15 A. Installed behind the molybdenum heater base is an alumel-chromel (K-type) thermocouple, which gives a reference temperature (a calibration curve of the actual sample temperature has to be recorded prior to usage).

The entire manipulator body can be rotated with a differentially pumped rotary platform by  $\pm 180^\circ$ . This movement determines the sample tilt with respect to the incoming particle flux ( $\theta_i$ ). The atmospheric side (first stage) of the rotary seal is connected to the deposition chamber roughening pump. The vacuum side (second stage) is connected to a 2 l/s appendage ion pump. The ion pump can be turned on when the pressure reaches  $< 10^{-6}$  mbar; the two stages then have to be isolated from each other through a valve.

### 2.2.2.5 Deposition Controller

The quartz crystal microbalance deposition controller (XTC/3S, Inficon) is based on the measurement principle that mass adsorption changes the resonance frequency of a quartz crystal resonator. The sensor employs a temperature-compensated AT-cut quartz crystal, operating at a base frequency of 6 MHz and sitting on a water-cooled body to avoid frequency shifts due to temperature changes and therefore false readings. The sensor head is mounted in close proximity to the substrate holder such that the crystal normal is parallel to the direction of the incoming particle flux. The crystal can be shielded from the vapor with a pneumatic shutter. This shutter guards against sputtering during the initial material heating phase prior to deposition and may prolong the lifetime of the crystal during deposition if closed periodically.

The deposition rate can be calculated with the Sauerbrey equation<sup>55</sup>, which relates a frequency change  $\Delta f$  to a change in mass  $\Delta m$  of the evaporated material:

$$\Delta f = -\frac{2f_0^2}{A_q\sqrt{\rho_q\mu_q}}\Delta m. \quad (2.1)$$

$f_0$  and  $A_q$  are the fundamental frequency and the area of the quartz crystal, respectively, and  $\rho_q = 2.648 \text{ g/cm}^3$  and  $\mu_q = 2.947 \cdot 10^{11} \frac{\text{g}}{\text{cm s}^2}$  are the density and shear modulus for an AT-cut quartz crystal. However, for frequency changes  $\Delta f/f > 0.02$  the so-called  $Z$ -match method<sup>56</sup> must be used to accurately determine the mass change

$$\frac{\Delta m}{A_q} = \frac{N_q\rho_q}{\pi Z f_L} \tan^{-1} \left[ Z \tan \left( \pi \frac{f_U - f_L}{f_U} \right) \right], \quad (2.2)$$

where the  $Z$  factor denotes the ratio between the shear mode acoustic impedance of the deposited material (subscript  $f$ ) and that of quartz (subscript  $q$ ):

$$Z = \sqrt{\frac{\rho_q\mu_q}{\rho_f\mu_f}}. \quad (2.3)$$

Here  $f_L$  and  $f_U$  are the frequencies of the loaded and unloaded crystal, respectively, and  $N_q$  the frequency constant of an AT-cut quartz crystal. Note that since the quartz crystal is installed within the line of sight of the evaporation source, bulk values for rigid films can be used. However, in order to have reliable thickness calculations a calibration curve has to be recorded. A so-called tooling factor (depending on  $\theta_i$ ) then relates the thickness measured by the oscillating crystal and the actual film thickness.

# Chapter 3

## Characterization Methods

### 3.1 Structural Properties

#### 3.1.1 Scanning Electron Microscopy

In a scanning electron microscope (SEM) a primary (high energy) electron beam is scanned in a raster scan pattern over a sample surface. The interaction of the electron beam with the atoms composing the sample produces various kinds of information such as X-rays, secondary electrons, backscattered electrons, and Auger electrons. Typical SEM micrographs, which are topographical surface images, are reconstructed from the detected secondary (low energy) electrons. Other signals can be used for compositional observation and elemental analysis, for instance. For a comprehensive treatise of scanning electron microscopy the reader is referred to the book by Goldstein *et al.*<sup>57</sup> and references therein.

The type of electron gun used in a SEM is crucial for the resolution. Three different types are generally used: a tungsten hairpin filament, a LaB<sub>6</sub> filament (both thermionic emission guns), and a cold cathode field-emission (FE) gun. The brightness and size of the electron source of a FE gun is approximately three orders of magnitude smaller than the thermionic guns and therefore yields the highest resolution<sup>57</sup>. The generated primary electron beam, with energies ranging from 0.5 keV up to 40 keV, is focused by electromagnetic lenses (typically two condenser lenses and one objective lens) onto the surface under investigation. After the condenser lenses, pairs of coils (or plates) are deflecting the beam in the  $x$  and  $y$  direction such that the sample surface is scanned in a raster fashion.

The low energy ( $< 50$  eV) secondary electrons generated due to inelastic scattering interactions of atoms with beam electrons are detected by an Everhart-Thornley detector, which is a special type of scintillator-photomultiplier system<sup>58</sup>. A positively biased grid ( $\sim 300$  V) attracts only low energy particles, which are further accelerated toward

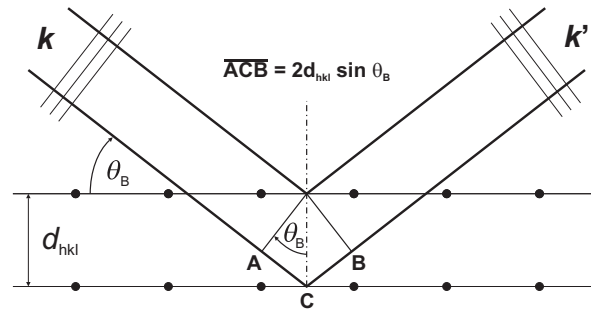


**Figure 3.1:** The incoming beam causes each scatterer to re-radiate a small portion of its intensity as a spherical wave. If scatterers are arranged symmetrically with a separation  $d_{hkl}$ , these spherical waves will add constructively only in directions where their path-length difference  $ACB$  equals an integer multiple of the wavelength. In that case, part of the incoming beam is deflected by an angle  $2\theta_B$ , producing a reflection spot in the diffraction pattern.

a scintillator. Together with the beam position  $(x, y)$  information, the two-dimensional signal intensity distribution represents a topographical image of the sample surface since the number of electrons reaching the detector depends on the surface texture.

SEM micrographs presented in this thesis have been recorded with a FE-SEM (S4700 Field-Emission SEM, Hitachi) specified for magnifications up to  $500\,000\times$  and an ultimate resolution of  $< 2$  nm. Typically, acceleration voltages of 6 to 8 keV were used at working distances of around 8 mm. For top-down images samples were glued with carbon tape to the specimen holder whereas for cross-section images the samples were mechanically clamped in a vertical position. This method, not involving any glue or tape, warrants a steady sample position even at the nanometer scale and allows for high resolution cross-sectional micrographs.

### 3.1.2 X-ray Diffraction

X-ray diffraction (XRD) is a widely used non-destructive method to determine properties of the crystal lattice. In an XRD experiment a beam of monochromatic electromagnetic waves with wavelength corresponding to the X-ray region is incident on a crystal and consequently diffracted, due to elastic scattering at parallel crystal planes separated by distance  $d$  (Fig. 3.1). The condition of constructive interference of scattered wave fronts and can be mathematically determined by Bragg's law:

$$2d_{hkl} \sin \theta_B = m\lambda, \quad (3.1)$$



with  $d_{hkl}$  being the spacing between the set of diffracting planes  $\{hkl\}^*$ ,  $\theta_B$  is the Bragg angle,  $m$  is any integer, and  $\lambda$  is the wavelength of the X-ray beam. Diffraction peaks due to constructive interference can be detected by performing a  $\theta_B - 2\theta_B$  scan and yield information about crystal structure and orientation<sup>59</sup>.

XRD measurements presented in this theses were carried out with a X-ray diffractometer (Multiflex+, Rigaku), which operates with Cu K $\alpha$  ( $\lambda = 1.54056 \text{ \AA}$ ) radiation. The sample is mounted horizontally on a  $\theta_B - 2\theta_B$  goniometer and illuminated with an approximately 10 mm wide beam such that a relatively broad sample area is illuminated the resulting reflections represent a mean value.

## 3.2 Spectroscopic Ellipsometry

Spectroscopic ellipsometry (SE) determines the complex-valued ratio  $\rho$  of linearly independent electric field components of polarized electromagnetic plane waves; i.e., the change of the polarization state of an electromagnetic plane wave upon interaction with a sample. Traditionally, this ratio is measured in reflection or transmission for light polarized parallel ( $p$ ), and perpendicular ( $s$ )<sup>†</sup> to the plane of incidence and expressed by the two real-valued ellipsometric values  $\Psi$  and  $\Delta$ <sup>60,‡</sup>

$$\rho = \left( \frac{B_p}{B_s} \right) / \left( \frac{A_p}{A_s} \right) = \tan \Psi e^{i\Delta}, \quad (3.2)$$

where amplitudes  $A$  stand for incident and  $B$  for exiting plane waves with  $p$ - and  $s$ -polarization components with respect to the plane of incidence as defined in the reflection arrangement in Fig. 3.2<sup>§</sup>. The absolute value of the complex ratio is defined by  $\tan \Psi$ , and  $\Delta$  denotes the relative phase change of the  $p$  and  $s$  components of the electric field vector<sup>61,62,63,64</sup>.

The complex ratio  $\rho$  can be addressed within different presentations of the electromagnetic plane wave response. Also, depending on the sample properties, i.e., for anisotropic samples, which cause mode conversion between  $p$ - and  $s$ -polarized light upon reflection (or transmission), the ellipsometric parameter set must be further expanded into the so-called generalized ellipsometry parameter set. In such cases the

\*The three integers  $hkl$  denote the Miller indices.

†The abbreviation “s” comes from the German word senkrecht for perpendicular.

‡Unless used unambiguously as running index, the symbol “ $i$ ” addresses the imaginary unit  $\sqrt{-1}$ .

§Considerations are given for a reflection set up, but hold for the complex-valued ratio of polarized plane wave components in the transmission arrangement as well.

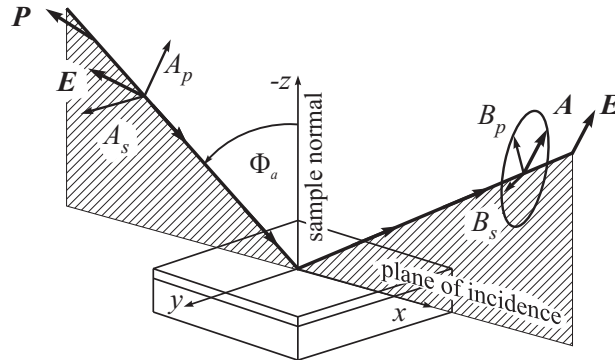


**Figure 3.2:** The wavevectors of the incident and emerging plane waves (incident and reflected at an angle  $\Phi_a$ ) and the sample normal define the plane of incidence ( $x$ - $z$  plane).  $A_p$ ,  $A_s$ ,  $B_p$ , and  $B_s$ , denote the complex amplitudes of the  $p$  and  $s$  modes before and after reflection, respectively.  $P$  and  $A$  are the azimuth angles of the linear polarizers used, for example, in the standard arrangement of rotating-analyzer (polarizer) ellipsometers.

Jones matrix presentation provides a convenient and sufficient frame. However, depolarization of light upon interaction with an optical system cannot be treated with the Jones formalism. In this case the Mueller matrix presentation is the appropriate choice.

### 3.2.1 Definition of the Optical Constants

The ellipsometric quantities  $\Psi$  and  $\Delta$  are related to wave optics through a solution of the wave equation:  $\mathbf{E} = E_0 \exp\{i\mathbf{k}\mathbf{r}\}$ , with  $E_0$  being the amplitude of the electric-field intensity  $\mathbf{E}$  at spatial variable  $\mathbf{r}$ . The propagation vector  $\mathbf{k}$  is a function of the complex-valued refractive index (optical constants) of the medium  $N = n + ik$ . The refractive index  $n$  follows experimentally from Snell's law:

$$n_1 \sin \theta_1 = n_2 \sin \theta_2, \quad (3.3)$$

where  $\theta_j$  is the angle of incidence counted toward the interface between two materials with  $n_1$  and  $n_2$ . The extinction coefficient  $k$  is connected to the absorption, measured by intensity ( $I = \mathbf{E}\mathbf{E}^*$ ) loss upon wave propagation over a distance  $d$ ,

$$I = I_0 \exp\{-\alpha' d\}, \quad (3.4)$$

with the absorption coefficient  $\alpha'$  being

$$\alpha' = \frac{4\pi}{\lambda} k. \quad (3.5)$$

Refractive index  $n$  and extinction coefficient  $k$  are defined for propagating waves along direction  $\mathbf{k}$  in a material, and for a given direction  $\mathbf{E}$ , such that both  $n$  and  $k$  would occur as in (3.3) and (3.5). As will be discussed later, for materials with monoclinic and triclinic optical properties such experiments cannot be designed, instead coupling with different propagation constants will occur in general. Generalized ellipsometry (GE) is the only appropriate tool to differentiate between the intrinsic propagation constants, the refractive index and extinction coefficient for major polarizability axes  $\mathbf{a}$ ,  $\mathbf{b}$ , and  $\mathbf{c}$ .

### 3.2.2 Jones and Mueller Matrix Presentation

**The Jones Matrix Presentation.** For non-depolarizing samples, the so-called Jones matrix provides a complete mathematical description for the electromagnetic plane wave response and allows for ellipsometric data analysis<sup>60,65,66,67,68</sup>.

The Jones reflection matrix  $\mathbf{J}$ , for a sample with plane parallel boundaries, connects the incident  $A$  modes ( $p, s$ ) with emergent  $B$  plane wave modes ( $p, s$ ):

$$\begin{pmatrix} B_p \\ B_s \end{pmatrix} = \mathbf{J} \begin{pmatrix} A_p \\ A_s \end{pmatrix} = \begin{pmatrix} r_{pp} & r_{ps} \\ r_{sp} & r_{ss} \end{pmatrix} \begin{pmatrix} A_p \\ A_s \end{pmatrix}. \quad (3.6)$$

The Jones matrix  $\mathbf{J}$  contains four complex-valued elements, which are also known as the anisotropic Fresnel reflection coefficients\*. The off-diagonal elements of  $\mathbf{J}$  are nonzero for optical systems that convert  $p$  into  $s$  waves and vice versa.

**The Mueller Matrix Presentation.** An alternative description of the polarized sample response is the Mueller matrix and the Stokes vector formalism. This approach can furthermore completely account for depolarization. The four real-valued Stokes parameters<sup>†</sup> ( $S_j, j = 0 \dots 3$ ) of an electromagnetic plane wave are defined in terms of the  $p$ - and  $s$ -polarized coordinate system:

$$S_0 = I_p + I_s, \quad (3.7a)$$

$$S_1 = I_p - I_s, \quad (3.7b)$$

$$S_2 = I_{45} - I_{-45}, \quad (3.7c)$$

$$S_3 = I_{\sigma+} - I_{\sigma-}, \quad (3.7d)$$

---

\*In this notation the first index denotes the incident polarization mode, and the second index refers to the outgoing polarization mode.

†The Stokes parameters have dimensions of intensities.

where  $I_p$ ,  $I_s$ ,  $I_{45}$ ,  $I_{-45}$ ,  $I_{\sigma+}$ , and  $I_{\sigma-}$  denote the intensities for the  $p$ -,  $s$ -,  $+45^\circ$ ,  $-45^\circ$ , right-, and left-handed circularly polarized light components, respectively<sup>60,69</sup>. The degree of polarization  $D_P$  for any state of polarization can be expressed by the Stokes parameters as<sup>70</sup>

$$D_P = \frac{I_{\text{pol}}}{I_{\text{tot}}} = \frac{(S_1^2 + S_2^2 + S_3^2)^{1/2}}{S_0}, \quad 0 \leq D_P \leq 1, \quad (3.8)$$

where  $I_{\text{pol}}$  is the intensity of the sum of polarization components and  $I_{\text{tot}}$  is the total intensity of the beam. A value of  $D_P = 1$  corresponds to completely polarized light,  $D_P = 0$  corresponds to unpolarized light, and  $0 < D_P < 1$  corresponds to partially polarized light. Arranging the Stokes parameters into a column vector, the Mueller matrix then describes the changes of each quantity upon interaction of the electromagnetic plane wave with an optical system\* as

$$\begin{pmatrix} S_0 \\ S_1 \\ S_2 \\ S_3 \end{pmatrix}_{\text{out}} = \begin{pmatrix} M_{11} & M_{12} & M_{13} & M_{14} \\ M_{12} & M_{22} & M_{23} & M_{24} \\ M_{13} & M_{32} & M_{33} & M_{34} \\ M_{14} & M_{42} & M_{43} & M_{44} \end{pmatrix} \begin{pmatrix} S_0 \\ S_1 \\ S_2 \\ S_3 \end{pmatrix}_{\text{in}}. \quad (3.9)$$

The advantage of the Mueller matrix concept is the ability to handle situations with partial polarization of the electromagnetic plane wave. Further details, the application to ellipsometry, and the relation to the Jones concept have been outlined previously by Azzam and Bashara<sup>60</sup>, Röseler<sup>69</sup>, and Jellison<sup>71,72,73</sup>.

In a rotating-analyzer-system, for example, the Mueller matrix elements of the 4<sup>th</sup> row and the 4<sup>th</sup> column cannot be measured. However, this does not impair the accessibility of the normalized Jones matrix elements, (3.6), except for its relative phase, which can only be obtained by including compensator(s)<sup>64,69</sup>.

For a non-depolarizing system, a one-to-one relation exists between matrices  $\mathbf{J}$  and  $\mathbf{M}$ <sup>60</sup>:

$$M_{11} = \frac{1}{2} (r_{pp}r_{pp}^* + r_{ss}r_{ss}^* + r_{sp}r_{sp}^* + r_{ps}r_{ps}^*), \quad (3.10a)$$

$$M_{12} = \frac{1}{2} (r_{pp}r_{pp}^* - r_{ss}r_{ss}^* - r_{sp}r_{sp}^* + r_{ps}r_{ps}^*), \quad (3.10b)$$

$$M_{13} = \text{Re} (r_{pp}r_{sp}^* + r_{ss}^*r_{ps}), \quad (3.10c)$$

$$M_{14} = \text{Im} (r_{pp}r_{sp}^* + r_{ss}^*r_{ps}), \quad (3.10d)$$

---

\*Sample, mirrors, rotators, optical devices within the light path, and any combinations thereof.

$$M_{21} = \frac{1}{2} (r_{pp}r_{pp}^* - r_{ss}r_{ss}^* + r_{sp}r_{sp}^* - r_{ps}r_{ps}^*), \quad (3.10e)$$

$$M_{22} = \frac{1}{2} (r_{pp}r_{pp}^* + r_{ss}r_{ss}^* - r_{sp}r_{sp}^* - r_{ps}r_{ps}^*), \quad (3.10f)$$

$$M_{23} = \operatorname{Re} (r_{pp}r_{sp}^* - r_{ss}^*r_{ps}), \quad (3.10g)$$

$$M_{24} = \operatorname{Im} (r_{pp}r_{sp}^* - r_{ss}^*r_{ps}), \quad (3.10h)$$

$$M_{31} = \operatorname{Re} (r_{pp}r_{ps}^* + r_{ss}^*r_{sp}), \quad (3.10i)$$

$$M_{32} = \operatorname{Re} (r_{pp}r_{ps}^* - r_{ss}^*r_{sp}), \quad (3.10j)$$

$$M_{33} = \operatorname{Re} (r_{pp}r_{ss}^* + r_{ps}^*r_{sp}), \quad (3.10k)$$

$$M_{34} = \operatorname{Im} (r_{pp}r_{ss}^* - r_{ps}^*r_{sp}), \quad (3.10l)$$

$$M_{41} = -\operatorname{Im} (r_{pp}r_{ps}^* + r_{ss}^*r_{sp}), \quad (3.10m)$$

$$M_{42} = -\operatorname{Im} (r_{pp}r_{ps}^* - r_{ss}^*r_{sp}), \quad (3.10n)$$

$$M_{43} = -\operatorname{Im} (r_{pp}r_{ss}^* + r_{ps}^*r_{sp}), \quad (3.10o)$$

$$M_{44} = \operatorname{Re} (r_{pp}r_{ss}^* - r_{ps}^*r_{sp}), \quad (3.10p)$$

where  $\{\cdot\}^*$  denotes the complex conjugate. The Mueller matrix for an isotropic sample is given by<sup>73</sup>

$$\mathbf{M} = \begin{pmatrix} 1 & -N_M & 0 & 0 \\ -N_M & 1 & 0 & 0 \\ 0 & 0 & C_M & S_M \\ 0 & 0 & -S_M & C_M \end{pmatrix}. \quad (3.11)$$

The quantities  $N_M$ ,  $S_M$ , and  $C_M$  provide access to the ellipsometric parameters

$$N_M = \cos 2\Psi, \quad (3.12a)$$

$$S_M = \sin 2\Psi \sin \Delta, \quad (3.12b)$$

$$C_M = \sin 2\Psi \cos \Delta. \quad (3.12c)$$

$N_M$ ,  $S_M$ , and  $C_M$  are not independent, and are constrained for non-depolarizing samples by the relation:

$$N_M^2 + S_M^2 + C_M^2 = 1. \quad (3.13)$$

The complex ratio  $\rho$  can be obtained from  $N_M$ ,  $S_M$  and  $C_M$

$$\rho = \frac{C_M + iS_M}{1 + N_M}. \quad (3.14)$$

### 3.2.3 Generalized Ellipsometry

In contrast to standard ellipsometry, in the generalized ellipsometry situation  $\Psi$  and  $\Delta$  depend on the polarization state of the incident plane wave. This concept is valid within both, the Mueller matrix as well as within the Jones matrix formalism. Within the Jones matrix presentation six real-valued generalized ellipsometry angles  $\Psi_{ij}$  and  $\Delta_{ij}$  are defined by three ratios of the four available complex-valued elements of the Jones reflection matrix  $\mathbf{J}$ :

$$R_{pp} \equiv \frac{r_{pp}}{r_{ss}} = \tan \Psi_{pp} \exp(i\Delta_{pp}), \quad (3.15a)$$

$$R_{ps} \equiv \frac{r_{ps}}{r_{ss}} = \tan \Psi_{ps} \exp(i\Delta_{ps}), \quad (3.15b)$$

$$R_{sp} \equiv \frac{r_{sp}}{r_{pp}} = \tan \Psi_{sp} \exp(i\Delta_{sp}). \quad (3.15c)$$

Note that the on-diagonal elements from the same column of the Jones matrix are used to normalize the off-diagonal matrix elements. This choice is convenient for rotating-analyzer ellipsometry<sup>65</sup>.

The generalized ellipsometry concept is required if the response of the optical system is anisotropic, i.e.,  $p$  modes are converted in  $s$  modes and vice versa. This results in non-zero off-diagonal elements of the Jones ( $r_{ps}$  and  $r_{sp}$ ) and Mueller matrix ( $M_{kl}$  and  $M_{lk}$  with  $k = 1, 2$ ;  $l = 3, 4$ ).

### 3.2.4 Anisotropic Dielectric Function Tensor

#### 3.2.4.1 General Description

In condensed matter with non-cubic symmetry, the dielectric function is represented by a complex-valued second-rank tensor  $\boldsymbol{\varepsilon}$ , which can be expressed in Cartesian coordinates ( $x, y, z$ ):

$$\mathbf{D} = \varepsilon_0 (\mathbf{E} + \mathbf{P}) = \varepsilon_0 \boldsymbol{\varepsilon} \mathbf{E} = \varepsilon_0 \begin{pmatrix} \varepsilon_{xx} & \varepsilon_{xy} & \varepsilon_{xz} \\ \varepsilon_{yx} & \varepsilon_{yy} & \varepsilon_{yz} \\ \varepsilon_{zx} & \varepsilon_{zy} & \varepsilon_{zz} \end{pmatrix} \mathbf{E}, \quad (3.16)$$

where the field-phasors displacement  $\mathbf{D}$ , polarization field  $\mathbf{P}$ , and electric field  $\mathbf{E}$  are given along the unit directions  $\mathbf{x}$ ,  $\mathbf{y}$ ,  $\mathbf{z}$  ( $\varepsilon_0$  is the vacuum permittivity):

$$\mathbf{D} = \mathbf{x}D_x + \mathbf{y}D_y + \mathbf{z}D_z, \quad (3.17a)$$

$$\mathbf{E} = \mathbf{x}E_x + \mathbf{y}E_y + \mathbf{z}E_z, \quad (3.17b)$$

$$\mathbf{P} = \mathbf{x}P_x + \mathbf{y}P_y + \mathbf{z}P_z. \quad (3.17c)$$

In general, the dielectric function tensor  $\boldsymbol{\varepsilon}$  is a function of the photon energy  $\hbar\omega$  due to non-local response within the time domain (frequency dispersion). Furthermore, the  $\boldsymbol{\varepsilon}$  tensor may be non-symmetric due to non-local response (chiral) in space<sup>74</sup>.

### 3.2.4.2 Orthogonal Rotations

Interior and exterior Cartesian coordinate axes of a sample under consideration are related by orthogonal rotations. In order to address the  $\boldsymbol{\varepsilon}$  tensor appropriately, a right-handed Cartesian system  $(x, y, z)$  with origin at the sample surface as defined in Fig. 3.2 is set by the plane of incidence  $(x, z)$  and the sample surface  $(x, y)$ . The real-valued Euler angles  $\varphi$ ,  $\theta$ , and  $\psi$  can be used to rotate between the Cartesian laboratory  $(x, y, z)$  and the Cartesian auxiliary coordinate system  $(\xi, \eta, \zeta)$  as defined in Fig. 3.3:

$$\boldsymbol{\varepsilon}(x, y, z) = \mathbf{A}\boldsymbol{\varepsilon}(\xi, \eta, \zeta)\mathbf{A}^{-1}, \quad (3.18)$$

where the unitary matrix\*  $\mathbf{A}$  is the orthogonal rotation matrix<sup>70</sup>

$$\mathbf{A} = \begin{pmatrix} \cos \psi \cos \varphi - \cos \theta \sin \varphi \sin \psi & -\sin \psi \cos \varphi - \cos \theta \sin \varphi \cos \psi & \sin \theta \sin \varphi \\ \cos \psi \sin \varphi + \cos \theta \cos \varphi \sin \psi & -\sin \psi \sin \varphi + \cos \theta \cos \varphi \cos \psi & -\sin \theta \cos \varphi \\ \sin \theta \sin \psi & \sin \theta \cos \psi & \cos \theta \end{pmatrix}. \quad (3.19)$$

First, rotation  $\varphi$  is performed around the  $z$ -axis, then the coordinate system is rotated by  $\theta$  around the new  $x$ -axis, and a final rotation of  $\psi$  around  $\zeta$  completes the coordinate system rotation.

### 3.2.4.3 Bond Polarizability Model

Intrinsic bond polarizations (eigenvectors) set up a spatial non-Cartesian (monoclinic, triclinic), or Cartesian (orthorhombic, tetragonal, hexagonal, trigonal, and cubic) center-of-gravity system, with axes described by vectors  $\mathbf{a} = \mathbf{x}a_x + \mathbf{y}a_y + \mathbf{z}a_z$ ,  $\mathbf{b} = \mathbf{x}b_x + \mathbf{y}b_y + \mathbf{z}b_z$ , and  $\mathbf{c} = \mathbf{x}c_x + \mathbf{y}c_y + \mathbf{z}c_z$ . The linear polarization response is additive, and may be split into

$$\mathbf{P} = \mathbf{P}_a + \mathbf{P}_b + \mathbf{P}_c, \quad (3.20)$$

---

\*Note that  $\mathbf{A}^{-1} = \mathbf{A}^T$ , where  $\{\cdot\}^T$  denotes the transpose of a matrix.

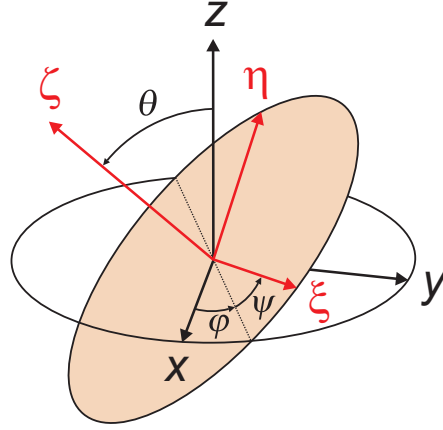


**Figure 3.3:** Definition of the Euler angles  $\varphi$ ,  $\theta$ , and  $\psi$  and the orthogonal rotations as provided by **A**.  $(\xi, \eta, \zeta)$ , and  $(x, y, z)$  refer to the Cartesian auxiliary and laboratory coordinate systems, respectively.

where

$$\mathbf{P}_a = \varrho_a (\mathbf{a}\mathbf{E}) \mathbf{a}, \quad (3.21a)$$

$$\mathbf{P}_b = \varrho_b (\mathbf{b}\mathbf{E}) \mathbf{b}, \quad (3.21b)$$

$$\mathbf{P}_c = \varrho_c (\mathbf{c}\mathbf{E}) \mathbf{c}. \quad (3.21c)$$

The complex-valued scalar major polarizabilities  $\varrho_a, \varrho_b, \varrho_c$  must obey Kramers-Kronig consistency, and correspond to the intrinsic center-of-gravity bond polarization system. Under restrictions to linear polarization, the second-rank susceptibility tensor  $\chi$  is defined by

$$\mathbf{P} = \varepsilon_0 \chi \mathbf{E} = \varepsilon_0 \begin{pmatrix} \chi_{xx} & \chi_{xy} & \chi_{xz} \\ \chi_{yx} & \chi_{yy} & \chi_{yz} \\ \chi_{zx} & \chi_{zy} & \chi_{zz} \end{pmatrix} \mathbf{E}, \quad (3.22)$$

and the electric displacement can be written as

$$\mathbf{D} = \varepsilon_0 (1 + \chi) \mathbf{E} = \varepsilon_0 \begin{pmatrix} 1 + \chi_{xx} & \chi_{xy} & \chi_{xz} \\ \chi_{yx} & 1 + \chi_{yy} & \chi_{yz} \\ \chi_{zx} & \chi_{zy} & 1 + \chi_{zz} \end{pmatrix} \mathbf{E}. \quad (3.23)$$

Accordingly, the corresponding part of the symmetric\* dielectric function tensor  $\varepsilon$  is

\*For purely dielectric material, due to invariance upon time-reversal, there is no directional dependence along one axis (Onsager principle). Only with an external magnetic field this time reciprocity is broken and  $\varepsilon$  becomes antisymmetric. See also Sect. 3.3.



easily deconvoluted by expanding (3.23) and (3.21)<sup>67</sup>:

$$\varepsilon_{xx} = 1 + a_x a_x \varrho_a + b_x b_x \varrho_b + c_x c_x \varrho_c, \quad (3.24a)$$

$$\varepsilon_{xy} = a_x a_y \varrho_a + b_x b_y \varrho_b + c_x c_y \varrho_c, \quad (3.24b)$$

$$\varepsilon_{xz} = a_x a_z \varrho_a + b_x b_z \varrho_b + c_x c_z \varrho_c, \quad (3.24c)$$

$$\varepsilon_{yy} = 1 + a_y a_y \varrho_a + b_y b_y \varrho_b + c_y c_y \varrho_c, \quad (3.24d)$$

$$\varepsilon_{yz} = a_y a_z \varrho_a + b_y b_z \varrho_b + c_y c_z \varrho_c, \quad (3.24e)$$

$$\varepsilon_{zz} = 1 + a_z a_z \varrho_a + b_z b_z \varrho_b + c_z c_z \varrho_c. \quad (3.24f)$$

Note that  $\varepsilon_{ij} = \varepsilon_{ji}$  and that (3.24) describe the most general form of an anisotropic dielectric symmetric tensor. For anisotropic materials, besides the coordinates of the unit axes  $\mathbf{a}$ ,  $\mathbf{b}$ , and  $\mathbf{c}$ , three polarizability functions  $\varrho_j$  ( $j = a, b, c$ ) need to be differentiated, which can be identified by major-axes dielectric function spectra  $\varepsilon_j(\omega)$  for certain symmetries only.

For orthorhombic, tetragonal, hexagonal, trigonal, and cubic symmetry, a real-valued rotation matrix  $\mathbf{A}$  independent of wavelength can be found such that  $\varepsilon$  is diagonal in a given orthogonal axes system  $\mathbf{a}, \mathbf{b}, \mathbf{c}$ :

$$\varepsilon = \mathbf{A} \begin{pmatrix} \varepsilon_a & 0 & 0 \\ 0 & \varepsilon_b & 0 \\ 0 & 0 & \varepsilon_c \end{pmatrix} \mathbf{A}^{-1}, \quad (3.25)$$

where  $\varepsilon_a \equiv 1 + \varrho_a$ ,  $\varepsilon_b \equiv 1 + \varrho_b$ , and  $\varepsilon_c \equiv 1 + \varrho_c$ .

For the monoclinic and triclinic crystal system such a wavelength-independent rotation matrix does not exist.

**Isotropic Materials.** In the most simple case, with no directional dependence,  $\varepsilon$  is a scalar and the electric displacement reads

$$\mathbf{D} = \varepsilon_0 \varepsilon \mathbf{E}. \quad (3.26)$$

**Uniaxial Materials.** For uniaxial materials with trigonal, tetragonal, and hexagonal symmetry,  $\varepsilon$  has two identical in-plane components  $\varepsilon_a = \varepsilon_b = \varepsilon_{\perp}$  and one out-of-plane  $\varepsilon_c = \varepsilon_{\parallel}$ , and the electric displacement takes the form

$$\mathbf{D} = \mathbf{x} \varepsilon_0 \varepsilon_{\perp} E_x + \mathbf{y} \varepsilon_0 \varepsilon_{\perp} E_y + \mathbf{z} \varepsilon_0 \varepsilon_{\parallel} E_z. \quad (3.27)$$

**Orthorhombic Materials.** For biaxial materials with orthorhombic symmetry, with their coordinate system coincident with a given laboratory system ( $a_y = a_z = b_x = b_z = c_x = c_y = 0$ ,  $a_x = b_y = c_z = 1$ ) one has expectedly

$$\mathbf{D} = \mathbf{x}\varepsilon_0(1 + \varrho_a)E_x + \mathbf{y}\varepsilon_0(1 + \varrho_b)E_y + \mathbf{z}\varepsilon_0(1 + \varrho_c)E_z, \quad (3.28a)$$

$$\mathbf{D} = \mathbf{x}\varepsilon_0\varepsilon_a E_x + \mathbf{y}\varepsilon_0\varepsilon_b E_y + \mathbf{z}\varepsilon_0\varepsilon_c E_z, \quad (3.28b)$$

where the polarization vector in a given direction exclusively depends upon the electric field component in that same direction.

**Monoclinic and Triclinic Materials.** For biaxial materials with non-Cartesian monoclinic and triclinic systems, (3.24) can be represented by a virtual orthogonal basis for  $\mathbf{a}$ ,  $\mathbf{b}$ ,  $\mathbf{c}$  and a projection matrix  $\mathbf{U}$ <sup>75</sup>:

$$\mathbf{U} = \begin{pmatrix} \sin \alpha & (\cos \gamma - \cos \alpha \cos \beta)(\sin \alpha)^{-1} & 0 \\ 0 & (1 - \cos^2 \alpha - \cos^2 \beta - \cos^2 \gamma + 2 \cos \alpha \cos \beta \cos \gamma)^{\frac{1}{2}}(\sin \alpha)^{-1} & 0 \\ \cos \alpha & \cos \beta & 1 \end{pmatrix}. \quad (3.29)$$

Parameters  $\alpha, \beta, \gamma$  are the internal angles between major polarizability axes  $\mathbf{a}$ ,  $\mathbf{b}$ ,  $\mathbf{c}$ , and which differentiate monoclinic ( $\beta \neq \alpha = \gamma = 90^\circ$ ) and triclinic ( $\alpha \neq \beta \neq \gamma$ ) biaxial optical properties. In the definition of  $\mathbf{U}$ , use was made of the following choice of free coordinates: within the auxiliary Cartesian system,  $\mathbf{c}$  is chosen to coincide with the  $z$ -axis, thus  $c_x = c_y = 0$  in (3.24).  $\mathbf{a}$  is chosen to be located within the  $\{x, z\}$ -plane, thus  $a_y = 0$  and  $a_x = \sqrt{1 - a_z^2}$ , and  $b_x, b_z$  follow accordingly where  $b_y = \sqrt{1 - b_x^2 - b_z^2}$ . Thus free parameters in (3.29) are  $a_z, b_x, b_z$ , or equivalently  $\alpha, \beta, \gamma$  as depicted in Fig. 3.4. If all angles  $\alpha = \beta = \gamma = 90^\circ$  the so called direct structure matrix  $\mathbf{U}$  takes the form  $\mathbf{U} = \text{diag}\{1, 1, 1\}$ , where  $\text{diag}\{\cdot\}$  indicates the diagonal  $3 \times 3$  matrix, which represents the orthorhombic symmetry. Explicitly, the dielectric tensor  $\varepsilon_m$  for a biaxial material with monoclinic symmetry takes the form

$$\varepsilon_m = \mathbf{U} \begin{pmatrix} \varepsilon_a & 0 & 0 \\ 0 & \varepsilon_b & 0 \\ 0 & 0 & \varepsilon_c \end{pmatrix} \mathbf{U}^T = \begin{pmatrix} 1 + \varrho_a & 0 & 0 \\ 0 & 1 + \sin^2 \beta \varrho_b & \sin \beta \cos \beta \varrho_b \\ 0 & \sin \beta \cos \beta \varrho_b & 1 + \cos^2 \beta \varrho_b + \varrho_c \end{pmatrix}, \quad (3.30)$$

where  $\beta$  is the monoclinic angle between axes  $\mathbf{b}$  and  $\mathbf{c}^*$ . In the most general form, the

<sup>75</sup>Note the uncommon assignment of unit cell angles. This notation is chosen here because it is equivalent to the definition of the ellipsometric analysis software WVASE32<sup>®</sup><sup>76</sup> and illustrated in Fig. 3.4.

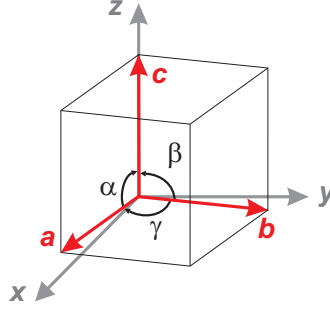


**Figure 3.4:** Definition of the angles  $\alpha$ ,  $\beta$ , and  $\gamma$  as used in WVASE32<sup>®</sup> (J.A. Woollam Co., Inc.). Orthorhombic ( $\alpha = \beta = \gamma = 90^\circ$ ), monoclinic ( $\alpha = \gamma = 90^\circ \neq \beta$ ), and triclinic ( $\alpha \neq \beta \neq \gamma \neq 90^\circ$ ) systems can be distinguished amongst materials with biaxial ( $\varrho_a \neq \varrho_b \neq \varrho_c$ ) properties when evaluating their external Euler angles as a function of wavelength.

dielectric tensor  $\varepsilon_t$  for a triclinic system reads

$$\varepsilon_t = \begin{pmatrix} \varrho_a \sin^2 \alpha + \varrho_b \frac{1}{\sin^2 \alpha} \Gamma^2 & \varrho_b \frac{1}{\sin^2 \alpha} \Gamma \Lambda & (\varrho_a + \varrho_b \frac{1}{\sin^2 \alpha} \Gamma) \sin \alpha \cos \beta \\ \varrho_b \frac{1}{\sin^2 \alpha} \Gamma \Lambda & -\varrho_b \frac{1}{\sin^2 \alpha} \Upsilon & \varrho_b \frac{1}{\sin \alpha} \cos \beta \Lambda \\ (\varrho_a + \varrho_b \frac{1}{\sin^2 \alpha} \Gamma) \sin \alpha \cos \beta & \varrho_b \frac{1}{\sin \alpha} \cos \beta \Lambda & \varrho_a \cos^2 \alpha + \varrho_b \cos^2 \beta + \varrho_c \end{pmatrix}, \quad (3.31)$$

with

$$\Gamma = -\cos \alpha \cos \beta \cos \gamma + \cos \gamma, \quad (3.32a)$$

$$\Lambda = (-\cos^2 \alpha - \cos^2 \beta + 2 \cos \alpha \cos \beta \cos \gamma + \sin^2 \gamma)^{\frac{1}{2}}, \quad (3.32b)$$

$$\Upsilon = \cos^2 \alpha + \cos^2 \beta - 2 \cos \alpha \cos \beta \cos \gamma + \cos^2 \gamma - 1. \quad (3.32c)$$

Experimentally, monoclinic and triclinic properties can only be distinguished by analyzing measured GE data over a wide spectral range. This phenomenon is due to dispersion, i.e., wavelength dependencies of functions  $\varrho_a(\omega)$ ,  $\varrho_b(\omega)$ ,  $\varrho_c(\omega)$ . The rotations to diagonalize (3.24) depend explicitly on  $\varrho_a$ ,  $\varrho_b$ ,  $\varrho_c$  and are thus wavelength dependent. Within a narrow spectral region an orthogonal rotation matrix with Euler angles  $\varphi$ ,  $\theta$ ,  $\psi$  can always be found such that  $\varepsilon$  can be diagonalized (Sect. 3.2.4.2). However, choosing a different spectral region, this rotation matrix will be different exhibiting the wavelength-dependent character and revealing monoclinic or triclinic properties. Considering for intrinsic monoclinic or triclinic properties by using projections  $\mathbf{U}$  and allowing for internal angles  $\alpha$ ,  $\beta$ ,  $\gamma$ , a wavelength-independent set of Euler angles  $\varphi$ ,  $\theta$ ,  $\psi$  must be found.

### 3.2.4.4 Connection between Intrinsic Polarizabilities and Dielectric Tensor

In general, symmetric  $\epsilon$ -tensor materials can be organized in three distinct groups with respect to their optical properties, as summarized in Table 3.1:

- Materials with a *cubic* symmetry are optically isotropic (for example, amorphous material). All three axes of major dielectric polarizabilities are equivalent and mutually orthogonal.
- Materials with *trigonal*, *tetragonal*, and *hexagonal* symmetry (three-fold, four-fold, and six-fold rotation axes exist, respectively) have uniaxial optical properties. All axes of major dielectric polarizabilities are mutually orthogonal, however, only two out of the three are equivalent axes. One dielectric principal axis coincides with the rotation axis, while any two remaining and equivalent directions are perpendicular to the principal axis of rotation.
- Materials with *orthorhombic*, *monoclinic*, and *triclinic* symmetry are optically biaxial. All three major dielectric polarizabilities are different.

**Table 3.1:** Symmetries and dielectric tensor properties of dielectric materials with symmetric dielectric tensor. For definition and explanation of major dielectric polarizabilities refer to Sect. 3.2.4.3.

Symmetry	Classification	Major Dielectric Polarizabilities ( $\epsilon_j = 1 + \varrho_j$ )	Internal Angles
isotropic	cubic	$\epsilon_a = \epsilon_b = \epsilon_c$	$\alpha = \beta = \gamma = 90^\circ$
uniaxial	trigonal	$\epsilon_a = \epsilon_b \neq \epsilon_c$	$\alpha = \beta = \gamma = 90^\circ$
	tetragonal		
	hexagonal		
biaxial	orthorhombic	$\epsilon_a \neq \epsilon_b \neq \epsilon_c$	$\alpha = \beta = \gamma = 90^\circ$
	monoclinic	$\varrho_a \neq \varrho_b \neq \varrho_c$	$\beta \neq \alpha = \gamma = 90^\circ$
	triclinic	$\varrho_a \neq \varrho_b \neq \varrho_c$	$\alpha \neq \beta \neq \gamma \neq 90^\circ$

If (3.16) of a transparent material is transformed to its principal axes (Sect. 3.2.4.2), the principal refractive indices  $n_j \equiv \sqrt{\epsilon_j}$  ( $j = a, b, c$ ) geometrically represent, in general, an ellipsoid, also called the index ellipsoid<sup>70,77</sup>. The terms uniaxial and biaxial refer to the number of optical axes. An optical axis is defined as the normal to a plane intersecting

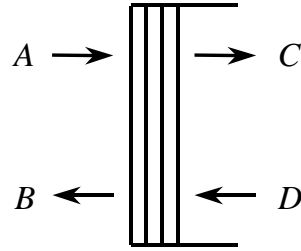


**Figure 3.5:** Schematic presentation of incident ( $A$ ), reflected ( $B$ ), and transmitted ( $C$ ) plane waves across a sample with plane parallel interfaces, and multiple layer stacks at the front side of the supporting substrate.  $D$  modes (if present) are incident from the right. The substrate may totally absorb  $C$  and/or  $D$ . Adapted from Schubert<sup>67</sup>.

the ellipsoid, where the circumference of the section is a circle, and its center coincides with the center of the ellipsoids. The optical axis presents a direction along which the speed of propagation is independent of polarization. Two such axes can be found in a general ellipsoid (biaxial), a spheroid has one (uniaxial), and a sphere an infinite number (isotropic). Materials with more than one principle dielectric constant exhibit birefringence.

### 3.2.5 Light Propagation in Layered Anisotropic Media

The electromagnetic response of stratified anisotropic materials with plane parallel boundaries can be conveniently calculated in either Jones or Mueller matrix presentation with a  $4 \times 4$  matrix approach, often cited as the Berreman-formalism<sup>60,66,67,78,79</sup>. Whereas the Jones and Mueller matrix formalism describe the measurable electromagnetic field components, the  $4 \times 4$  matrix algebra treats the electromagnetic field components within the sample, i.e, internal sample polarization-modifying processes responsible for the external polarizing sample properties. The response of the entire multiple-layered structure (Fig. 3.5) is described by a transfer matrix  $\mathbf{T}$ :

$$\begin{pmatrix} A_s \\ B_s \\ A_p \\ B_p \end{pmatrix} = \mathbf{T} \begin{pmatrix} C_s \\ D_s \\ C_p \\ D_p \end{pmatrix}. \quad (3.33)$$

A so-called characteristic transfer matrix,  $\mathbf{T}_p$ , accounts for the optical properties of

a single homogeneous layer within a stratified sample\*. Matrices for incident (ambient,  $\mathbf{L}_a$ ) and exit mediums ( $\mathbf{L}_f$ ) embed the layer stack according to the layer stack surrounding. The transfer matrix  $\mathbf{T}$  results from the ordered product of all  $m$  layers' matrices  $\mathbf{T}_p$  according to their position within the layer stack, starting and ending with the incident and exit matrices<sup>65,79</sup>:

$$\mathbf{T} = \mathbf{L}_a^{-1} \mathbf{T}_{p1}^{-1} \dots \mathbf{T}_{pm}^{-1} \mathbf{L}_f. \quad (3.34)$$

The ambient matrix

$$\mathbf{L}_a^{-1} = \frac{1}{2} \begin{pmatrix} 0 & 1 & -(n_a \cos \Phi_a)^{-1} & 0 \\ 0 & 1 & (n_a \cos \Phi_a)^{-1} & 0 \\ (\cos \Phi_a)^{-1} & 0 & 0 & 1/n_a \\ -(\cos \Phi_a)^{-1} & 0 & 0 & 1/n_a \end{pmatrix} \quad (3.35)$$

depends on the angle of incidence  $\Phi_a$  and the index of refraction  $n_a$  of the (isotropic) ambient material. The exit matrix depends on the angle of propagation within the exit medium  $\Phi_f$  and its complex valued index of refraction  $N_f = \sqrt{\varepsilon_f} = n_f + ik_f$ :

$$\mathbf{L}_f = \begin{pmatrix} 0 & 0 & \cos \Phi_f & -\cos \Phi_f \\ 1 & 1 & 0 & 0 \\ -N_f \cos \Phi_f & N_f \cos \Phi_f & 0 & 0 \\ 0 & 0 & N_f & N_f \end{pmatrix}. \quad (3.36)$$

The angle  $\Phi_f$  is calculated from Snell's law:

$$\cos \Phi_f = \sqrt{1 - ([n_a/N_f] \sin \Phi_a)^2}. \quad (3.37)$$

For a given layer of thickness  $d$  with index of refraction  $N$ , the matrix  $\mathbf{T}_p$  can be obtained from the exponential function

$$\mathbf{T}_p \equiv \exp \left\{ i \frac{\omega}{c} \mathbf{\Delta} d \right\}, \quad (3.38)$$

where  $c$  is the speed of light,  $\omega$  is the light wave orbital frequency, and  $\mathbf{\Delta}$  is the characteristic coefficient matrix of the layer. The characteristic coefficient matrix  $\mathbf{\Delta}$  is derived from Maxwell's equations as shown by Schubert<sup>79</sup> and depends on the dielectric

---

\*Further details and analytical solutions for  $\mathbf{T}_p$  can be found in the literature<sup>67,79</sup>.

tensor  $\boldsymbol{\varepsilon}$  and the wavevector component  $k_x$ :

$$\boldsymbol{\Delta} = \begin{pmatrix} -k_x \frac{\varepsilon_{zx}}{\varepsilon_{zz}} & -k_x \frac{\varepsilon_{zy}}{\varepsilon_{zz}} & 0 & 1 - \frac{k_x^2}{\varepsilon_{zz}} \\ 0 & 0 & -1 & 0 \\ \varepsilon_{yz} \frac{\varepsilon_{zx}}{\varepsilon_{zz}} - \varepsilon_{yx} & k_x^2 - \varepsilon_{yy} + \varepsilon_{yz} \frac{\varepsilon_{zy}}{\varepsilon_{zz}} & 0 & k_x \frac{\varepsilon_{yz}}{\varepsilon_{zz}} \\ \varepsilon_{xx} - \varepsilon_{xz} \frac{\varepsilon_{zx}}{\varepsilon_{zz}} & \varepsilon_{xy} - \varepsilon_{xz} \frac{\varepsilon_{zy}}{\varepsilon_{zz}} & 0 & -k_x \frac{\varepsilon_{xz}}{\varepsilon_{zz}} \end{pmatrix}, \quad (3.39)$$

$$k_x = n_a \sin \Phi_a. \quad (3.40)$$

The matrix  $\boldsymbol{\Delta}$  should not be confused with the real-valued ellipsometric parameter  $\Delta$ .  $\mathbf{T}_p$  connects the in-plane components of the electric and magnetic fields at layer interfaces separated by  $d$  and includes the effects of all multiple reflections if a part of the wave is traveling along a direction with no or weak absorption.  $\mathbf{T}_p$  is computed with  $\boldsymbol{\Delta}$  as input:

$$\mathbf{T}_p \equiv \exp \left\{ i \frac{\omega}{c} \boldsymbol{\Delta} d \right\} = \beta_0 \mathbf{E} + \beta_1 \boldsymbol{\Delta} + \beta_2 \boldsymbol{\Delta} \boldsymbol{\Delta} + \beta_3 \boldsymbol{\Delta} \boldsymbol{\Delta} \boldsymbol{\Delta}. \quad (3.41)$$

The scalars  $\beta_j$  are obtained from the following linear relations:

$$\exp \left\{ i \frac{\omega}{c} q_k d \right\} = \sum_{j=0}^3 \beta_j q_k^j, \quad k = 1 \dots 4, \quad (3.42)$$

where  $q_k$  denote the eigenvalues of  $\boldsymbol{\Delta}$  associated with one of the four electromagnetic eigenmodes  $\Xi_k$  within the layer ( $k = 1 \dots 4$ ). Two solutions have a positive real part and constitute the forward traveling plane waves with respect to the chosen laboratory coordinate system. The other solutions with negative real parts are due to the backward-traveling wave components.

In order to calculate  $\mathbf{T}_p$  parameters  $\varrho_a, \varrho_b, \varrho_c, \varphi, \theta, \psi$ , and  $\alpha, \beta, \gamma$  are needed, and which then represent the current orientation of the polarizability system ( $\mathbf{a}, \mathbf{b}, \mathbf{c}$ ) relative to the laboratory coordinate system (sample surface and plane of incidence) and relative to the ellipsometry measurement (plane of incidence and angle of incidence).

**Piecewise homogeneous layers.** Explicitly, the transfer matrix for a 3F2-STF (chevron with three layers) depicted in Fig. 3.8a reads

$$\mathbf{T} = \mathbf{L}_a^{-1} \mathbf{T}_{p1}^{-1} \mathbf{T}_{p2}^{-1} \mathbf{T}_{p3}^{-1} \mathbf{L}_f. \quad (3.43)$$

The STF is virtually separated into three layers with specific thickness  $d$  such that

each partial transfer matrix accounts for each slanted columnar layer, and together with incident and exit matrix result in the transfer matrix of the layer stack. Note that within each layer the dielectric tensor  $\boldsymbol{\varepsilon}$  of the (virtual) orthorhombic basis for  $\mathbf{a}, \mathbf{b}, \mathbf{c}$  is in diagonalized form when  $\varepsilon_a = \varepsilon_x$ ,  $\varepsilon_b = \varepsilon_y$ , and  $\varepsilon_c = \varepsilon_z$ , and oriented as depicted in Fig. 6.3. Hence, as discussed also later, if the slanting planes are parallel to the plane of incidence in Fig. 3.8a, the Euler angles within  $\mathbf{T}_{pj}$ , for example, are  $\varphi = +90^\circ$ ,  $\theta = +45^\circ$ , and  $\psi = 0^\circ$ .

**Continuously rotated layers.** Similar to the piecewise homogenous layer, the transfer matrix for a continuously rotated H-STF (Fig. 3.8b) explicitly takes the form

$$\mathbf{T} = \lim_{\substack{\delta d \rightarrow 0 \\ m \rightarrow \infty}} \mathbf{L}_a^{-1} \left( \prod_{j=1}^m \mathbf{T}_{pj}^{-1}(\delta d) \right) \mathbf{L}_f. \quad (3.44)$$

Here, it is implied in that  $\varrho_a, \varrho_b, \varrho_c, \alpha, \beta, \gamma, \theta$ , and  $\psi$  are identical for each layer and layers differ only by  $\delta\varphi$ . The total number  $m$  of partial transfer matrices depends on the level of discretization of the structure, i.e., in how many sublayers (slices) with thickness  $\delta d$  the structure is split up. A higher level of discretization results in more, thinner slices, and therefore finer approximations can be achieved. However, the computational effort may increase considerably.

## 3.2.6 Ellipsometry Model Description for Sculptured Thin Films

### 3.2.6.1 Homogeneous Biaxial Layer Approach

It is known that a thin film with columnar microstructure causes optical birefringence<sup>25</sup>. The microstructural asymmetry described as shape anisotropy (columns exhibit a slightly elliptical shape due to non-existence of structure shadowing in the direction perpendicular to the incoming particle flux) or preferentially bunched columns along the direction perpendicular to the deposition plane causes one setup of the so called form birefringence<sup>80</sup>. Also due to these “non-idealities” the optical nature of a slanted columnar thin film is biaxial. Hodgkinson and Wu<sup>81</sup> adapted the Herpin index method\* to transparent biaxial thin films and concluded that non-absorbing slanted columnar thin films (F1-STFs) can be considered as an effective medium with biaxial properties.

---

\*At one wavelength, a symmetrical thin-film combination (periodically stratified medium) is equivalent to a single film, characterized by an equivalent index and equivalent thickness<sup>82</sup>.



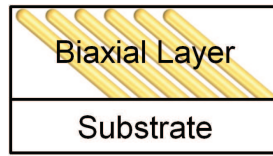


**Figure 3.6:** Optical layer model of an absorbing F1-STF (slanted columnar thin film). The anisotropic nanostructure can be described as an effective medium with a single biaxial layer on top of a substrate.

This consideration has been adapted and augmented here to create a generalized optical model, which is valid for slanted columnar thin films of any material (absorbing and non-absorbing). Examples for absorbing ( $k \neq 0$ ) STFs prepared from different metals are presented in Chap. 6.

The optical equivalent description for a F1-STF can be, in general, a single dielectrically homogeneous (along  $z$ ) biaxial layer, thereby describing an effective medium (Fig. 3.6). The biaxial layer comprises parameters thickness  $d$ , corresponding to the actual thickness of the nanostructured thin film, three complex, wavelength-dependent functions  $\varrho(\omega)_a$ ,  $\varrho(\omega)_b$ , and  $\varrho(\omega)_c$  pertinent to intrinsic axes  $\mathbf{a}$ ,  $\mathbf{b}$ , and  $\mathbf{c}$ , their internal angles  $\alpha$ ,  $\beta$ , and  $\gamma$ , and (external) Euler angles  $\varphi$ ,  $\theta$ , and  $\psi$  determining the orientation of the columns and sample during a particular measurement.

This homogenous biaxial layer approach has major advantages over other existing effective medium approximations: (i) no initial assumptions such as optical properties of the constituents or packaging fractions are necessary, (ii) it is valid for absorbing and non-absorbing materials, (iii) it does not depend on packaging fractions, and (iv) it does not depend on the structure size. Note that the actual structure size is disregarded in this homogenization approach. This procedure is considered valid since the lateral dimension of the nanostructures (diameter) is much smaller than the probing wavelength. Care must be taken when properties at shorter wavelengths are evaluated, because diffraction and scattering phenomena may be present.

### 3.2.6.2 Anisotropic Bruggeman Effective Medium Approximation

Effective medium approximations (EMAs) are physical models based on the properties and the relative fraction of its components and describe the macroscopic properties of a medium. The Bruggeman formalism, for example, is a homogenization process with absolute equality between the phases in mixture, and was originally developed for randomly oriented, in general, elliptical inclusions<sup>83</sup>. The Bruggeman EMA can also

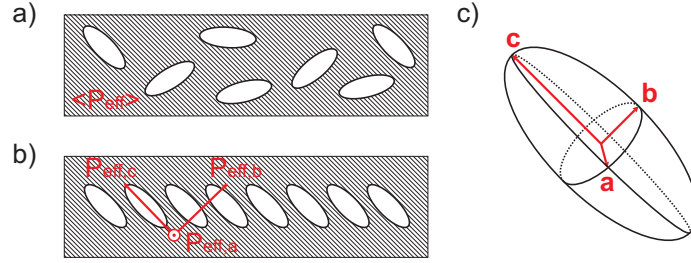


**Figure 3.7:** Effective medium scenarios with mixtures of elliptical inclusions [depicted in (c)] and a homogeneous host medium. The mixture with randomly oriented inclusions (a) exhibits an average effective polarizability  $\langle \mathbf{P}_{\text{eff}} \rangle$  whereas the mixture with aligned inclusions (b) shows anisotropic properties with three effective polarizabilities  $\mathbf{P}_{\text{eff},j}$  according to the shape of the inclusions.

be applied ad-hoc to highly oriented inclusions and is then called anisotropic Bruggeman EMA (AB-EMA). Depolarization factors  $L_a^D, L_b^D, L_c^D$  are representative for relative dimensions of elliptical inclusions along major polarizability axes  $\mathbf{a}, \mathbf{b}, \mathbf{c}$ . In case of a host medium with randomly oriented inclusions the mixture macroscopically exhibits an isotropic effective polarizability  $\langle \mathbf{P}_{\text{eff}} \rangle$  with an isotropic effective dielectric function  $\varepsilon_{\text{eff}}$  due to an averaging over all major polarizability axes. For aligned inclusions with ellipsoidal shape embedded in a host matrix the average for the biaxial (orthorhombic) effective dielectric functions  $\varepsilon_{\text{eff},a}, \varepsilon_{\text{eff},b}, \varepsilon_{\text{eff},c}$  is then only taken along  $\mathbf{a}, \mathbf{b}$ , and  $\mathbf{c}$ , respectively (Fig. 3.7). The AB-EMA formulae for the three effective major dielectric functions  $\varepsilon_{\text{eff},j} \equiv \varepsilon_j$  in implicit form are:

$$f \frac{\varepsilon_i - \varepsilon_{\text{eff},j}}{\varepsilon_{\text{eff},j} + L_j^D (\varepsilon_i - \varepsilon_{\text{eff},j})} + (1 - f) \frac{\varepsilon_m - \varepsilon_{\text{eff},j}}{\varepsilon_m + 2\varepsilon_{\text{eff},j}} = 0, \quad j = a, b, c, \quad (3.45)$$

where inclusions with permittivity  $\varepsilon_i$  and volume fraction  $f$  are located in a homogeneous environment matrix ( $\varepsilon_m$ ).  $\varepsilon_i$  and  $\varepsilon_m$  are the dielectric functions of the respective bulk material.  $L_j^D$  are the depolarization factors of the inclusion ellipsoids along the three orthogonal major polarizability axes  $\mathbf{a}, \mathbf{b}, \mathbf{c}$ , and the sum of all three depolarization factors must obey unity<sup>81,83</sup>:

$$1 = L_c^D + L_a^D + L_b^D. \quad (3.46)$$

Euler angles  $\varphi, \theta, \psi$  can then transform the Cartesian laboratory coordinate frame into the material coordinate frame.

The upper and lower bounds on  $\varepsilon_{\text{eff},j}$ , where the depolarization factors are 0 and 1,

correspond to minimum and maximum charge screening effects, respectively, and are called Wiener bounds<sup>84,85</sup>. These two cases can be understood considering capacitors connected either in parallel or in series. The effective permittivities of spheroids aligned along the substrate normal result then from (3.45) with  $L_a^D = L_b^D = 0.5$  and  $L_c^D = 0$ . Consequently, the case of  $L_a^D = L_b^D = L_c^D = \frac{1}{3}$  corresponds to spherical inclusions<sup>81,86,87</sup>.

In general, the thin homogenization approach applies to orthorhombic and higher symmetry cases only and monoclinic and triclinic properties cannot be described with the AB-EMA. Moreover, the AB-EMA is only valid in the long wavelength approximation and therefore no accurate values can be determined if the structure size reaches the order of the wavelength of the probing light<sup>64,83,88</sup>.

### 3.2.6.3 Piecewise Homogeneous Biaxial Layer Approach

If substrate rotation is involved during the growth process of STFs, a single biaxial layer accounting for the film is not sufficient anymore to describe the dielectric polarization response\*. For the piecewise homogeneous biaxial layer approach two types of STFs are distinguished here: (i) F-STFs (except F1; fabricated with sequential substrate rotations) and (ii) H-STFs (fabricated with continuous substrate rotation). It is assumed that the STF is made of  $m$  F1-STF slices, where within each slice (layer) the dielectric properties are homogeneous<sup>27,89</sup>.

**F-STFs.** F-STFs (all but F1) are grown while the substrate is rotated step-wise (abruptly) after a certain pause time. If a sequential substrate rotation of  $180^\circ$  is employed, for example, the resulting F2-STFs, also called chevrons or zig-zags, can be considered as stratified (or a cascade of) F1-STFs with opposite slanting directions in adjacent slabs. Consequently, the optical model for the chevron thin film with three layers (3F2-STF)<sup>†</sup>, depicted in Fig. 3.8a, consists of three homogeneous anisotropic (biaxial) layers on top of a layer accounting for the substrate. The Euler angles for each layer  $(\varphi_j, \theta_j, \psi_j)$ , which transform the Cartesian coordinate system  $(x, y, z)$  into the sample coordinates  $(\xi, \eta, \zeta)$ , represent the orientation of each slanted column (building block) in the nanostructure. In case the angle of the incoming particle flux  $\theta_i$  was kept constant during deposition, a common dielectric tensor, with three major polarizabil-

---

\*Very fast substrate rotation ( $< 2$  nm vertical growth per revolution) results in V-STFs, i.e., a screw degenerates to a straight column because the pitch is too small. Optical properties of V-STFs are not discussed in this thesis, however, the nanostructured film has uniaxial properties with the ordinary dielectric constant in the substrate interface and the extraordinary along the columns and normal to the substrate.

<sup>†</sup>For nomenclature see Table 2.1.

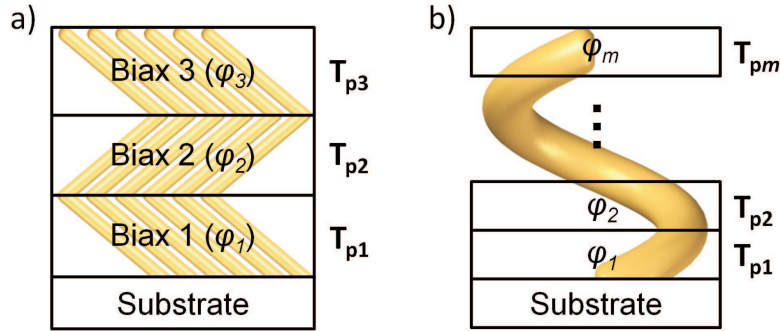


**Figure 3.8:** Optical layer model for arbitrarily oriented STFs. (a) a 3F2-STF (chevron with three layers), for example, is optically modeled with three biaxial layers with alternating orientations. (b) a H-STF is approximated by  $n$  biaxial layers, which are rotated with respect to each other by  $\delta\varphi$ .  $\mathbf{T}_{pm}$  corresponds to the partial transfer matrix in the  $4 \times 4$  algebra for layer  $m$ , and depends on  $\varrho_a, \varrho_b, \varrho_c, \alpha, \beta, \gamma, \varphi, \theta, \psi$ , and  $d$ .

ities  $\varrho_a, \varrho_b, \varrho_c$  pertinent to the intrinsic axes **a**, **b**, **c**, and internal angles  $\alpha, \beta, \gamma$  and Euler angles  $\varphi, \theta, \psi$  can be assigned to each biaxial layer. Deposition at constant  $\theta_i$  results in equal packaging fractions in subsequent layers and therefore common major polarizabilities may be assumed. Furthermore, all layers have an individual thickness parameter  $d_j$  such that the total thickness is equal to the overall film thickness ( $d = d_1 + d_2 + \dots + d_m$ ). This approach is valid, in general, for arbitrarily oriented F-STFs and examples are presented in Sect. 6.3. As will be shown later, the Euler angle  $\theta$  is identical to the geometrical slanting angle,  $\varphi$  is the rotation of the slanting plane with respect to the laboratory coordinate frame, and  $\psi$  is found to be zero.

**H-STFs.** If the substrate is continuously rotating around the normal during deposition, helical STFs (H-STFs) are growing since the sample rotation is equivalent to a constant angular change of the incoming vapor flux direction around the substrate normal and thus the self-shadowed regions change dynamically. H-STFs, schematically shown in Fig. 3.8b, represent rotationally inhomogeneous anisotropic material with a twist along the sample normal. Such chiral nanostructured thin films can be considered as “frozen” cholesteric liquid crystals<sup>79,90,91</sup>. Here the dielectric tensor  $\varepsilon(z)$  depends on the spatial position with respect to the  $z$  axis. In order to model the electromagnetic plane wave response of H-STFs the thin film has to be virtually separated into  $m$  homogeneous anisotropic layers with subsequently shifted Euler angle parameters  $\varphi_1, \varphi_2, \dots, \varphi_m$  with individual thickness parameters  $\delta d = d/m$ . These layers represent piecewise rotation with respect to each other by  $\delta\varphi$  to resemble the twisted character

such that

$$\boldsymbol{\varepsilon}_j = (z) = \mathbf{A}(\varphi_j)\boldsymbol{\varepsilon}\mathbf{A}(\varphi_j)^{-1}, \quad j = 1, \dots, m. \quad (3.47)$$

Here,  $\boldsymbol{\varepsilon}_j$  is the dielectric function tensor that describes the first virtual layer corresponding to its orientation during measurement with respect to the plane of incidence. Physical quantities such as principal dielectric functions (as a function of photon energy and  $z$ ), orientation, overall thickness, handedness, and thickness of the helical structure can be thereby retrieved from the ellipsometry model calculations. In contrast to F-STFs, for H-STF the Euler angle  $\psi$  is found to be not equal to zero (Sect. 6.3.4).

### 3.2.7 Ellipsometry Data Analysis

The Jones ( $r_{ij}$ ) or Mueller ( $M_{kl}$ ) matrix elements are functions of the photon energy  $\hbar\omega$ , the (major-axes) dielectric functions  $\varepsilon_j(\omega)^*$  ( $j = a, b, c$ ) and its Euler orientation angles  $\psi$ ,  $\varphi$ , and  $\theta$ , the thickness  $d$ , the ambient material's dielectric function, and the angle of incidence  $\Phi_a$ . For multiple layers,  $\varepsilon_j$ , the Euler angles, internal polarizability angles  $(\alpha, \beta, \gamma)$ , as well as  $d$  may be layer-specific. The standard model for analyzing ellipsometry data is based on a sequence of homogeneous (isotropic or anisotropic) layers with smooth and parallel interfaces. In case of an anisotropic sample, the ellipsometric measurement depends also on the orientation of axes  $\mathbf{a}$ ,  $\mathbf{b}$ ,  $\mathbf{c}$  with respect to the plane of incidence, and the polarization state of the incident light beam<sup>60,68,79</sup>. Depending on the parameters of interest and the sample properties (layer sequence, anisotropy) different analysis approaches can be employed.

#### 3.2.7.1 Wavelength-by-Wavelength Analysis

Traditionally, wavelength-by-wavelength best-match model calculations (point-by-point best-match model calculations) are performed when the dielectric function values of interest are extracted from the experimental data for each wavelength, and independent of all other spectral data points. For this procedure, the thickness of the particular layer as well as the dielectric functions and the thicknesses of all other sample constituents have to be known. However, in order to obtain values of physically relevant parameters (such as critical point energies and broadening parameters) and to ensure Kramers-Kronig consistency the dielectric function obtained from the point-by-point best-match model calculation needs to be compared with a line-shape model.

---

\*For materials with monoclinic and triclinic symmetry  $\varepsilon_j(\omega)$  depend on the polarization functions  $\varrho_a, \varrho_b, \varrho_c$  and their non-Cartesian axes  $\mathbf{a}$ ,  $\mathbf{b}$ , and  $\mathbf{c}$  as described in Sect. 3.2.4.

### 3.2.7.2 Parameterized Model Dielectric Function Analysis

A commonly employed, robust procedure is matching parameterized model dielectric functions (MDFs) to experimental data simultaneously for all spectral data points. This provides a direct connection between measured data and physical parameters of interest. Parametric models further prevent wavelength-by-wavelength measurement noise from becoming part of the extracted dielectric functions and greatly reduce the number of free parameters. With the use of parametric models a certain risk is involved for subtle spectral features to be neglected by the lineshape of the model function. Nevertheless, parameterizations of  $\varepsilon_j$  based on a physical model is the best choice for ellipsometry data analysis, especially when the wavelength-by-wavelength best-match model calculation method is inapplicable.

In this work, two physical lineshape parameterization models have been used in order to match experimental data in the measured visible to near-infrared spectral region.

**Harmonic Lorentzian oscillator model.** A simple calculation of the complex dielectric function assumes that the response of the material to electromagnetic radiation can be represented by an ensemble of non-interacting harmonic oscillators. The harmonic Lorentz oscillator model equation is given by

$$\varepsilon(E) = (n + ik)^2 = \varepsilon_{\text{off}} + \sum_j \frac{A_j}{E_{c,j}^2 - E^2 + i\gamma_j E}, \quad (3.48)$$

for the dielectric function expressed in terms of the photon energy  $E$ . Parameters  $A_j$ ,  $E_{c,j}$ ,  $\gamma_j$  are determined in the best-match model calculation and denote amplitude, center energy, and broadening of the  $j$ th oscillator, respectively.  $\varepsilon_{\text{off}}$  is an offset parameter to account for contributions outside the measured spectral range.

**Drude model for free-charge carriers.** The classical Drude expression for free-charge carrier contributions is given by setting  $E_c = 0$  in (3.48):

$$\varepsilon(E) = (n + ik)^2 = -\frac{N_v q^2}{m_{\text{eff}} \varepsilon_0 (E^2 - i\gamma E)}. \quad (3.49)$$

The amplitude parameter  $A = N_v q^2 / m_{\text{eff}} \varepsilon_0$ , where  $m_{\text{eff}}$  denotes the effective mass of the free-charge carriers with volume-density  $N_v$ . The vacuum dielectric permittivity and the charge of the free-charge carriers is given by  $\varepsilon_0$  and  $q$ , respectively. The broadening parameter  $\gamma$  is related to the energy-independent relaxation time  $\tau$  and the free-charge

carrier mobility  $\mu$  as

$$\gamma = \tau^{-1} = \frac{q}{m_{\text{eff}}\mu}. \quad (3.50)$$

Equation (3.49) leads with  $\varepsilon = i\sigma/(\varepsilon_0 E)$  in the low frequency limit ( $E \rightarrow 0$ ) to the classical DC Drude conductivity expression  $\sigma_0 = N_v q^2 \tau / m_{\text{eff}}$ <sup>63,67</sup>.

### 3.2.7.3 Ellipsometry Test Functions

During the data analysis model parameters are varied until calculated and measured data match as close as possible (best-match model calculation). For fast convergence the Levenberg-Marquardt algorithm can be used, for example, in order to vary the adjustable model parameters until the weighted test function  $\xi_{\text{SE}}$  (mean square error, MSE) is minimized (maximum likelihood approach)<sup>92</sup>:

$$\xi_{\text{SE}}^2 = \frac{1}{2S - K + 1} \sum_{j=1}^S \left[ \left( \frac{\Psi_j - \Psi_j^c}{\sigma_j^\Psi} \right)^2 + \left( \frac{\Delta_j - \Delta_j^c}{\sigma_j^\Delta} \right)^2 \right], \quad (3.51)$$

where  $S$  denotes the number of measured data pairs  $(\Psi_j, \Delta_j)$ ,  $K$  is the number of real-valued model parameters,  $\Psi_j^c$  and  $\Delta_j^c$  are the calculated ellipsometric parameters at photon energy  $E = \hbar\omega_j$ , and  $(\sigma_j^\Psi, \sigma_j^\Delta)$  are the standard deviations obtained during the measurement<sup>93,94</sup>.

For the generalized ellipsometry situation, the test function is set up accordingly for the Jones ( $\xi_{\text{GE-J}}^2$ ) and Mueller ( $\xi_{\text{GE-M}}^2$ ) matrix presentation:

$$\begin{aligned} \xi_{\text{GE-J}}^2 = & \frac{1}{6S - K + 1} \sum_{j=1}^S \left[ \left( \frac{\Psi_{pp,j} - \Psi_{pp,j}^c}{\sigma_{pp,j}^\Psi} \right)^2 + \left( \frac{\Psi_{ps,j} - \Psi_{ps,j}^c}{\sigma_{ps,j}^\Psi} \right)^2 + \left( \frac{\Psi_{sp,j} - \Psi_{sp,j}^c}{\sigma_{sp,j}^\Psi} \right)^2 \right] \\ & + \frac{1}{6S - K + 1} \sum_{j=1}^S \left[ \left( \frac{\Delta_{pp,j} - \Delta_{pp,j}^c}{\sigma_{pp,j}^\Delta} \right)^2 + \left( \frac{\Delta_{ps,j} - \Delta_{ps,j}^c}{\sigma_{ps,j}^\Delta} \right)^2 + \left( \frac{\Delta_{sp,j} - \Delta_{sp,j}^c}{\sigma_{sp,j}^\Delta} \right)^2 \right], \end{aligned} \quad (3.52)$$

$$\xi_{\text{GE-M}}^2 = \frac{1}{16S - K} \sum_{j=1}^S \sum_{k=0}^3 \sum_{l=0}^3 \left( \frac{M_{kl,j} - M_{kl,j}^c}{\sigma_j^{M_{kl}}} \right)^2. \quad (3.53)$$

Similar to standard ellipsometry, in addition to  $\Psi_{pp}$ ,  $\Delta_{pp}$ ,  $\Psi_{ps}$ ,  $\Delta_{ps}$ ,  $\Psi_{sp}$ ,  $\Delta_{sp}$ , and  $M_{kl}$  ( $k, l = 0 \dots 3$ ), their respective standard deviations  $\sigma^\Psi$ ,  $\sigma^\Delta$ , and  $\sigma^{M_{kl}}$  are measured and propagated into the test functions.

Note that GE MSE values for anisotropic samples cannot be directly compared with MSE values obtained with standard ellipsometry best-match model calculations for isotropic samples, where the ‘‘rule-of-thumb’’ indicates best achievement for MSE near

or less than unity. The data set included for GE model analysis is generally larger than for SE analysis. In GE data analysis, in addition to closeness of the best-match model data to a given particular measured spectrum, match to the same data set versus sample rotation as well as its angle of incidence dependence is of equal importance.

In the result of the regression analysis, the correlation between different adjusted parameters and the confidence limit of the individual model parameter are of particular importance. Both quantities can be derived from the curvature matrix  $\alpha$ :

$$\alpha_{kl} = \sum_{j=1}^N \left( \frac{1}{\sigma_{\Psi_j}^2} \frac{\delta\Psi_j^C \delta\Psi_j^C}{\delta\alpha_k \delta\alpha_l} + \frac{1}{\sigma_{\Delta_j}^2} \frac{\delta\Delta_j^C \delta\Delta_j^C}{\Delta\alpha_k \Delta\alpha_l} \right), \quad (3.54)$$

which is the inverse of the covariance matrix  $\mathbf{C} \equiv \alpha^{-1}$ . The standard 90% confidence limit  $L$  for the  $j$ th parameter is then given by<sup>95</sup>

$$L_j = \pm 1.65 \sqrt{C_{jj}} \xi, \quad (3.55)$$

where 1.65 is a statistically derived constant. Since  $\xi$  (MSE) has been also introduced into the expression, the confidence limits become larger when the quality of the best-match model calculation degrades. If not otherwise stated, the uncertainties given in this work are the respective confidence limits. The parameter correlation coefficients  $\eta_{jk}$  can be obtained from  $\mathbf{C}$  by:

$$\eta_{jk} = \frac{C_{jk}}{\sqrt{C_{jj}} \sqrt{C_{kk}}}. \quad (3.56)$$

A value of  $\eta_{jk} \sim 1$  indicates correlation between the  $j$ th and the  $k$ th parameter. For correct and unique analysis no or only small correlation may occur between model parameters.

#### 3.2.7.4 Multi-Sample and Multi-Sample-Configuration Analysis

If model parameters correlate or confidence limits are too large, either modifications to the model or other options have to be considered such as including further ellipsometric experimental data from similar samples and employ the multi-sample-analysis technique. In this approach, measured data sets of multiple samples are simultaneously analyzed with different models, which share a common set of parameters. These common parameters are assumed to be identical for each individual sample.

In a similar manner, measurement data obtained from a single sample but with a



modified external parameter (applied magnetic field or temperature, for example) can be analyzed simultaneously. The effect of the varied quantity on the MDF has to be known and implemented in the model analysis. This approach is referred here to as multi-sample-configuration analysis.

### 3.2.7.5 Difference Spectra Analysis

The difference spectra analysis is particularly useful when changes of the sample's optical response due to a modification of an external parameter are small. Difference spectra are obtained by subtracting measured data sets acquired, for example, at opposite (externally applied) magnetic field directions. This approach reveals most directly the change in the optical response upon variation of the external parameter.

### 3.2.8 Experimental Setup

Spectroscopic ellipsometry measurements were performed with a commercial J. A. Woollam Co., Inc. M-2000VI<sup>®</sup> multichannel ellipsometer covering the visible to near infrared spectral region, and which is mounted on an automated stage (Fig. 3.9). The polarization state generator unit (1) comprises a polarizer and rotating compensator and a 50 W halogen lamp serves as the light source. After reflection off the sample surface the light passes a rotating analyzer (part of the polarization state analyzer, 2), is spectrally separated by a prism and directed onto two CCD arrays. One CCD array detects a total of 390 wavelength within the spectral range of 371 to 1000 nm (1.24 to 3.34 eV) whereas the second one detects another 200 wavelength between 1000 and 1690 nm (0.73 to 1.24 eV). Hence, data for all 590 wavelength can be acquired at the same time. The rotating-compensator-type ellipsometer is capable of measuring 11 out of 16 Mueller matrix elements normalized to  $M_{11}$  (except for elements in fourth row)\*. The sample tilt adjustment procedure is done with an additional alignment laser and four-quadrant detector (3) and is followed by a computer-controlled  $z$ -alignment (sample height adjustment). The motorized goniometer together with the horizontal sample stage (4) enables automated angle resolved (angle of incidence  $\Phi_a$  and rotation angle  $\phi$ ) measurements, where  $\Phi_a$  can be varied from  $45^\circ$  to  $90^\circ$  and  $\phi$  from  $0^\circ$  to  $360^\circ$ . Furthermore, the M-2000VI<sup>®</sup> is equipped with a beam shutter to perform automated DC offset calibrations<sup>†</sup>. The WVASE32<sup>®</sup> software, which controls the ellipsometer hard-

---

\*Mueller matrix elements of the fourth row cannot be resolved because the polarization state analyzer (2) does not comprise a rotating compensator<sup>63,64</sup>.

<sup>†</sup>A DC offset calibration determines the detector noise level without source illumination.

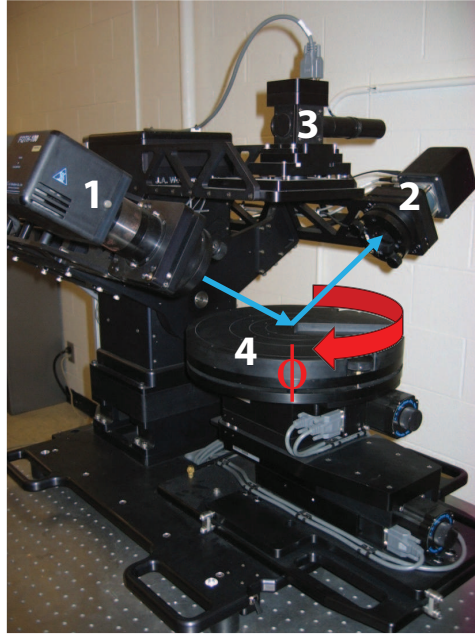


**Figure 3.9:** J. A. Woollam M-2000VI® ellipsometer (1,2) with automated rotation stage (4) and alignment laser (3) for automated  $z$ -alignment.

ware, allows for programming customized measurement routines through the add-on program WVASEscript<sup>76</sup>.

### 3.3 Magneto-Optical Generalized Ellipsometry

For linear-response magneto-optical characterization of magnetic material determination of the entire dielectric function tensor  $\epsilon$  is desirable. Magnetized media are in general optically anisotropic due to non-reciprocal magneto-optical properties. The aim here is to determine the dielectric function tensor of a magnetized sample [ $\epsilon(\mathcal{M})$ ] and ultimately the magnetization kinetics and direction in anisotropic STF's exposed to an external magnetizing field  $\mathbf{H}$  [ $\mathcal{M}(\mathbf{H})$ ]. Generalized magneto-optic ellipsometry (MOGE), in principle, allows for complete magneto-optical characterization including the determination of the magnetization orientation of arbitrarily magnetized anisotropic stratified media<sup>96,97</sup>. For this however, a meaningful connection between the dielectric tensor elements and the sample magnetization  $\mathcal{M} = \mathcal{M}(m_x, m_y, m_z)$  must be made in addition to functions  $\mathcal{M}(\mathbf{H})$ . In particular, functions  $\mathcal{M}(\mathbf{H})$  render highly non-linear functions with hysteresis due to preceding magnitude and direction of external magnetic fields (sample history).

### 3.3.1 Magneto-Optical Dielectric Tensor

In the presence of an external magnetic field, the dielectric tensor has to be augmented by off-diagonal complex parameters\*, which account for magneto-optical activity.  $\boldsymbol{\varepsilon}$  becomes non-symmetrical and takes the general form<sup>99</sup>

$$\boldsymbol{\varepsilon} = \boldsymbol{\varepsilon}^{\text{D}} + \boldsymbol{\varepsilon}^{\text{MO}} = \begin{pmatrix} \varepsilon_{xx} & \varepsilon_{xy} & \varepsilon_{xz} \\ \varepsilon_{xy} & \varepsilon_{yy} & \varepsilon_{yz} \\ \varepsilon_{xz} & \varepsilon_{yz} & \varepsilon_{zz} \end{pmatrix} + \begin{pmatrix} 0 & i\varepsilon_{xy}^{\text{P}} & -i\varepsilon_{xz}^{\text{T}} \\ -i\varepsilon_{xy}^{\text{P}} & 0 & i\varepsilon_{yz}^{\text{L}} \\ i\varepsilon_{xz}^{\text{T}} & -i\varepsilon_{yz}^{\text{L}} & 0 \end{pmatrix}. \quad (3.57)$$

This expression is valid for a homogeneous medium of any symmetry, and which may be uniformly magnetized at an arbitrary direction. The main diagonal elements of  $\boldsymbol{\varepsilon}^{\text{D}}$  represent the dielectric part of the tensor and are independent of  $\mathcal{M}$ . The off-diagonal elements  $\varepsilon_{xy}^{\text{P}}$ ,  $\varepsilon_{xz}^{\text{T}}$ , and  $\varepsilon_{yz}^{\text{L}}$  of the magneto-optical permittivity tensor  $\boldsymbol{\varepsilon}^{\text{MO}}(\mathcal{M})$  are assumed to be linear functions of  $\mathcal{M}$  and account for a magnetization component along directions  $z$ ,  $y$ , and  $x$ , respectively<sup>†</sup>. If the magnetization is along one direction, one of the primary Kerr geometries (discussed below) is represented, and only the respective off-diagonal element will be different from zero.

### 3.3.2 Primary Magneto-Optical Effects

The most important magneto-optical effects for optical recording and optical communication are Faraday and Kerr effects. Faraday effects are observed in transmission whereas the equivalent phenomenon in reflection geometry are so-called Kerr effects<sup>100</sup>. Due to the nature of the samples discussed in this thesis (STFs on Si substrates) and the corresponding reflection-type measurements only the Kerr effect shall be discussed in the following. Phenomenologically, Kerr rotation is observed as a rotation of the polarization plane of the reflected light, when a linearly polarized electromagnetic wave is reflected from the surface of a magnetized material, where the magnetization  $\mathcal{M}$  is assumed to be perpendicular to the surface. This rotation originates from the difference in the electronic transition matrix element selection rule for incident right and left circularly polarized light (propagating eigenmodes). The direction of the rotation angle depends also on the direction of  $\mathcal{M}$  such that the Kerr rotation can be utilized to optically read out information stored in form of magnetization directions<sup>101</sup>. In contrast to chiral media, which also rotate the polarization plane upon reflection or transmission,

\*The response of  $\mathcal{M}$  to  $\mathbf{H}$  is restricted to frequencies of the order of the paramagnetic relaxation frequencies. Therefore,  $\mathcal{M}$  cannot follow at variations of optical frequencies and the relative magnetic permeability is always taken as unity and hence does not need to be taken into account here<sup>98</sup>.

<sup>†</sup>Directions  $x$ ,  $y$ , and  $z$  are defined in Fig. 3.2.

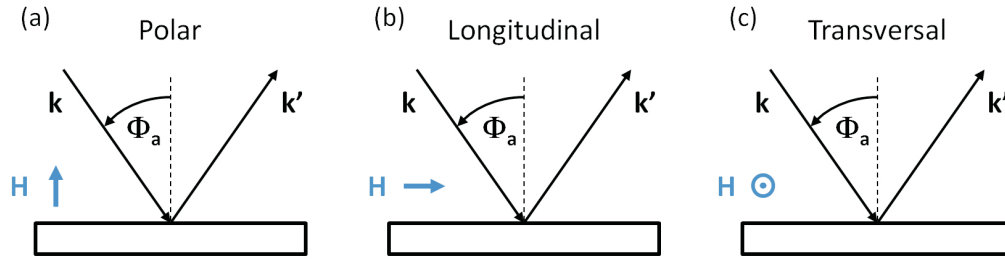


**Figure 3.10:** Basic geometries of magneto-optical generalized ellipsometry in reflection (“Kerr geometries”). In (a) the polar configuration the magnetic field  $\mathbf{H}$  is perpendicular to the sample surface. For the longitudinal configuration (b) the vector  $\mathbf{H}$  is parallel to the sample surface and the plane of incidence. (c) the transverse configuration is with  $\mathbf{H}$  parallel to the sample surface and perpendicular to the plane of incidence.

and which are non-reciprocal in space, magneto-optical effects are non-reciprocal in time\*. Hence, if the reflected beam is returned by a mirror, for example, and reflects again off the magnetized sample to the starting point, the total polarization rotation is doubled.

Three primary geometries of the Kerr effect can be distinguished by the magnetic field orientation<sup>103</sup> and are illustrated in Fig. 3.10. Traditionally, these geometries were associated with zero angle of incidence. Because ellipsometry is performed at oblique angles of incidence the terms polar, longitudinal, and transversal will be kept when addressing magneto-optical generalized ellipsometry measurements. The sample magnetization  $\mathcal{M}$  is not necessary parallel to the external magnetizing field  $\mathbf{H}$  for STFs, hence the geometries only refer to direction of  $\mathbf{H}$  with respect to the laboratory coordinate system.

- (a) **Polar.** A linearly polarized beam of light falls onto a surface, which is magnetized in a direction perpendicular to the surface (out-of-plane).
- (b) **Longitudinal.** An obliquely incident electromagnetic wave strikes the surface, which is magnetized along the plane of incidence (in-plane).
- (c) **Transversal.** The geometry is the same as in the longitudinal case, except that in-plane magnetization is perpendicular to the plane of incidence.

\*Optically active (chiral) media rotate the polarization state because the spatial (mirror) symmetry in the material is broken. Non-reciprocity in magnetized samples is caused because the time symmetry is broken (rotation of electron reverses sense upon time-reversal)<sup>102</sup>.

### 3.3.3 Kerr Rotation and Kerr Ellipticity

Traditionally measured Kerr rotation  $\theta_K$  and ellipticity  $\varepsilon_K$  parameters are (in the notation used here) identical to the magnetic field-induced changes in the normalized complex off-diagonal Jones matrix element  $R_{ps} = r_{ps}/r_{pp}$  at normal incidence (i.e.,  $\theta_K + i\varepsilon_K = R_{ps}[\mu_0 H] - R_{ps}[\mu_0 H = 0 \text{ T}]$ )<sup>97,104</sup>. Because  $R_{ps}[\mu_0 H = 0]$  is not zero in general for anisotropic samples, the Kerr effect depends on the anisotropic optical properties of the sample, and is a function of the incident polarization state and the sample orientation with respect to the plane of incidence.

### 3.3.4 Magneto-Optical Generalized Ellipsometry Model Description

Samples from ferromagnetic materials such as Co, for example, can be magnetized in an external magnetic field  $\mathbf{H}$ . In case of a magnetized sample the optical model valid for describing the polarization response without applied magnetic field (Sect. 3.2.6) has to be augmented to account for the additional magneto-optical contributions  $[\varepsilon(\mathcal{M})]$ . In particular, the dielectric tensor of each layer with material properties altered by an external magnetic field requires additional magneto-optical off-diagonal parameters as described in (3.57).

### 3.3.5 Experimental Setup

#### 3.3.5.1 Magneto-Optical Kerr-Effect Configuration

Magneto-optical spectroscopic Mueller matrix measurements were performed with a commercial ellipsometer (V-VASE<sup>®</sup>, J. A. Woollam Co., Inc.) combined with a water-cooled, current-controlled, room-temperature, Helmholtz-type magnet (Applied Magnetics Laboratory, Inc.).

The beam steering mirror used in the polar and longitudinal Kerr-effect configuration (see below), needs to be characterized and included in the model analysis procedure. A measurement without field ( $\mu_0 H = 0$ ) has to be performed to determine mirror surface angular rotations of the laboratory coordinate frame and thereby the  $p$  and  $s$  amplitude and phase changes imposed by the mirror<sup>105</sup>. These parameters are considered in the optical model.

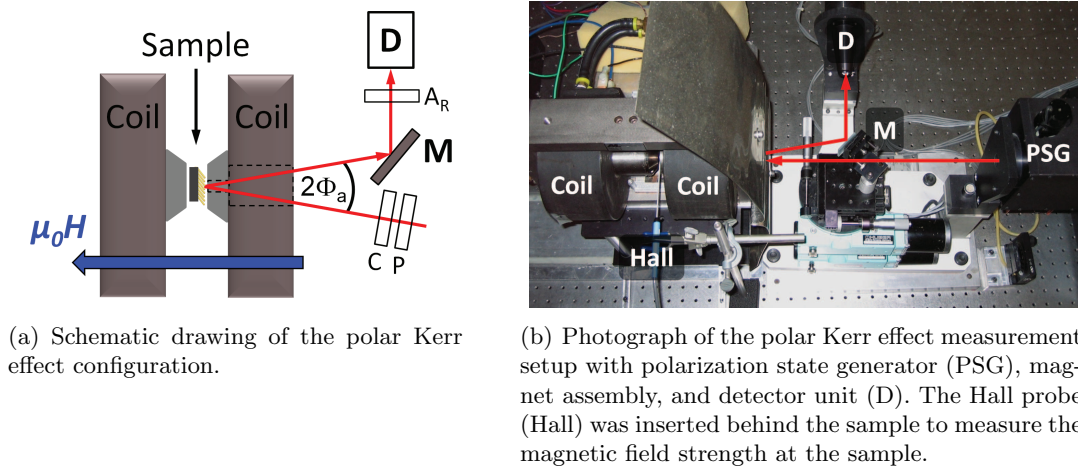
**Ellipsometer.** The V-VASE<sup>®</sup> is a commercially available rotating analyzer variable angle of incidence ellipsometer covering the near infrared to ultraviolet spectral region ( $\sim 0.75$  to  $\sim 5.5$  eV). The computer-controlled system is equipped with an automated

compensator (Berek waveplate) in the polarization state generator. This configuration is capable of measuring 11 out of 16 Mueller matrix elements normalized to  $M_{11}$  (except for elements in fourth row). A 75 W Xe short arc lamp is used as a light source followed by a monochromator, which allows for precise photon energy selection. In order to cover the specified spectral range a tandem detector is used, comprising two photodiodes. The beam diameter at the sample surface is approximately 4 mm. The sample tilt is manually adjusted at normal incidence using a detachable four-quadrant detector module.

**Magnet.** The commercially available Helmholtz-type electromagnet consists of two water-cooled coils made of copper conductors. One of the pole pieces is variable to adjust the air-gap width between 0 and 75 mm and the other one has a successively decreasing center bore with a minimum diameter of approximately 6 mm. The strength of the magnetic field between the poles (with vanadium permendur pole caps) is tunable from  $-2.3 < \mu_0 H < +2.3$  T (at  $\pm 14$  A and 60 V) by controlling the current through the coils and also by varying the air-gap between the pole pieces. The magnet is mounted on a horizontally rotatable stage, which allows for different magnetic field directions.

**Polar Kerr-Effect Configuration.** In the traditional polar geometry (Fig. 3.11) the external magnetic field is parallel to the substrate normal ( $z$ -axis). In this configuration, the pole cap of the fixed pole piece has to be detached. The sample was attached to a glass slide fixed to a tilt stage, which can be adjusted in height. This assembly was mounted onto a  $x$ - $y$ -translation stage and introduced into the air-gap. Subsequently, the air-gap was reduced to a minimum by moving the adjustable pole piece to obtain maximum magnetic field strength. Polarized light passes through the center bore in the fixed coil core and the reflected beam from the sample is guided by a plane aluminum mirror into the fixed detector. The mirror is attached to a tilt stage, which is mounted on an  $x$ ,  $y$ -stage for precise alignment. This setup allows for measurements near normal incidence ( $\Phi_a = 3^\circ$ ) without blocking the beam by either mirror or center bore. The magnetic-field strength was measured by a transverse electrical Hall probe (421 Gaussmeter, LakeShore Cryotronics, Inc.), which was permanently mounted in between the poles and behind the sample to ensure accurate and stable magnetic fields during optical measurements.

**Longitudinal Kerr-Effect Configuration.** In the longitudinal Kerr geometry depicted in Fig. 3.12 the external magnetic field is in the sample surface and parallel to the plane



(a) Schematic drawing of the polar Kerr effect configuration.

(b) Photograph of the polar Kerr effect measurement setup with polarization state generator (PSG), magnet assembly, and detector unit (D). The Hall probe (Hall) was inserted behind the sample to measure the magnetic field strength at the sample.

**Figure 3.11:** In-house built magneto-optical polar Kerr effect configuration. Light emitted by a xenon short arc lamp passes polarizer (P) and compensator (C), illuminates the sample through a center bore in one pole and is reflected off the sample at an angle of incidence  $\Phi_a = 3^\circ$ , and directed by a mirror (M) through a rotating analyzer ( $A_R$ ) into the detector (D). The polarization state generator (PSG) comprises the lamp, P and C.

of incidence (along the  $x$ -axis). Hence, the magnet is rotated by  $90^\circ$  counterclockwise with respect to the polar geometry. Both pole pieces are attached in this configuration. This configuration allows for a maximum angle of incidence\* of  $\Phi_a = 18.5^\circ$  (without blocking the beam). The detector arm of the ellipsometer system is rotated by  $180^\circ$  with respect to the polar setup. The sample was mounted on one flat end of a thin aluminum rod, which was attached to a tilt stage for sample alignment. An  $x$ - $y$ -translation stage base allows for careful introduction into the air-gap. The same adjustable aluminum mirror was used as with the polar configuration and also a Hall probe was constantly present between the poles and behind the sample.

### 3.3.5.2 Octupole Vector-Magnet Setup

Spectroscopic vector magneto-optical generalized ellipsometry (VMOGE) have been performed<sup>†</sup> on a setup comprising a V-VASE<sup>®</sup> ellipsometer (discussed in Sect. 3.3.5.1) and a computer-controlled octupole vector-magnet (Anderberg & Mod er Accelerator

\*Typically, in thin solid films the longitudinal Kerr effect gives rise to polarization changes that are an order of magnitude less pronounced than those associated with the polar Kerr effect<sup>106</sup>. Achieving a larger angle of incidence is desirable due to increasing sensitivity to a possible longitudinal component<sup>100</sup>.

<sup>†</sup>Measurements were conducted at the Research Center Rossendorf, Germany, by collaborator Dr. H. Schmidt.

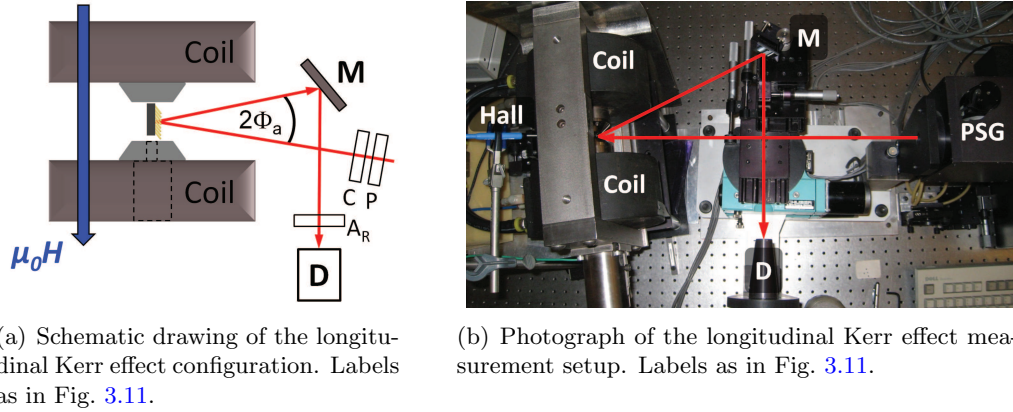


**Figure 3.12:** Same as Fig. 3.11 but in the longitudinal Kerr effect configuration. Light is reflected off the sample at an angle of incidence  $\Phi_a = 18.5^\circ$ .

AB) mounted onto the ellipsometer goniometer. The vector-magnet is illustrated in Fig. 3.13(a) and is composed of four solenoid pairs arranged along the space diagonals of a cube within the magnet frame. The current through each coil pair can be independently controlled with four bipolar power supplies (Kepco, Inc.) such that arbitrary magnetic field directions with a magnitude of maximum 0.4 T are possible; i.e., the magnetic field can be arbitrarily rotated by adjusting the current flow. Magnetic field calibrations are done prior to the optical measurement with a three axis Hall probe (LakeShore Cryotronics, Inc.). The cubic center between the solenoid pole faces can accommodate samples with a maximum size of  $10 \times 10 \text{ mm}^2$ . The sample holder and magnet are mounted with sufficient degrees of freedom for the alignment of the sample with respect to the ellipsometer coordinate system. Within the probing area of the ellipsometry measurement (center of the cube, vertical beam extension of approximately 3 mm) the magnetic field is assumed to be homogeneous. The angle of incidence can be varied within the range  $20^\circ < \Phi_a < 90^\circ$ , where ranges  $\Phi_a = 22^\circ \dots 38^\circ$  and  $\Phi_a = 52^\circ \dots 68^\circ$  are not accessible because the beam is blocked by vertical rods separating top and bottom parts of the magnet assembly (not drawn in Fig. 3.13(a))<sup>107</sup>.

Definitions of measurement configurations in the VMOGE setup are graphically illustrated in Fig. 3.13(b). The plane of incidence ( $\{x, z\}$ -plane) is defined by the incident ( $\mathbf{k}$ ) and reflected ( $\mathbf{k}'$ ) wavevectors. The sample surface is in the  $\{x, y\}$ -plane and the angle of incidence is  $\Phi_a$ . The magnetic field  $\mu_0 \mathbf{H} = \mu_0(H_x, H_y, H_z)$  is parameterized in spherical coordinates, where  $H$  is the magnitude, and the orientation is given by  $\phi_m$  and  $\theta_m$ . Depending on the direction of  $\mathbf{H}$ , polar, longitudinal, and transversal VMOGE configurations are labeled (P), (L), and (T), respectively, and which correspond to the



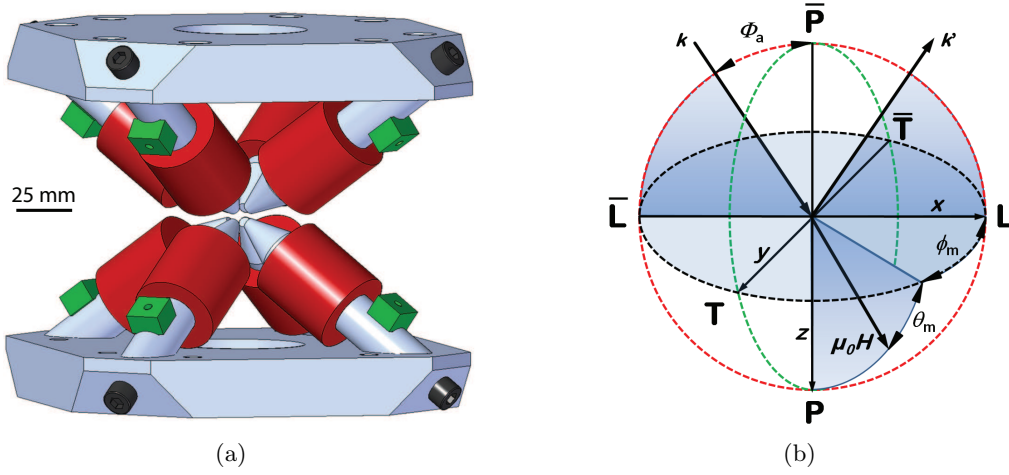


**Figure 3.13:** (a) Technical drawing of the octupole vector-magnet with four solenoid pairs oriented along the space diagonal of a cube and (b) definition of vector-magneto-optical generalized ellipsometry in the Cartesian coordinate system  $\{x, y, z\}$ .  $\mathbf{k}$  and  $\mathbf{k}'$  denote the incident and emergent wavevectors, respectively, with an angle of incidence  $\Phi_a$ . The direction of the external magnetic field  $\mu_0 \mathbf{H}$  is denoted by the azimuthal  $\phi_m$  and polar angle  $\theta_m$ . (P,  $\bar{P}$ ), (L,  $\bar{L}$ ), and (T,  $\bar{T}$ ) indicate polar, longitudinal, and transversal orientations with respect to primary Kerr geometries. The overbar denotes the respective configuration along  $-x, -y, -z$ .

three primary Kerr geometries. In the T-VMOGE configuration  $\mathbf{H}$  is parallel to the  $\{x, y\}$ - and perpendicular to  $\{x, z\}$ -plane ( $H_x \neq 0, H_y = H_z = 0$ ). P- and L-VMOGE are defined accordingly (see also Sect. 3.3.5.1). Additionally, three major orbital scans are defined according to the principal coordinate planes: LP- ( $\phi_m = 0^\circ, \theta_m = 0 \dots 360^\circ$ ), LT- ( $\phi_m = 0 \dots 360^\circ, \theta_m = 0^\circ$ ), and TP-VMOGE ( $\phi_m = 90^\circ, \theta_m = 0 \dots 360^\circ$ ) can be performed by rotating  $\mathbf{H}$  at  $H = \text{const.}$  within the  $\{x, z\}$ -,  $\{x, y\}$ -, and  $\{y, z\}$ -plane, respectively.

# Chapter 4

## Experimental Parameters

### 4.1 Sculptured Thin Film Deposition

STFs discussed in this thesis were deposited at room-temperature in the customized UHV chamber (Sect. 2.2.2) onto (001) Si substrates with a native oxide of approximately 2.5 nm. All deposition materials were purchased in form of pellets (1/4" diameter  $\times$  1/4" length) from the Kurt J. Lesker Company\*. Alumina ( $\text{Al}_2\text{O}_3$ ) crucible liners were used for the deposition of Co, whereas graphite liners were used for Ti and supermalloy. For all STFs discussed here, the deposition angle  $\theta_i$  was set to  $85 \pm 1^\circ$ . The deposition rate was monitored with a quartz crystal microbalance. The electron-beam power was controlled manually by adjusting the emission current to maintain a constant rate typically between 4 and 5  $\text{\AA}/\text{s}$  (with respect to the deposition controller at normal incidence  $\theta_i = 0^\circ$ ). This rate results in a growth time of approximately 10 to 12 min for a 100 nm thick STF deposited at  $\theta_i = 85^\circ$ . The base pressure was approximately  $10^{-9}$  mbar and did not rise above  $10^{-8}$  mbar during depositions.

Table 4.1 summarizes deposition parameters of all samples, for which optical analysis is discussed in the following chapters. A growth recipe is given with respect to substrate action. For example, sample #4 is a Ti 2F2-STF where the first layer was grown for  $p_{t1} = 5$  min, then the substrate was rotated  $180^\circ$  counterclockwise in 15 s ( $r_t(-\pi) = 15$ ), and afterwards kept still for  $p_{t2} = 5$  min to grow the second layer. During growth of samples #8 and #9, the substrate was continuously rotated at 0.1 rpm (counterclockwise for the  $1\text{H}^+$  and clockwise for the  $1\text{H}^-$ ) for 11 min, which results in a total substrate rotation of  $396^\circ$ . The additional 10% have been added to compensate for the formation of the nucleation layer during the initial growth period, based on investigations on previous H-STFs.

---

\*Cobalt has a specified purity of 99.95% and titanium 99.995%. Supermalloy is composed of 79.8% Ni, 15.1% Fe, and 5.1% Mo.

**Table 4.1:** Overview of STF samples and their material discussed in this thesis with sample identification number (ID). A detailed growth recipe is given for each sample with coded substrate dynamics:  $r_t(\pm x)$  denotes a stepwise substrate rotation by  $x$  rad,  $c_t(\pm y)$  denotes a continuous rotation at  $y$  rpm, and  $p_t$  stands for pause time. Values for  $p_t$  and  $c_t$  are given in minutes whereas  $r_t$  is given in seconds.

ID	Material	Geometry	Deposition Rate ( $\text{\AA}/\text{s}$ )	Growth Recipe $[p_t, c_t] = \text{min}, [r_t] = \text{s}$
1	Co	F1	$5.0 \pm 0.3$	$p_t = 10$
2	Ti	F1	$4.0 \pm 0.1$	$p_t = 10:30$
3	NiFeMo	F1	$3.6 \pm 0.2$	$p_t = 11$
4	Ti	2F2	$5.1 \pm 0.1$	$p_{t1} = 5; r_t(-\pi) = 15, p_{t2} = 5$
5	Ti	2F4 <sup>+</sup>	$5.0 \pm 0.2$	$p_{t1} = 5; r_t(-\frac{\pi}{2}) = 10; p_{t2} = 5$
6	Ti	2F4 <sup>-</sup>	$5.0 \pm 0.1$	$p_{t1} = 5; r_t(+\frac{\pi}{2}) = 10; p_{t2} = 5$
7	Co	3F4 <sup>+</sup>	$4.2 \pm 0.3$	$p_{t1} = 16; r_{t1}(-\frac{\pi}{2}) = 10; p_{t2} = 16;$ $r_{t2}(-\frac{\pi}{2}) = 10; p_{t3} = 16$
8	Co	1H <sup>+</sup>	$4.0 \pm 0.1$	$c_t(-0.1) = 11$
9	Co	1H <sup>-</sup>	$4.0 \pm 0.2$	$c_t(+0.1) = 11$

## 4.2 Hybridization

The Ti 2F2-STF (sample #4) was hybridized by infiltrating semiconducting poly(3-dodecylthiophene) (P3DDT), a commonly used hole-conducting polymer<sup>108</sup> to alter optical properties. The STF was hybridized by spin casting the semiconducting polymer P3DDT dissolved in toluene (5 g/L) at 3000 rpm for 45 s. The sample was exposed to ambient air at room-temperature for 12 h to allow the highly volatile solvent to evaporate. P3DDT (synthesized at Neste Oy, Inc.) was used as preserved; the number- and weight-average molecular weight were approximately 10 and 30 kg/mol, respectively.

## 4.3 Generalized Ellipsometry

Unless otherwise noted, all STF samples discussed in this thesis were transferred immediately after deposition to the M2000VI ellipsometer (Sect. 3.2.8) to conduct angle-resolved spectroscopic Mueller matrix ellipsometry measurements within the spectral range from 400 to 1700 nm. The angle of incidence was varied from  $45^\circ \leq \Phi_a \leq 75^\circ$  in steps of  $10^\circ$  while a full sample in-plane rotation  $\phi = 0^\circ \dots 360^\circ$  in steps of  $6^\circ$  was

performed at each angle of incidence.

All GE measurements have been carried out in such a way that the sample orientation at  $\phi = 0^\circ$  corresponds to the initial sample orientation during deposition  $\phi_{\text{GLAD}} = 0^\circ$ . Hence,  $\phi = \phi_{\text{GLAD}} = 0^\circ$  for F1-STFs represents the situation when the slanting plane of the columns is parallel to the plane of incidence and the tips of the columns are pointing toward the source. This situation corresponds to an Euler angle  $\varphi = 90^\circ$  and further clockwise sample rotation  $\phi + \delta\phi$  results in a positive increase of  $\varphi + \delta\varphi$ . Note the difference between the sample orientation while performing ellipsometry measurements  $\phi$  and the Euler angle  $\varphi$ .

Magneto-optical generalized ellipsometry measurements are discussed in their respective section of Chap. 7.

# Chapter 5

## Structural Properties of Metal Sculptured Thin Films

### 5.1 Scanning Electron Microscopy Micrograph Analysis

#### 5.1.1 Flat Substrates

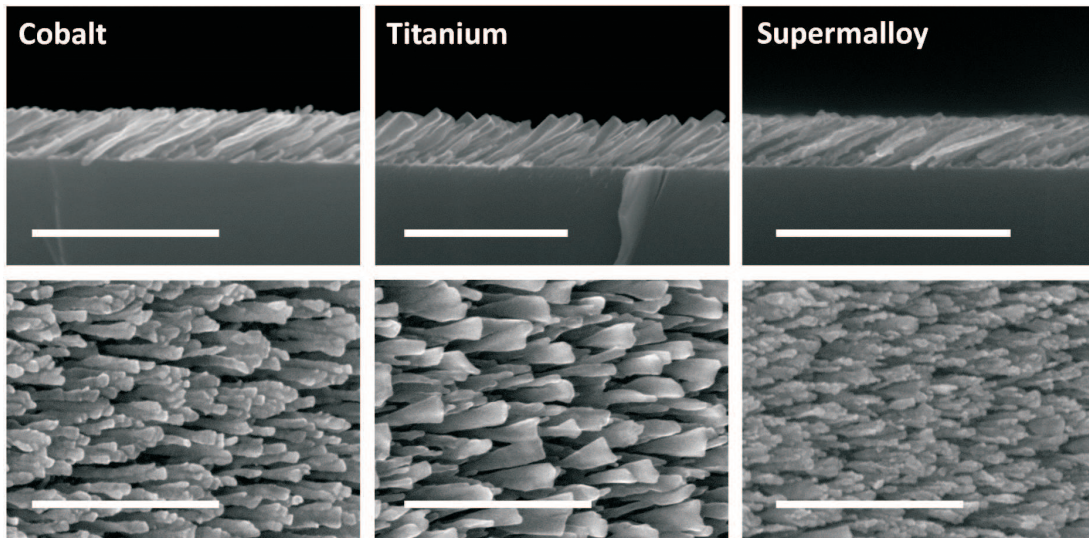
Examples for metal F1-STFs resulting from the deposition procedure on flat substrates discussed in Sect. 4.1 are presented in Fig. 5.1. Cross-sectional and top-view high resolution SEM images of Co (sample #1), Ti (sample #2), and supermalloy (sample #3) F1-STFs illustrate the different film morphologies.

The Co columnar structure grows relatively uniform and bunching of several columns can be observed in the top-view image. Analysis of both Co images shows that the columns have a slightly elliptical shape with the short side of the ellipse ( $18 \pm 2$  nm) in the direction of the incoming vapor flux and the long side ( $24 \pm 3$  nm) perpendicular to it.

Ti columns start to broaden with increasing height because of the anisotropic nature of the physical shadowing. Due to the non-existence of physical shadowing in the direction perpendicular to the incoming particle stream, columns start to fan out<sup>47,109</sup>. Noticeable are the very smooth sidewalls of the columns and the sharp  $90^\circ$  corners at the top of the column. The short axis of the ellipse is approximately  $26 \pm 4$  nm, whereas the long axis varies strongly due to fanning.

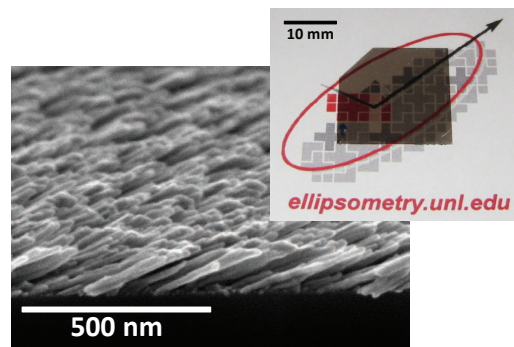
Supermalloy columns are very uniform from bottom to top and hence similar to Co rather than to Ti F1-STFs, however, they exhibit the smallest structure size of the three investigated materials, and a relatively rough column surface. The shape of an individual column is almost round with  $13 \pm 3$  nm and  $14 \pm 3$  nm length for directions parallel and perpendicular to the particle flux, respectively.

Figure 5.2 shows a side view of a Co F1-STFs on top of a Si substrate tilted by



**Figure 5.1:** SEM micrographs of F1-STF from different materials. The panels show cross-sectional and top-view images of cobalt, titanium, and supermalloy, respectively. For all of the images the incoming particle flux direction is from the right. Scale bars are 500 nm.

15° and a photograph of a 100 nm thick F1-STF deposited under similar conditions as sample #1 onto a glass slide. The stack was then placed on a printed image and details of the image can still be seen, which illustrates the high degree of transparency of ferromagnetic Co F1-STFs.



**Figure 5.2:** Scanning electron micrograph of a cobalt F1-STF taken at a sample tilt of approximately 15° and photograph of an almost identical film deposited on a glass slide. The approximately 100 nm thick Co F1-STF is highly transparent as can be seen in the photograph, where the glass slide with deposited F1-STFs is placed onto a printed image.

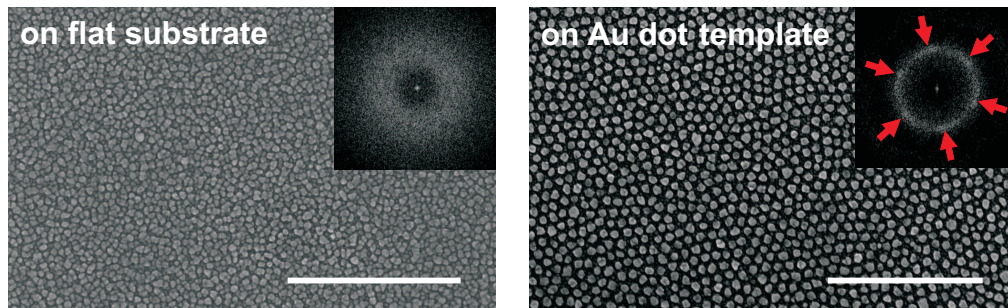


**Figure 5.3:** Top-view SEM micrographs of approximately 50 nm tall Co V-STFs deposited on an untreated flat substrate (left) and on a prepatterned substrate with a hexagonal Au dot-pattern template achieved with diblock-copolymer nanolithography. The inset in each micrograph shows the corresponding Fourier transform spectrum. Scale bars are 1  $\mu\text{m}$ .

### 5.1.2 Prepatterned Substrates

Organized in-plane growth of otherwise randomly distributed nanostructures can be achieved by performing GLAD on a prepatterned substrate. Self-assembled nanodot-pattern within hexagonal arrangement made by diblock-copolymer nanolithography served as nucleation seeds to predetermine structure positions<sup>49,50,54</sup>. Figure 5.3 depicts top-view SEM micrographs of a Co V-STF with a height of approximately 50 nm deposited on a Si substrate. The left image shows posts grown on a flat (unpatterned) part of the sample, whereas nanostructures depicted in the right image are grown on a seed pattern comprising Au dot with a diameter of 12 nm. The inset in each image depicts the Fourier transform spectrum of the respective SEM micrograph. The broad homogeneous circle in the Fourier transform spectrum of the unpatterned part reveals the random in-plane distribution with a quasi-periodic arrangement. The Fourier transform spectrum of the templated part shows a narrow circle with six intense spots (highlighted by the arrows). The defined and narrow circle denotes periodic structures with only small deviations in the intercolumnar spacing and the six intense spots reveal that the hexagonal ordering of the Au seed pattern is still preserved after GLAD growth.

## 5.2 Column Tilt Evaluation

The incident particle flux for growth of the above presented F1-STFs strikes the surface at an angle of  $\theta_i = 85^\circ$  (measured with respect to the substrate normal). It can be seen in the cross-sectional SEM micrographs that the columns of all three materials are not

parallel to the incident vapor but further erected toward the surface normal (Fig. 5.1). The tangent rule can be used to quantitatively explain and determine the tilting angle of the columns with respect to the substrate normal  $\theta$  based on the flux incidence angle  $\theta_i$ <sup>31</sup>:

$$\tan \theta_i = 2 \tan \theta. \quad (5.1)$$

It was realized, however, that as the deposition angle becomes more oblique  $\theta_i > 65^\circ$  the tangent rule predicts too large tilting angles. Tait *et al.*<sup>110</sup> attempted to correct this deficiency by deriving a ballistic model based on a non-symmetric shadowing effect and which led to the relation

$$\theta = \theta_i - \arcsin\left(\frac{1 - \cos \theta_i}{2}\right). \quad (5.2)$$

For  $\theta_i = 85^\circ$  (5.1) predicts a slanting angle of  $\theta = 80.1^\circ$  whereas (5.2) results in  $\theta = 57.8^\circ$ . Therefore, Tait's rule seems to be a good approximation for the Co films, which exhibit a tilting of  $\theta_{\text{Co}} = 57 \pm 3^\circ$ . However, F1-STFs from Ti ( $\theta_{\text{Ti}} = 53 \pm 4^\circ$ ) and NiFeMo ( $\theta_{\text{NiFeMo}} = 64 \pm 4^\circ$ ) show different slanting angles indicating that the result of (5.2) is only an estimate and the slanting angle depends not only geometrically on the incident angle of the vapor flux<sup>111</sup>. Other models incorporating surface diffusion have been reported, however, they only explain trends seen in experiments but also fail to exactly predict the slanting angle<sup>112,113</sup>. During the course of this work, it has been realized that the tilting angle depends also on the geometry of the evaporation source and varies slightly with the deposition rate.

### 5.3 Determination of Structural Parameters by Ellipsometry Data Analysis

Structural parameter analysis using an SEM often involves destructive sample cleaving especially when investigating column tilt and film thickness because cross-sectional SEM images need to be taken. Furthermore, for accurate column tilt determination of both layers of a 2F4<sup>±</sup>-STF, for example, two SEM images should be recorded at sample orientations where the slanting plane coincides with the image plane. Therefore, care needs to be taken before growth that slanting planes are aligned with cleaves, which depends on substrate material and crystal orientation.

All issues related to sample cut or cleaving can be overcome when determining structural parameters such as slanting plane orientation, column tilt, and film thickness by a



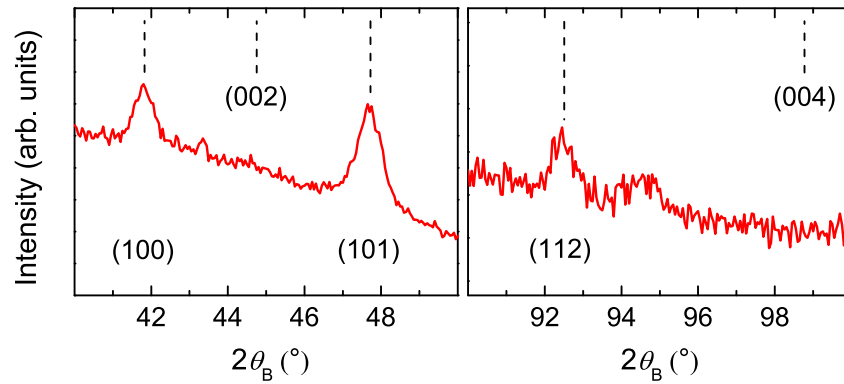


**Figure 5.4:** XRD spectra of a Co F1-STF. All indicated diffraction peak positions belong to a Co hcp lattice.

non-destructive ellipsometry data analysis. As will be shown for different STF samples in Chap. 6, Euler angles  $\theta$  and  $\varphi$ , determining the orientation of major polarizability axes, are identical to the geometrical slanting angle and the rotation of the slanting plane with respect to the laboratory coordinate frame, respectively. Furthermore, the thickness  $d$  is a direct result of the best-match model calculations. These parameters can be individually determined for each layer within complex layered STFs and are in very good agreement with SEM image analysis.

## 5.4 X-ray Diffraction Analysis

X-ray diffraction measurements of a Co F1-STF suggest that the slanted columns have a textured, hexagonal close-packed (hcp) structure with a preferential orientation of the  $\mathbf{c}$ -axis parallel to the wires, which is in agreement with other reports of posts and nanocolumns made by GLAD<sup>45,114</sup> and electrodeposition<sup>115,116</sup>, respectively. Figure 5.4 reveals (100) diffraction peaks in the nanostructured films, which may originate from the nucleation layer whereas the other diffraction peaks, also belonging to a Co hcp lattice, may be due to misaligned domains or even nanocolumns tilted slightly more or less than the average slanting angle of approximately  $57^\circ$  for the particular sample under investigation (determined by SEM and GE analysis). Tilting the crystallographic  $\mathbf{c}$ -axis only  $+1^\circ$  and  $-6^\circ$  away from  $57^\circ$  exposes the (101) and (112) planes, respectively, considering a non-distorted Co hcp lattice. Diffraction peaks from lattice planes (002) and (004) occurring within the depicted  $2\theta$  range are not detected revealing that no

domains are present where the **c**-axis is parallel to the substrate normal. Other  $2\theta_B$  regions where Co hcp diffraction peaks are expected have also been measured but no diffraction peaks were detected.

## 5.5 Summary

- SEM micrograph analysis reveals the elliptical shape of individual nanostructures due to anisotropic shadowing effects. F1-STFs from titanium start to fan out with increasing thin film thickness whereas F1-STFs from cobalt and supermalloy exhibit a relatively uniform column shape.
- Lateral coherence (i.e., organized in-plane growth) can be achieved by depositing on a prepatterned substrate. A nanodot seed template may serve as nucleation centers thereby determining growth positions.
- Tait's rule<sup>110</sup> for predicting the column tilt, which is not parallel to the incoming particle flux, is a simple and good approximation scheme for very oblique deposition conditions ( $\theta_i > 65^\circ$ ).
- X-ray diffraction measurements of Co F1-STFs suggest a textured hcp structure with preferential orientation along the **c**-axis.

## Chapter 6

# Optical Properties of Metal Sculptured Thin Films

This chapter is devoted to the determination of intrinsic optical properties of metal STFs deposited on flat Si substrates. Monoclinic optical properties of slanted columnar thin films (F1-STFs) are determined by the analysis of spectroscopic generalized ellipsometry measurements with a homogeneous biaxial layer approach. A universality regarding the monoclinic and intrinsic major polarizability functions is found in F1-STFs. Complex layered STFs can be considered as cascaded F1-STFs with different slanting directions. Therefore, optical properties of manifold STFs can be predicted by using the optical model developed here for the F1-STFs. The optical model for complex STFs comprises appropriately stacked model layers accounting for F1-STFs in a modular conception thereby mimicking the cascaded STF geometry. It is shown that the piecewise homogeneous biaxial layer approach is also valid for hollow-core helical STFs.

All samples discussed here were analyzed using the multi-sample-configuration analysis method including multiple in-plane orientations  $\phi$  into the best-match model calculations.

### 6.1 Monoclinicity of Metal F1-STFs

Analysis of spectroscopic GE measurements have revealed that metal F1-STFs exhibit monoclinic optical properties. A model based on the specific thin film geometry is proposed, which explains this monoclinic behavior based on dielectric polarization charge coupling effects across neighboring slanted but electrically isolated nanocolumns. A detailed explanation is presented on the example of an achiral Co F1-STF (sample #1).

### 6.1.1 Optical Constants

Experimentally obtained Mueller matrix spectra (as described in Sect. 4.3) for the Co F1-STF were analyzed with an optical model containing a single anisotropic (biaxial) layer on top of the substrate as discussed in Sect. 3.2.6. Consequently, the computed wavelength-independent Euler angles  $(\varphi, \theta, \psi)$  that transform the Cartesian coordinate system  $(x, y, z)$  into the sample coordinates  $(a, b, c)$  represent the orientation of the nanostructure and the internal angles  $\alpha, \beta, \gamma$  differentiate between orthorhombic, monoclinic, or triclinic properties of the film.

The linear polarizability response of F1-STFs due to an electric field  $\mathbf{E}$  is a superposition of contributions along certain directions and may be written as  $\mathbf{P} = \varrho_a \mathbf{a} + \varrho_b \mathbf{b} + \varrho_c \mathbf{c}$ . Axis  $\mathbf{a}, \mathbf{b}, \mathbf{c}$  and major polarizability functions  $\varrho_a, \varrho_b, \varrho_c$  in F1-STFs are determined by nanostructure geometry rather than crystallographic unit cells. The experiment shows, that for F1-STFs,  $\mathbf{a}, \mathbf{b}$ , and  $\mathbf{c}$  span a monoclinic coordinate system with  $\mathbf{c}$  along the long axis of the columns,  $\mathbf{a}$  perpendicular to  $\mathbf{b}$  and  $\mathbf{c}$  and parallel to the substrate surface, and a monoclinic angle  $\beta$  between  $\mathbf{c}$  and  $\mathbf{b}$ . Along these axes, major polarizability functions  $1 + \varrho_j = \varepsilon_j$  ( $j = a, b, c$ ) can be determined which may vary with frequency (see also Sect. 3.2.4).  $\varrho_j$  were first determined on a wavelength-by-wavelength basis. The point-by-point extracted data have then been parameterized with MDFs (Lorentzian oscillators and Drude terms) and the best-match model calculation procedure was repeated facilitating the MDF approach for final results.

For the Co F1-STF, functions  $\varrho_a$  and  $\varrho_b$  were parameterized with three Lorentz oscillators, respectively, and four Lorentz oscillators and one Drude term were incorporated for  $\varrho_c$ . Individual parameters are listed in Table 6.4. Note that the MDF parameters are very specific for Co F1-STFs grown in the deposition chamber discussed in Sect. 2.2.2. However, it should be pointed out that retrieved optical constants are highly reproducible for films deposited in an identical manner. F1 nanostructures grown in a UHV chamber with different geometries, for example, will exhibit slightly altered values due to different packaging fractions and possibly shape of the columns itself.

The MDF parameters are presented exemplarily only without further evaluation. The identification of physically meaningful quantities is not within the scope of this thesis. Hence, for other STF discussed below MDF parameters are not listed individually.

Note that principal refractive indices and extinction coefficients along major polarizability axes ( $\mathbf{a}, \mathbf{b}, \mathbf{c}$ ) do not exist for monoclinic (and triclinic) materials, instead intrinsic polarizability functions ( $\varrho_a, \varrho_b, \varrho_c$ ) need to be discussed. Intrinsic complex-valued optical constants ( $N_a, N_b, N_c$ ) imply that directions exist, along which wave propaga-

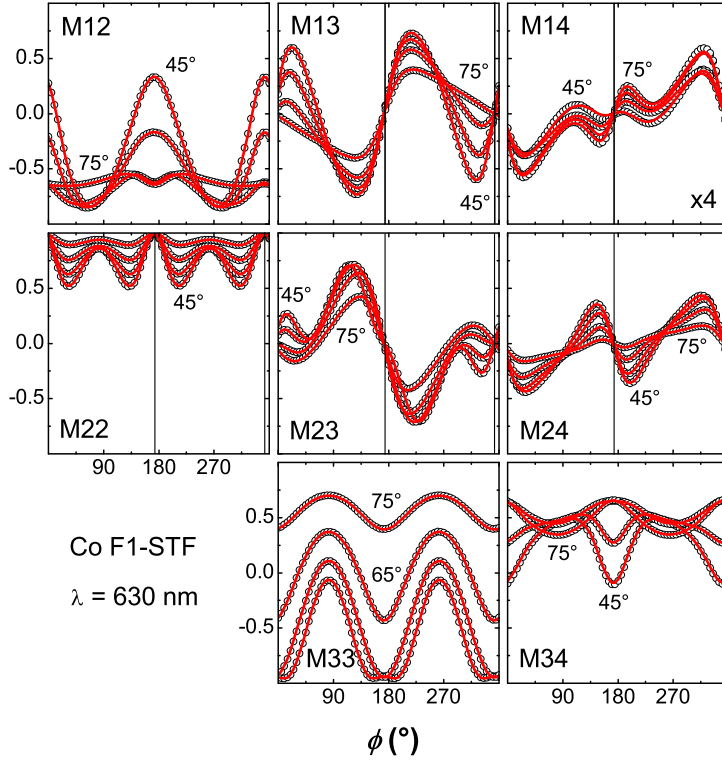


**Figure 6.1:** Exemplary experimental (circles) and best-match calculated (solid lines) GE data of a Co F1-STF versus sample azimuth angle  $\phi$  at  $\lambda = 630$  nm. The four graphs for each Mueller matrix element are four different angles of incidence  $\Phi_a = 45^\circ, 55^\circ, 65^\circ, 75^\circ$ . Note the pseudo-isotropic orientations (indicated by the vertical bars); i.e., the sample positions  $\phi$  at which all off-diagonal Mueller matrix data ( $M_{13}, M_{14}, M_{23}, M_{24}$ ) vanish and  $M_{22} = 1$ , which is the case near  $\phi = 0^\circ$  and  $\phi = 180^\circ$ . Such orientations occur when the slanting plane coincides with the plane of incidence. Element  $M_{14}$  is magnified  $\times 4$ .

tion with such indices can be obtained (and measured upon refraction). However, such directions do not exist in materials with monoclinic and triclinic symmetry and therefore,  $N_a, N_b, N_c$  do not exist. Alternatively, since presentation of optical functions in terms of  $\varrho_a, \varrho_b, \varrho_c$  are not yet common, in this thesis,  $N_j \equiv \sqrt{1 + \varrho_j} = n_j + ik_j$  with  $j = a, b, c$ , are seen as effective optical constants.

**Experimental data.** Figure 6.1 depicts selected GE Mueller matrix data for four different angles of incidence obtained from a ferromagnetic Co F1-STF (sample #1) at an exemplary wavelength of  $\lambda = 630$  nm\*. The film was measured approximately

\*A wavelength of  $\lambda = 630$  nm was chosen for depicting Mueller matrix data with respect to sample azimuth because it is fairly close to the wavelength of a HeNe ( $\lambda = 632.8$  nm), which is typically

1 h after deposition, therefore it is assumed that data are representative for pure Co nanostructures and a possible oxide shell can be neglected at this point. The graphs show non-redundant\* Mueller matrix elements of the measured  $4 \times 3$  part of the matrix versus sample azimuth. Model and experimental data are in excellent agreement for all wavelengths in the investigated spectral region from 400 to 1700 nm. The off-diagonal Mueller matrix data ( $M_{13}$ ,  $M_{14}$ ,  $M_{23}$ ,  $M_{24}$ ) exhibit the highly anisotropic nature of the F1 nanostructures. These elements are zero for all angles of incidences  $\Phi_a$  at all wavelengths for isotropic samples. So-called pseudo-isotropic sample orientations can be identified at  $\phi \approx 0^\circ$  and  $\phi \approx 180^\circ$ , which coincide with orientations of the sample when the slanting direction of the nanocolumns is parallel to the plane of incidence (Euler angles  $\varphi = 90^\circ$  and  $\varphi = 270^\circ$ ). Hence, no  $p$ -polarized light is converted into  $s$ -polarized light and vice versa in this particular setup. It can be seen that there is no repetition of data over one full rotation except for symmetry with respect to pseudo-isotropic  $\phi$  positions, and data over one full in-plane rotation should be measured in order to fully evaluate the optical properties. The element with the smallest amplitude is  $M_{14}$  (multiplied by a factor of 4), which carries information on circularly polarized light. Interestingly,  $M_{22}$  exhibits a four-fold symmetry, whereas  $M_{33}$  only shows a two-fold symmetry with respect to sample in-plane orientation.

Functions  $N_a, N_b, N_c$  obtained with parameterized MDFs (Table 6.4) are depicted in Fig. 6.2. Refractive indices  $n_j$  and absorption coefficients  $k_j$  are pertinent to axes **a**, **b**, and **c** of the coordinate system shown in Fig. 6.3 and differ drastically from those of bulk material (right panel)<sup>†</sup>. Note that the reported optical constants are effective values since the optical model assumes a homogeneous layer. Strong birefringence and dichroism can be observed in the investigated spectral region between all polarizabilities. The index of refraction  $n_c$  along the slanted nanocolumns (**c**-axis) is intersecting with both other refractive indices  $n_b$  and  $n_a$  (Fig. 6.2). Such intersections are not present for the extinction coefficients  $k_j$  which follow the same order as the refractive indices above  $\lambda = 800$  nm ( $k_c > k_a > k_b$ ). In general,  $n_c$  and  $k_c$  have a strong wavelength dependence in contrast to the optical constants along the **a**- and **b**-axes. There is almost no absorption along axis **b**. Amongst the three directions, the polarizability along the **c**-axis of the nanostructures is the only one with a similar dispersion compared to bulk Co.

---

available in laboratories dealing with optics.

\*In case the sample under investigation does not exhibit non-reciprocal properties, Mueller matrix elements not shown can be obtained by symmetry operations:  $M_{21}(\varphi) = M_{12}(\varphi + \pi)$  and  $M_{3j}(\varphi) = -M_{j3}(\varphi + \pi)$  with  $j = 1, 2$ . No inversion operation is necessary to convert  $M_{12}(\varphi)$  into  $M_{21}(\varphi + \pi)$  because these elements depend on the symmetric cos function only whereas this is not true for all other elements. See for example (3.11).  $\pi$  denotes a sample rotation by  $180^\circ$ .

<sup>†</sup>Optical constants for bulk Co have been taken from Palik<sup>117</sup>.

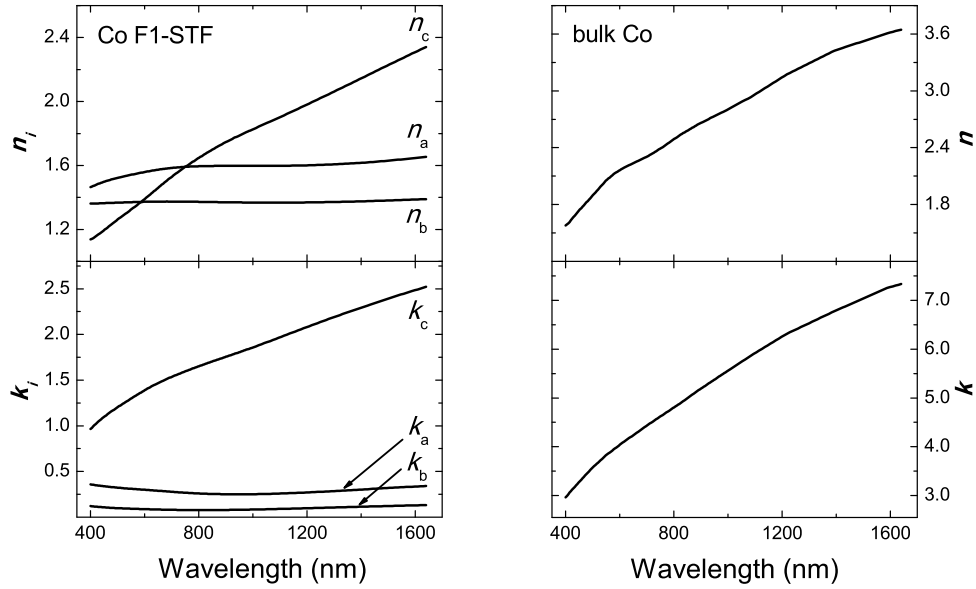


**Figure 6.2:** Refractive indices  $n_j$  and extinction coefficients  $k_j$  along major polarizability axes **a**, **b**, **c** with monoclinic arrangement of a Co F1-STF, and isotropic bulk optical constants of Co. From the anisotropic optical constants of the F1-STF only those along axis **c** have similarities with the isotropic bulk optical constants.

The optically determined structural parameters film thickness ( $d = 106.9 \pm 0.1$  nm) and inclination angle (Euler angle  $\theta = 63.68 \pm 0.01^\circ$ ) are in very good agreement with data from SEM micrograph analysis ( $d = 115 \pm 5$  nm and  $\theta = 65 \pm 3^\circ$ , respectively). Note that the GE thickness parameter is an optical thickness, which is generally less than SEM estimates. Even though thickness estimates from cross-sectional SEM images are typically from a different region of the thin film than that measured optically, the optical thickness is assumed to originate mainly from differences between the idealized model and the real STF. In particular, the optical model does not account for a nucleation layer (typically  $< 5$  nm) or a surface roughness, for example. Besides that, in the homogenization approach, the columns are assumed to be homogeneous along the long axis. These idealizations might affect the optically determined thin film thickness (for SEM micrographs of F1-STFs see Fig. 5.1).

The investigated Co F1-STF possesses monoclinic optical properties with an angle  $\beta = 83.69 \pm 0.09^\circ$  ( $\alpha = \beta = 90^\circ$ ). The MSE, which is a measure for the quality of the match between model and experimental data is 7.77. The Euler angle  $\psi = 0$  and hence not included in the best-match model calculations. This can be seen by the pseudo-isotropic orientations in the angle-resolved experimental Mueller matrix data

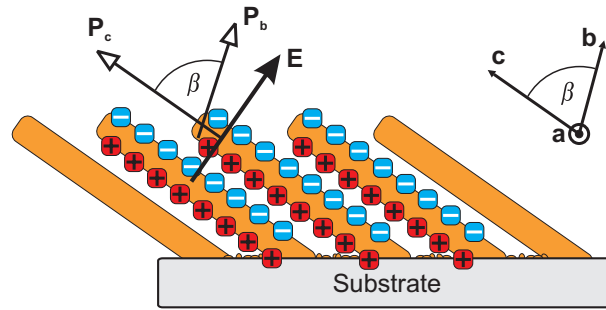


**Figure 6.3:** Schematic drawing of the electric charge transfer mechanism causing monoclinic optical properties. The polarization  $\mathbf{P}_b$  due to an electric field  $\mathbf{E}$  within the plane of incidence is tilted toward the substrate normal.

(Fig. 6.1). Such orientations with no conversion between  $p$ - and  $s$ -polarization states would not occur if the sample coordinate system was further rotated by  $\psi$  ( $\mathbf{b}$  out of the slanting plane, and  $\mathbf{a}$  out of the substrate surface).

### 6.1.2 Monoclinicity

The monoclinic angle reveals an intrinsic optical thin film property of F1-STFs and results also from the specific arrangement of the coherently tilted nanostructures. As discussed in Sect. 3.2.4, monoclinic properties can only be identified by considering a broad spectral range during data analysis.

The monoclinic angle can be understood as a characteristic due to charge transfer leading to anisotropic charge distribution in slanted columnar thin films (F1-STFs) prepared from electrically conductive materials. At the bottom of the structure, charge exchange is possible due to a conducting nucleation (wetting) layer whereas charge transfer is not possible at the isolated top of the column. The slanting of nanocolumns causes an anisotropic distribution of charges due to the mutual screening of charge dipoles across adjacent columns (Fig. 6.3). Therefore, the effective overall dipole moment for electric fields perpendicular to the columns and within the slanting plane ( $\mathbf{P}_b$ ) is tilted toward the surface normal. Further examples of monoclinic F1-STF are discussed in Sect. 6.2. It can be expected that the monoclinic angle depends on the overall film thickness, the tilting angle of the columns, the intercolumnar spacing, and the properties of the nucleation layer. Systematic investigations have yet to be conducted, however, trends observed in currently available samples hint in this direction.



### 6.1.3 Summary

- Highly anisotropic F1-STF with biaxial optical properties exhibit pseudo-isotropic orientations, which coincide with sample orientations when the slanting plane of the columns is parallel to the plane of incidence.
- Large birefringence and dichroism is observed in the visible and near infrared spectral region and effective optical constants differ significantly from those of bulk material.
- F1-STFs exhibit monoclinic optical properties due to anisotropic charge distribution. The wetting layer at the bottom of the columns allows for charge transfer whereas this is hindered at the isolated column tops.

## 6.2 Universality of Metal F1-STFs

Analysis have shown that there are several characteristics common for metal F1-STF investigated here. Angle-resolved Mueller matrix data for F1-STF prepared from different materials exhibit two pseudo-isotropic orientations, which occur when the slanting plane is parallel to the plane of incidence. The consequence is that the Euler angle  $\psi = 0$  and can be excluded from best-match model calculations. For each Mueller matrix element versus  $\phi$ , except element  $M_{34}$ , the graph representing data for  $\Phi_a = 75^\circ$  exhibits less azimuthal variations than  $\Phi_a = 45^\circ$ .

The attained refractive indices and extinction coefficients along major polarizability axis for each material show similar dispersion relations and exhibit strong birefringence and dichroism. The order of the refractive indices in the near-infrared spectral region is always identical with  $n_c > n_a > n_b$ , and which is also the order of the extinction coefficients within the entire investigated spectral region.  $n_c$  and  $k_c$  exhibit bulk-like dispersion, whereas  $k$  along axes **a** and **b** shows almost no absorption.  $n_c$  always intersects  $n_a$  and then  $n_b$  within the visible spectral region. Furthermore, all investigated F1-STFs exhibit monoclinic optical properties.

The observed universality is demonstrated here for two additional F1-STFs made from titanium (sample #2) and supermalloy ( $\text{Ni}_{80}\text{Fe}_{15}\text{Mo}_5$ , sample #3). Experimentally obtained angle-resolved Mueller matrix data for both films have been analyzed in the same manner as explicitly described for Co F1-STFs in Sect. 6.1.1.

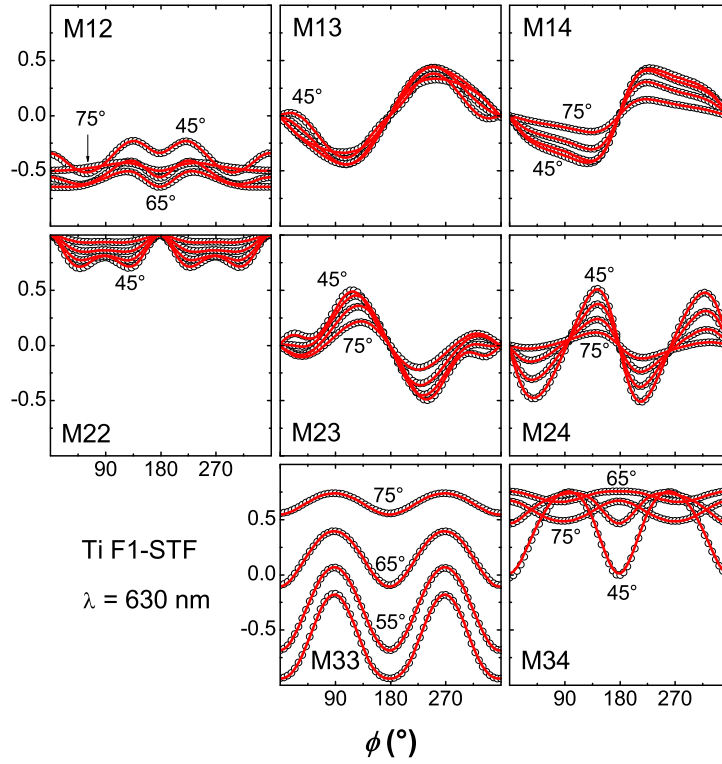


**Figure 6.4:** Exemplary experimental (circles) and best-match calculated (solid lines) GE data of a Ti F1-STF versus sample azimuth angle  $\phi$  at  $\lambda = 630$  nm. The four graphs for each Mueller matrix element are four different angles of incidence  $\Phi_a = 45^\circ, 55^\circ, 65^\circ, 75^\circ$ . Note the pseudo-isotropic orientations; i.e., the sample positions  $\phi$  at which all off-diagonal Mueller matrix data ( $M_{13}, M_{14}, M_{23}, M_{24}$ ) vanish and  $M_{22} = 1$ , which is the case near  $\phi = 0^\circ$  and  $\phi = 180^\circ$ . Such orientations occur when the slanting plane coincides with the plane of incidence.

### 6.2.1 Titanium F1-STFs

The optical model for Ti F1-STFs contains parameterized MDFs for optical constants along the major polarizability axes **a**, **b**, and **c** of a monoclinic system.  $\rho_a$  and  $\rho_b$  contain two and three Lorentzian oscillators, and  $\rho_c$  four Lorentzian oscillators and a Drude term.

Figure 6.4 depicts selected non-redundant Mueller matrix data versus sample azimuth for four different angles of incidence ( $\Phi_a = 45^\circ, 55^\circ, 65^\circ, 75^\circ$ ) at  $\lambda = 630$  nm obtained approximately 1 h after deposition. Note the pseudo-isotropic orientations occurring at  $\phi = 180^\circ$  and  $\phi = 360^\circ$ , which again agree with the orientation where the slanting plane is parallel to the plane of incidence.

The spectral dependence of  $M_{12}$  is exemplarily shown in Fig. 6.5 for an in-plane

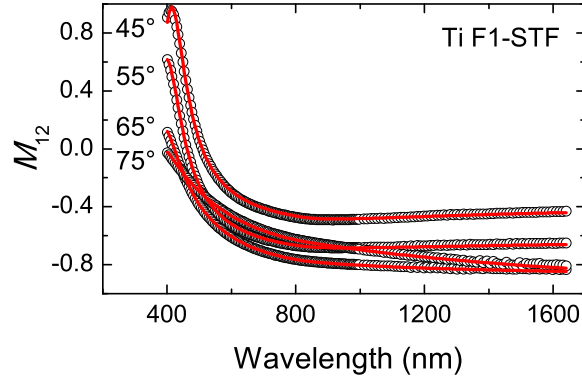


**Figure 6.5:** Exemplary experimental (circles) and best-match calculated (solid lines) GE data of a Ti F1-STF for four different angles of incidence  $\Phi_a$  within the wavelength range from 400 to 1650 nm. The change in spectral resolution occurring around  $\lambda = 1000$  nm is due to the two different CCD arrays used for the short and long wavelength region as discussed in Sect. 3.2.8.

orientation  $\phi = 1.7^\circ$  (close to a pseudo-isotropic orientation because there is no mode-coupling). Data demonstrate the excellent agreement between experiment and best-match model. There is almost no dispersion in the near infrared spectral region until substantial variation occurs in the visible spectral region. The peak position, which is at approximately 400 nm for  $\Phi_a = 45^\circ$  correlates with the thin film thickness and hence is a Fabry-Pérot interference in the STF.

Refractive indices  $n_j$  and absorption coefficients  $k_j$  depicted in Fig. 6.2 differ significantly from those of bulk material (right panel, taken from Palik<sup>117</sup>). In general, the optical constants have similar properties and dispersion relations compared to the ones from ferromagnetic Co F1-STFs (Sect. 6.1.1). Again,  $n_c$  and  $k_c$  exhibit similarities with bulk optical constants from Ti. Especially the local maximum in  $k$  around 800 nm caused by interband transitions is present, although not as pronounced as in the case of bulk Ti<sup>118</sup>.

The investigated Ti F1-STF possesses monoclinic optical properties with an angle  $\beta = 80.2 \pm 0.1^\circ$  ( $\alpha = \gamma = 90^\circ$ ). Other structural parameters determined from optical analysis and in comparison to SEM micrograph analysis are summarized in Sect. 6.5, Table 6.6.

### 6.2.2 Supermalloy ( $\text{Ni}_{80}\text{Fe}_{15}\text{Mo}_5$ ) F1-STFs

The optical model for supermalloy F1-STFs contains parameterized MDFs for major polarizabilities  $\varrho_a, \varrho_b, \varrho_c$ , where two and three Lorentzian oscillators are incorporated

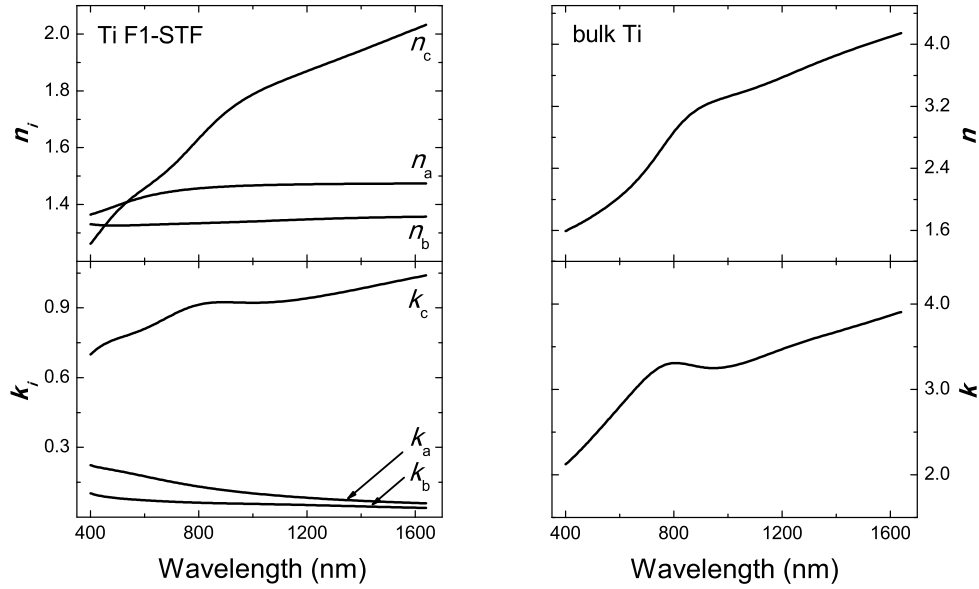


**Figure 6.6:** Refractive indices  $n_j$  and extinction coefficients  $k_j$  along major polarizability axes **a**, **b**, **c** with monoclinic arrangement of a Ti F1-STF, and isotropic bulk optical constants of Ti.

into  $\varrho_a$  and  $\varrho_b$ , respectively;  $\varrho_c$  contains two Lorentzian oscillators and a Drude term.

Non-redundant Mueller matrix data for four different angles of incidence ( $\Phi_a = 45^\circ, 55^\circ, 65^\circ, 75^\circ$ ) obtained at  $\lambda = 630$  nm versus sample azimuth are depicted in Fig. 6.7. The azimuthal variations of the Mueller matrix elements are very close to those from the Co F1-STF except for elements  $M_{22}$  and  $M_{14}$ , which are comparable to Ti F1-STFs.

Refractive indices  $n_j$  and absorption coefficients  $k_j$  depicted in Fig. 6.8 differ significantly from those of bulk material (right panel)\*.  $n_c$  and  $k_c$  exhibit similarities with bulk optical constants, however, the broad shoulder in  $n_c$  between 800 and 1200 nm (Fig. 6.8) is flattened out for the F1-STF. Supermalloy STF optical constants are almost identical to the ones from ferromagnetic Co F1-STFs (Fig. 6.2).

The obtained monoclinic angle  $\beta = 89.52 \pm 0.08^\circ$  indicates almost purely orthorhombic properties. Structural parameters determined optically through best-match model calculations are summarized in Sect. 6.5, Table 6.7.

\*Bulk optical constants have been generated with an isotropic Bruggeman EMA ( $L_{\text{iso}}^{\text{D}} = \frac{1}{3}$  for spherical inclusions) and optical constants for Ni, Fe, and Mo were taken from Palik<sup>117</sup>. For further details on Bruggeman EMA see also Sect. 3.2.6

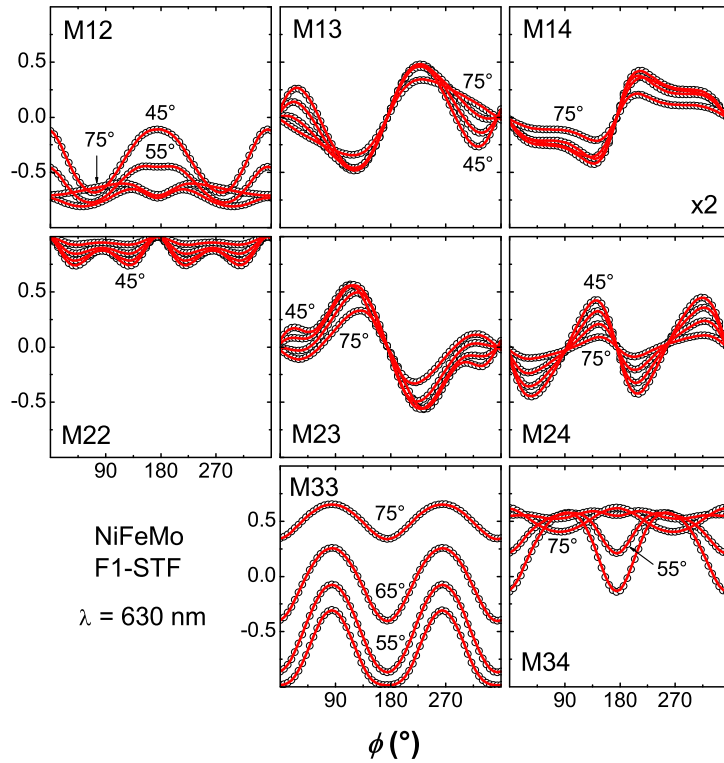


**Figure 6.7:** Exemplary experimental (circles) and best-match calculated (solid lines) GE data of a NiFeMo F1-STF versus sample azimuth angle  $\phi$  at  $\lambda = 630$  nm. The four graphs for each Mueller matrix element are four different angles of incidence  $\Phi_a = 45^\circ, 55^\circ, 65^\circ, 75^\circ$ . Note the pseudo-isotropic orientations; i.e., the sample positions  $\phi$  at which all off-diagonal Mueller matrix data ( $M_{13}, M_{14}, M_{23}, M_{24}$ ) vanish and  $M_{22} = 1$ , which is the case near  $\phi = 0^\circ$  and  $\phi = 180^\circ$ . Such orientations occur when the slanting plane coincides with the plane of incidence. Element  $M_{14}$  is magnified  $\times 2$ .

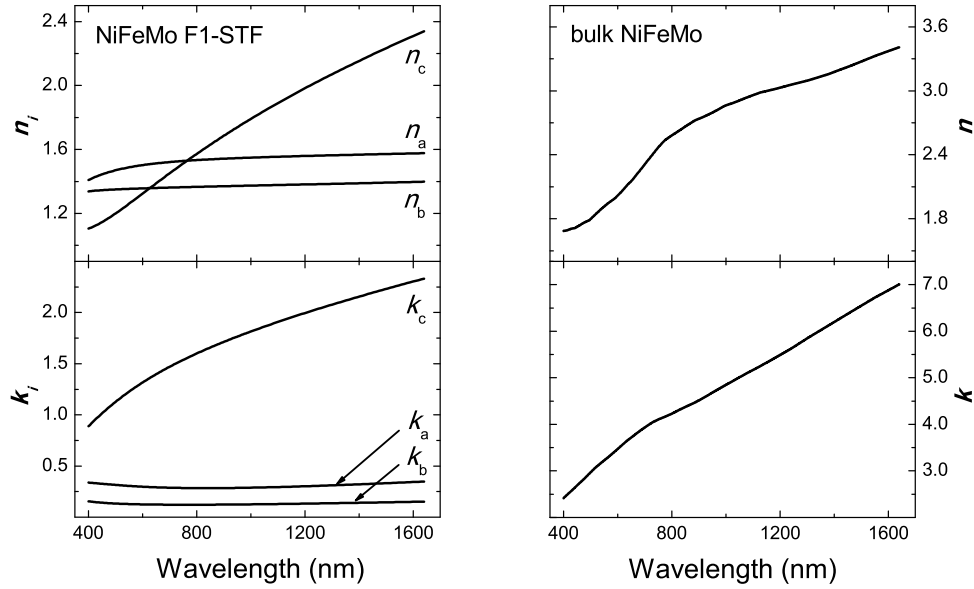


**Figure 6.8:** Refractive indices  $n_j$  and extinction coefficients  $k_j$  along major polarizability axes **a**, **b**, **c** with monoclinic arrangement of a superalloy F1-STF, and isotropic bulk optical constants of  $\text{Ni}_{80}\text{Fe}_{15}\text{Mo}_5$ .

### 6.2.3 Summary

Optical properties of F1-STF from different metals and metal alloys exhibit very similar characteristics:

- The Euler angle  $\psi = 0$  can be excluded from model calculations, which is a consequence of the pseudo-isotropic orientations and due to the fact that all columns share parallel slanting planes.
- Refractive indices in the near infrared spectral region follow the order  $n_c > n_a > n_b$  and hence the same order as the extinction coefficients in the entire investigated spectral region.
- $N_c$  exhibits similarities with bulk optical constants from the respective material of which the STFs are made of and there is almost no absorption along axes **a** and **b**.
- All metal F1-STFs exhibit monoclinic optical properties.

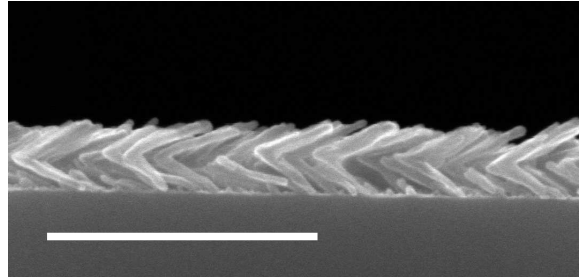


**Figure 6.9:** SEM micrograph of the Ti 2F2-STF. The scale bar is 500 nm.

### 6.3 Modularity of Complex Sculptured Thin Films

Optical constants determined for an F1-STF (for a certain material and deposition setup) can be used in principle to predict the optical response for any STF with an arbitrary sequence of rotation steps during growth (*lFx*-STFs as well as H-STFs). Complex layered STFs can be considered as cascaded F1-STFs with different slanting directions. Therefore, optical properties of manifold STFs can be predicted by using the optical model discussed above for F1-STFs as a basic module. The optical model for complex STFs then comprises appropriately stacked model layers accounting for F1-STFs in a modular conception thereby mimicking the cascaded STF geometry. The modularity is exemplarily discussed for a total of four differently grown complex layered STF from cobalt and titanium. Furthermore, it is shown that this piecewise homogeneous biaxial layer approach is also valid for hollow-core helical STFs.

Information on growth conditions for each sample discussed here can be found in Chap. 4 and Table 4.1.

#### 6.3.1 Chevron-like Sculptured Thin Films (2F2-STFs)

Morphologically one step advanced with respect to F1-STFs are F2-STFs. These nanostructured thin films, also called chevrons or zig-zags, consist of  $m$  layers of slanted columns with alternating tilting direction and may therefore be considered as cascaded F1-STFs (Fig. 6.9). The change in geometry required for this growth can be obtained by rotating the substrate by half a turn around its normal axis. Note that all layers of a chevron nanostructure share a common plane containing the slanted column and the substrate normal and therefore, 2F2-STFs are achiral. Exemplarily, the optical analysis of a 2F2-STF from titanium (sample #4) is discussed here.

In contrast to the previously discussed F1-STFs (Sect. 6.2.1), the optical model

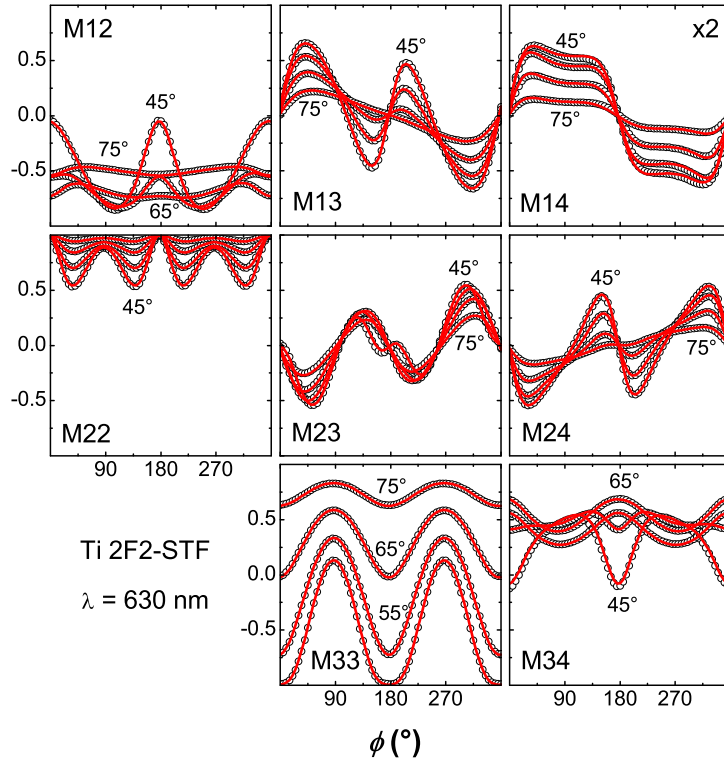


**Figure 6.10:** Exemplary experimental (circles) and best-match calculated (solid lines) GE data of a NiFeMo F1-STF versus sample azimuth angle  $\phi$  at  $\lambda = 630$  nm. The four graphs for each Mueller matrix element are four different angles of incidence  $\Phi_a = 45^\circ, 55^\circ, 65^\circ, 75^\circ$ . Note the pseudo-isotropic orientations; i.e., the sample positions  $\phi$  at which all off-diagonal Mueller matrix data ( $M_{13}$ ,  $M_{14}$ ,  $M_{23}$ ,  $M_{24}$ ) vanish and  $M_{22} = 1$ , which is the case near  $\phi = 0^\circ$  and  $\phi = 180^\circ$ . Such orientations occur when the slanting planes of both layers coincide with the plane of incidence. Element  $M_{14}$  is magnified  $\times 2$ .

for the achiral 2F2-STF is composed of two anisotropic (biaxial) layers with opposite azimuthal orientation ( $\varphi_1 = -\varphi_2$ ), which account for both slanting directions. Hence, the thin film is virtually separated into two F1-STFs for optical analysis (for model details see also Sect. 3.2.6). The single set of major polarizabilities  $\varrho_a, \varrho_b, \varrho_c$  used in both layers has been parameterized with MDFs. Functions  $\varrho_a$  and  $\varrho_b$  contain two and three Lorentz oscillators, respectively, and four Lorentz oscillators and one Drude term were incorporated for  $\varrho_c$ .

Selected experimental and best-match model calculated GE Mueller matrix data for four different angles of incidence obtained from the Ti 2F2-STF are depicted in Fig. 6.10. A single wavelength  $\lambda = 630$  nm was chosen for the graphs and similar results with an excellent agreement between model and experimental data have been



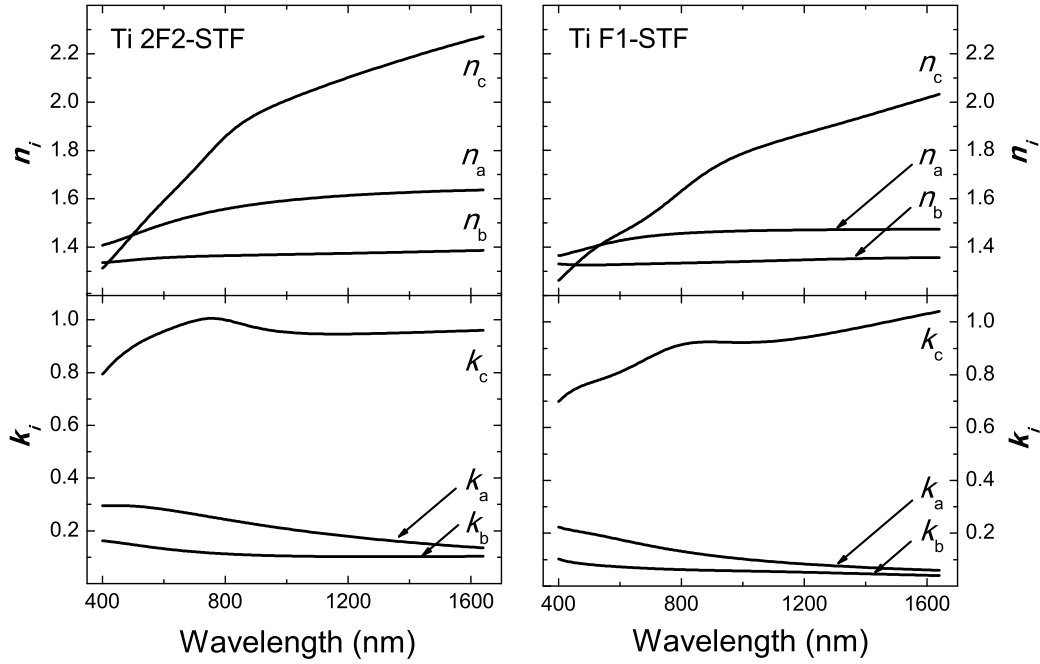


**Figure 6.11:** Refractive indices  $n_j$  and extinction coefficients  $k_j$  along major polarizability axes **a**, **b**, **c** with monoclinic arrangement of a Ti 2F2-STF (left panel) in comparison with Ti F1-STF (right panel).

obtained for all wavelengths in the investigated spectral region from 400 to 1700 nm. Also for 2F2-STFs pseudo-isotropic sample orientations can be identified at  $\phi \approx 0^\circ$  and  $\phi \approx 180^\circ$ , which coincide with sample directions when the set of slanting planes is parallel to the plane of incidence. This reveals that also for a two-layered STF, where both slanting directions share the same plane, similar properties as for F1-STFs can be found.

The obtained set of optical constants common for both biaxial layers is in very good agreement with optical constants determined from Ti F1-STFs deposited in a comparable manner (Fig. 6.11). Even the shoulder in  $n_c$  and  $k_c$  around 800 nm caused by interband transitions<sup>118</sup> can still be observed. Differences between Ti 2F2- and F1-STF optical constants are attributed to structure non-idealities, differently chosen deposition rates, and the assumed ideal interface between bottom and top layers in the optical model.

Other optically determined best-match parameters are summarized in Table 6.5 (Sect. 6.4.1). A deviation from  $180^\circ$  of the angle between the two deposition steps  $\delta\varphi$  is a measure for the non-perfect alignment of the two slanting planes. The mono-

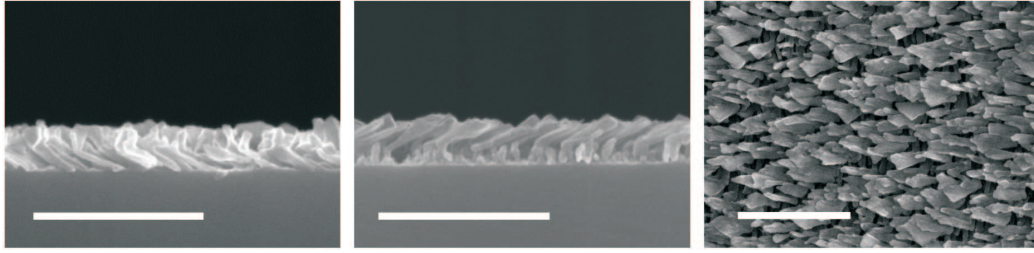


**Figure 6.12:** Cross-section and top-view SEM micrographs of the Ti 2F4<sup>+</sup>-STF. The left and middle images are orientated such that the first and the second layer are in the plane of the image, respectively. The top-view image (right) illustrates the high porosity and reveals that structure fanning (broadening) is comparable to that of a single layer (Fig. 5.1). Scale bars are 500 nm.

clinic system is much further distorted with  $\beta_1 = 58^\circ$  compared to Ti F1-STFs. This could be due to additional charges at the top of the second layer, which enhance the monoclinic effect and further tilt the effective polarization  $\mathbf{P}_b$  toward the substrate normal. The monoclinic angle of the second layer,  $\beta_2$ , approaches  $90^\circ$  because the top F1-STF layer has no lateral conductive channel along which the necessary charge transfer could occur (Fig. 6.3).

### 6.3.2 L-shape Sculptured Thin Films (2F4-STFs)

The most primitive chiral STF is a 2F4-STF, “L-shape” STF, where handedness is introduced based on the rotation direction of the substrate during growth. The required change in geometry for this growth can be obtained by rotating the substrate by  $\pm 90^\circ$  around its normal axis after depositing the first layer. If the second layer is rotated counterclockwise by  $90^\circ$  with respect to the first one, the nanostructured L-shape thin film is termed here 2F4<sup>+</sup>-STF (right-handed; sample #5; Fig. 6.12), otherwise 2F4<sup>-</sup>-STF (left-handed, sample #6). Both, a right- and left-handed 2F4-STFs from titanium are discussed and compared.

Similar to 2F2-STFs (previous section), the optical model for the chiral 2F4-STFs is composed of two anisotropic (biaxial) layers, which are azimuthally rotated with respect to each other by Euler angle  $\pm\delta\varphi$ . Hence, the thin film is virtually separated into two model layer F1-STFs for optical analysis (for model details see Sects. 3.2.6 and 6.1.1).

Here, the single set of major polarizabilities  $\varrho_a, \varrho_b, \varrho_c$  used in both biaxial model layers is similar for the right- and lefthanded chiral STF and has been parameterized with MDFs. Functions  $\varrho_a$  and  $\varrho_b$  contain two Lorentz oscillators each, and four Lorentz

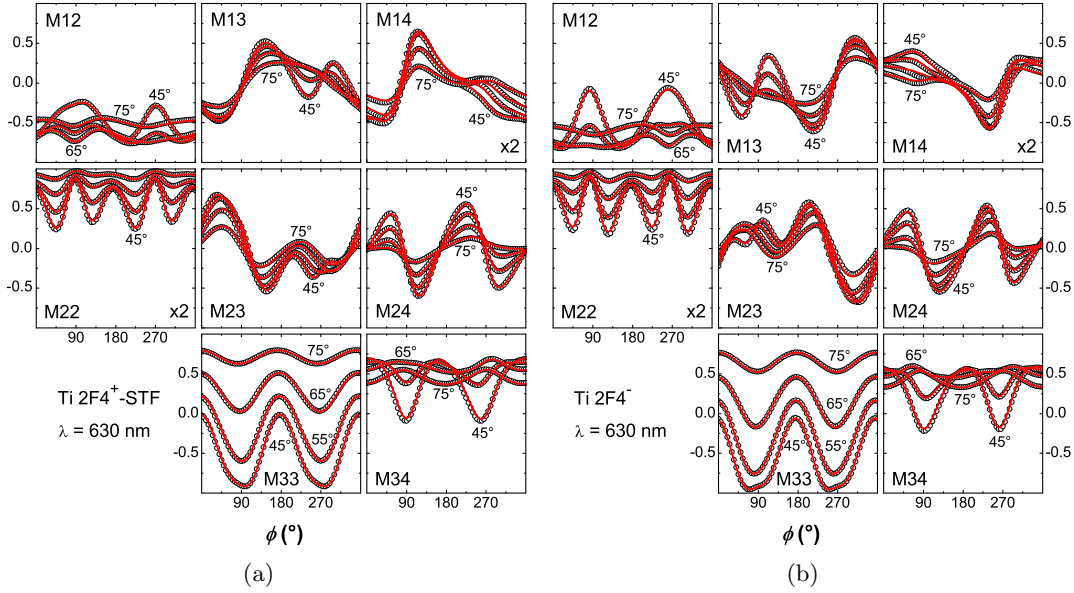


**Figure 6.13:** Exemplary experimental (circles) and best-match calculated (solid lines) GE data of a Ti  $2F4^+$ -STF (a) and a Ti  $2F4^-$ -STF (b) versus sample azimuth angle  $\phi$  at  $\lambda = 630$  nm. The four graphs for each Mueller matrix element are four different angles of incidence  $\Phi_a = 45^\circ, 55^\circ, 65^\circ, 75^\circ$ . Note that for these chiral STF's no pseudo-isotropic orientation is present. Elements  $M_{14}$  and  $M_{22}$  are magnified  $\times 2$ .

oscillators and one Drude term were incorporated for  $\rho_c$ .

Experimental and best-match model calculated GE Mueller matrix data for four different angles of incidence obtained from the Ti  $2F4^+$ -STF and  $2F4^-$ -STF are shown in Fig. 6.13(a) and Fig. 6.13(b), respectively. Each graph depicts eight non-redundant Mueller matrix elements versus sample azimuth at an exemplary wavelength  $\lambda = 630$  nm. For ideal samples, off-diagonal elements  $M_{13}$ ,  $M_{14}$ ,  $M_{23}$ , and  $M_{24}$  from the Ti  $2F4^+$ -STF can be transferred into the same elements of the Ti  $2F4^-$ -STF by inversion around  $(180^\circ, 0)$ , whereas a mirror operation at  $\phi = 180^\circ$  is necessary for elements  $M_{12}$ ,  $M_{22}$ ,  $M_{33}$  and  $M_{34}$ . Another characteristics for this chiral STF is that there is no symmetry within a single Mueller matrix elements as compared to all other achiral STF's discussed above. Most importantly, in both chiral STF's no pseudo-isotropic orientation can be observed.

Optical constants obtained from both chiral nanostructured films depicted in Fig. 6.14 are very similar and show the same dispersion relation. Differences between left and right handed  $2F4$ -STF can be observed in absolute values of  $n_c$  and  $k_c$ . In general, both sets of optical constants are in good agreement with the optical constants obtained from

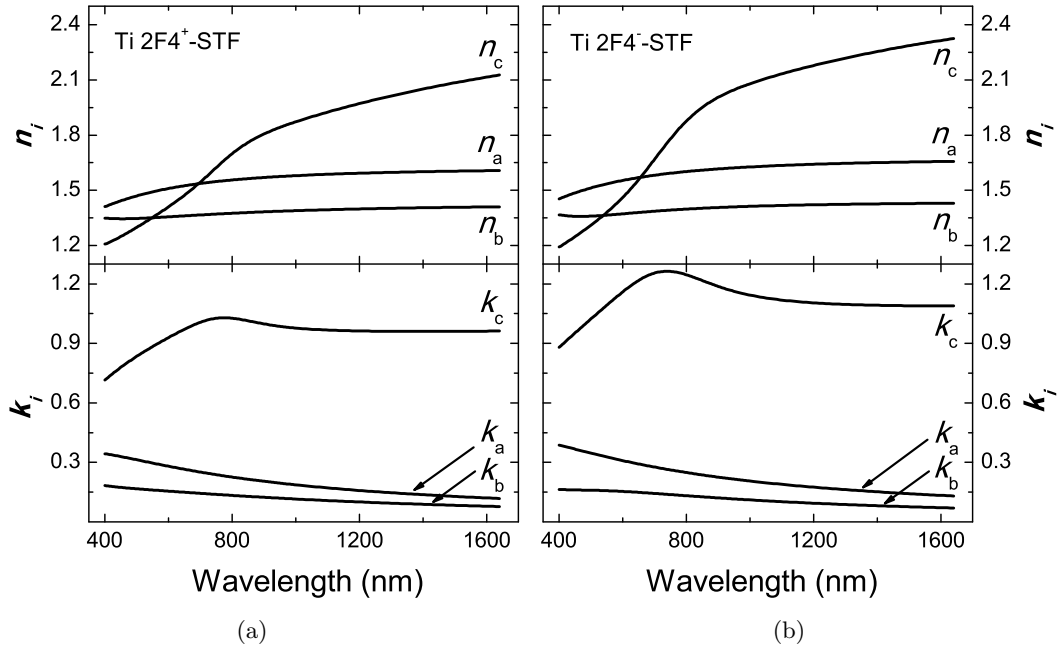


**Figure 6.14:** Refractive indices  $n_j$  and extinction coefficients  $k_j$  along major polarizability axes **a**, **b**, **c** with monoclinic arrangement of (a) a Ti 2F4<sup>+</sup>-STF and (b) a Ti 2F4<sup>-</sup>-STF. Optical constants depicted here are in good agreement with optical constants of Ti F1-STFs and Ti 2F2-STFs shown in Fig. 6.6 and Fig. 6.11, respectively.

Ti F1-STFs (Fig. 6.6). Furthermore,  $n$  and  $k$  along major polarizability axes **a**, **b**, **c** of the 2F4<sup>+</sup>-STF are in excellent agreement with optical constants obtained from the 2F2-STF (Fig. 6.11). Differences may be well explained with structure non-idealities due to non-constant evaporation source conditions, differences in deposition rates (Sect. 4.1), and the model assumption of ideal interfaces between bottom and top layers.

Other optically determined best-match parameters for both 2F4<sup>+</sup>-STF and 2F4<sup>-</sup>-STF are summarized in Table 6.1. Thickness  $d_j$  and slanting angle  $\theta_j$  for bottom ( $j = 1$ ) and top ( $j = 2$ ) layer, and the monoclinic angle  $\beta_1$  are in very good agreement between both films. The main difference between both STF is the angle between the two deposition steps  $\delta\varphi$ , which is nominally  $90^\circ$ . A deviation from  $90^\circ$  indicates that the two slanting planes are not orthogonal as expected from the growth parameters. It is not clear where the deviation of almost  $17^\circ$  for the 2F4<sup>+</sup>-STF is coming from but a possible source could be sample manipulator rotation non-idealities (see also Sect. 6.3.4). Best-match model calculations revealed that  $\beta_2$  was not changing and stayed constant around  $90.0 \pm 0.1^\circ$ . Consequently it was not included into the final

**Table 6.1:** Best-match model results for the Ti 2F4<sup>+</sup>- and 2F4<sup>-</sup>-STF and results from SEM micrograph analysis of Ti 2F4<sup>+</sup>. The error limits given in parentheses denote the uncertainty of the last digit (90% reliability).

Parameters	2F4 <sup>+</sup>	2F4 <sup>-</sup>	SEM 2F4 <sup>+</sup>
$d_1$ (nm)	65.3(3)	63.7(2)	63(3)
$d_2$ (nm)	50.7(1)	50.7(1)	65(5)
$\theta_1$ (°)	60.4(1)	60.5(1)	63(6)
$\theta_2$ (°)	62.0(1)	65.4(1)	67(5)
$\beta_1$ (°)	78.0(2)	76.5(3)	–
$\beta_2$ (°)	90	90	–
$\delta\varphi$ (°)	73.3(2)	85.7(2)	–
MSE	13.34	15.01	–

best-match calculation. The monoclinic angle of the bottom layer ( $\beta_1$ ) is comparable to the monoclinic angle of the Ti F1-STF discussed in Sect. 6.2.1. Hence, the second layer with perpendicular slanting direction has almost no influence on the monoclinic properties of the bottom layer in contrast to 2F2-STFs (Sect. 6.3.1). On the other hand, similar to 2F2-STFs, the top layer exhibits orthorhombic properties because there is no lateral conductive channel along which the necessary charge transfer could occur.

Best-match model parameters are well within the range determined by SEM micrograph analysis and the only discrepancy is the thickness of the second layer. This might be due to differences in density between both layers and hence, since identical optical constants for both layers are assumed, the denser layer is optically less thick.

### 6.3.3 U-shape Sculptured Thin Films (3F4-STFs)

Adding another layer to a 2F4-STF by further rotating the substrate 90° in the same direction as for the second layer results in a chiral U-shaped nanostructure abbreviated according to the proposed nomenclature 3F4-STF. Hence, slanting planes of top and bottom layer are parallel and nanocolumns are tilted in opposite directions, and the slanting plane of the sandwiched middle layer is perpendicular to top and bottom layers. The optical analysis of a 3F4<sup>+</sup>-STF (sample #7) from cobalt is exemplarily discussed (Fig. 6.15).

For the optical analysis the three-dimensional chiral Co 3F4<sup>+</sup> nanostructures were decomposed into three individual F1-STF layers. Consequently, the optical model was similar to the 2F4<sup>+</sup>-STF but with a third biaxial layer accounting for the third de-

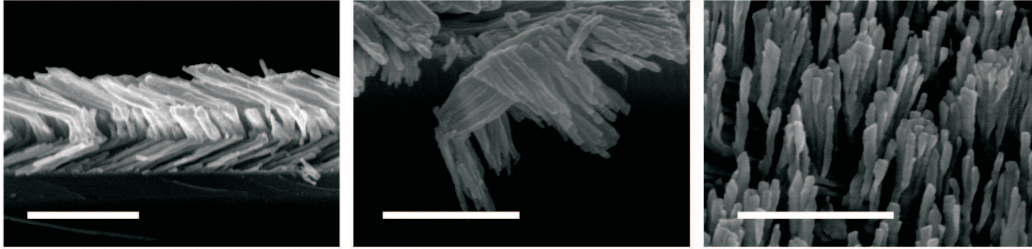


**Figure 6.15:** SEM micrographs of the Co 3F4<sup>+</sup>-STF: (left) cross-section view where both top and bottom layer are in the plane of the image, (middle) view on a structure ruptured from the substrate, which exhibits the homogeneous columns in form of a U-shape, and (right) top-view image revealing that some column bunching occurs but also free standing structures can be observed. Scale bars are 500 nm.

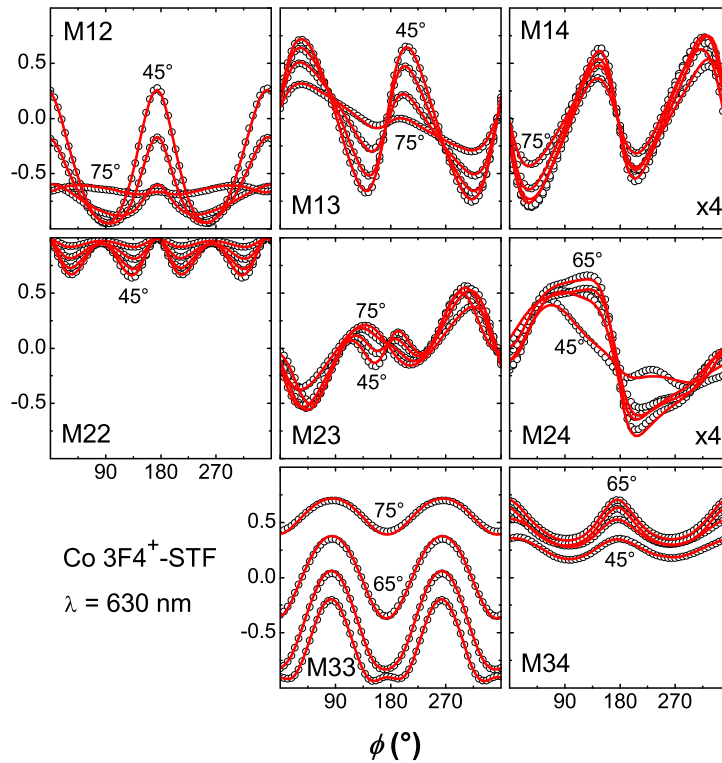


**Figure 6.16:** Exemplary experimental (circles) and best-match calculated (solid lines) GE data of a Co 3F4<sup>+</sup>-STF versus sample azimuth angle  $\phi$  at  $\lambda = 630$  nm. The four graphs for each Mueller matrix element are four different angles of incidence  $\Phi_a = 45^\circ, 55^\circ, 65^\circ, 75^\circ$ . Note that for this chiral STF no pseudo-isotropic orientation is present. Elements  $M_{14}$  and  $M_{24}$  are magnified  $\times 4$ .

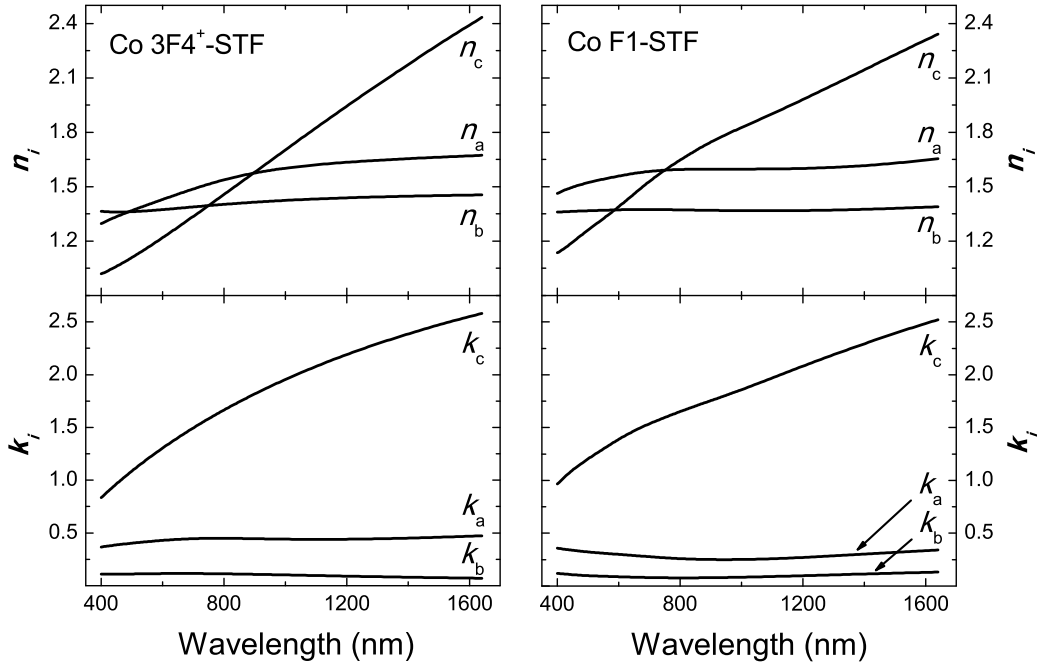


**Figure 6.17:** Refractive indices  $n_j$  and extinction coefficients  $k_j$  along major polarizability axes **a**, **b**, **c** with orthorhombic arrangement of a Co 3F4<sup>+</sup>-STF (left panel) in comparison with Co F1-STF (monoclinic arrangement; right panel).

position sequence (for model details see Sect. 3.2.6 and Sect. 6.3.2). The single set of major polarizabilities  $\varrho_a, \varrho_b, \varrho_c$  used in all three biaxial model layers has been parameterized with MDFs. Functions  $\varrho_a$  and  $\varrho_b$  contain three Lorentz oscillators each, and two Lorentz oscillators and one Drude term were incorporated for  $\varrho_c$ . For this particular thin film, the large error associated with the monoclinic angle and correlation between  $\beta$  and  $\theta$  hindered best-match model calculations with a monoclinic arrangement. Therefore, intrinsic biaxial properties were assumed to be orthorhombic ( $\alpha = \beta = \gamma \stackrel{\dagger}{=} 90^\circ$ ). Experimental and best-match model calculated GE Mueller matrix data for four different angles of incidence obtained from the Co 3F4<sup>+</sup>-STF are shown in Fig. 6.16. The graph depicts selected Mueller matrix elements versus sample azimuth at an exemplary wavelength  $\lambda = 630$  nm. Similar to the chiral Ti 2F4<sup>±</sup>-STFs, no pseudo-isotropic orientation can be observed. Note in particular the discrepancy of  $\Phi_a = 45^\circ$  in element  $M_{24}$ , and which does not intersect with the other  $\Phi_a$ -graphs at  $M_{24} = 0$ . However, sample orientations with minimum mode coupling can be identified near  $\phi = 180^\circ$  and  $\phi = 360^\circ$ , which coincide with sample directions when both slanting planes of bottom and top layer are parallel to the plane of incidence. Note that value and position of

**Table 6.2:** Best-match model results for the Ti 3F4<sup>+</sup> in comparison with values determined by SEM micrograph analysis. Subscripts 1, 2, and 3 denote bottom, middle, and top layer, respectively.  $\delta\varphi_{jk}$  is the angle between layer  $j$  and  $k$ . The error limits given in parentheses denote the uncertainty of the last digits (90% reliability).

Parameters	GE	SEM
$d_1$ (nm)	99(1)	135(10)
$d_2$ (nm)	87.1(8)	130(15)
$d_3$ (nm)	117.2(4)	130(15)
$\theta_1$ (°)	71.5(4)	66(3)
$\theta_2$ (°)	68.4(2)	65(5)
$\theta_3$ (°)	66.6(1)	65(7)
$\delta\varphi_{12}$ (°)	93.9(6)	–
$\delta\varphi_{23}$ (°)	75.3(2)	–
MSE	21.56	–

the minimum are wavelength-dependent. This behavior of orientations with minimum mode coupling is not due the non-perfect alignment  $\delta\varphi$  between two deposition steps (Table 6.2) but rather a characteristic of 3F4<sup>±</sup>-STFs, as calculations with  $\delta\varphi_{jk} = 90^\circ$  have revealed.

The set of optical constants derived under conditions of the above described model, common for all three biaxial layers, is in good agreement with optical constants determined from Co F1-STFs (Fig. 6.17). Deviations are attributed to the idealized interface between subsequent layers and the assumption of an orthorhombic symmetry for the optical model of the 3F4<sup>+</sup>-STF.

Further optically determined best-match parameters for the 3F4<sup>+</sup>-STF are summarized in Table 6.2. The MSE is considerably higher than for F1-STF, which is probably due to structure non-idealities such as column bunching as well as the non-consideration of possible monoclinic properties.

### 6.3.4 Helical Sculptured Thin Films (H-STFs)

In contrast to F-STFs, which are fabricated by sequential substrate rotations, helical chiral STFs are the consequence of a slow continuous substrate rotation. Optical analysis of a right- and left-handed Co H-STF with one turn each, 1H<sup>+</sup> (sample #8) and 1H<sup>−</sup> (sample #9), are discussed exemplarily here. Cross-sectional and top-view SEM images of both H-STFs are depicted in Figure 6.18.



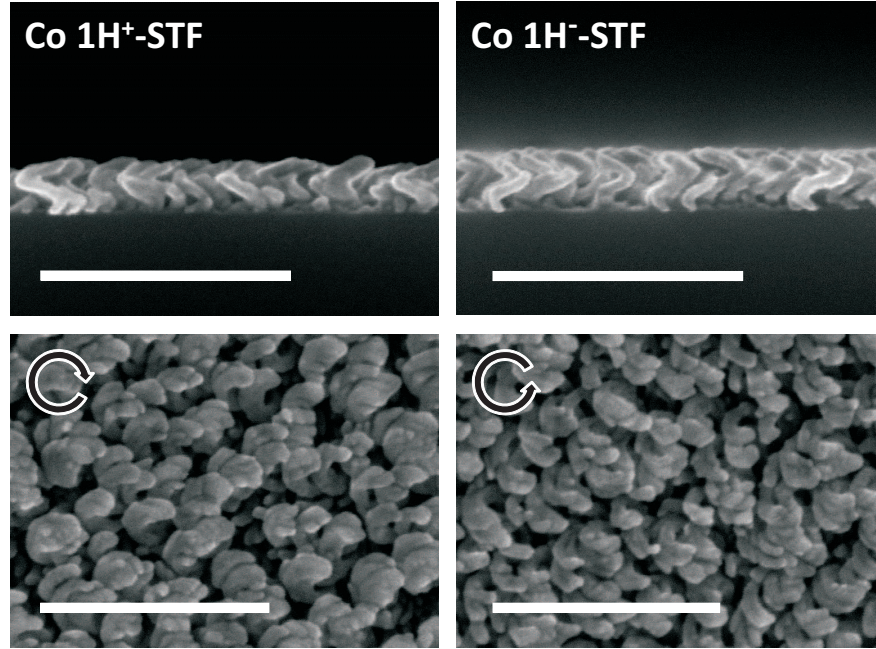


**Figure 6.18:** Cross-sectional (top row) and top-view (bottom row) SEM micrographs of the Co 1H<sup>+</sup>- and Co 1H<sup>-</sup>-STF. The arrows in form of a circle in the top-view image denote the handedness of each H-STF. Scale bars are 400 nm.

The optical model for H-STFs consists of multiple sublayers (slices) with dielectric function tensor descriptions rotated stepwise with respect to the sample normal between adjacent layers according to the handedness. This in-plane rotation  $\varphi$  (ideally homogeneous) from the substrate interface to the top of the structure accounts for the helical nature of the chiral nanostructures (for further model details see Sect. 3.2.6.3). The major polarizabilities  $\varrho_a, \varrho_b, \varrho_c$  equal for all sublayers have been parameterized with MDFs. For both H-STFs with different handedness, function  $\varrho_b$  contains two Lorentz oscillators and  $\varrho_c$  one Lorentzian oscillator and a Drude term.  $\varrho_a$  was parameterized with two and three Lorentzian oscillators for 1H<sup>+</sup>- and 1H<sup>-</sup>-STF, respectively.

Each H-STF was subdivided into 21 homogeneous anisotropic layers with a piecewise  $\delta\varphi$  rotated orthorhombic axes system ( $\mathbf{a}, \mathbf{b}, \mathbf{c}$ ;  $\alpha = \beta = \gamma = 90^\circ$ ; Fig. 3.8). This level of discretization was sufficient to reach close match between model and experiment. However, in order to achieve best-match model results, it was not possible to find a homogeneous  $\varphi$  rotation along  $z$  (substrate normal). A stepwise  $z$  profile for  $\varphi(z)$  was introduced with 8 nodes, and each node was divided into 3 slices. The nodes were fixed and equally spaced along  $z$  (spacing depends on the overall film thickness), and the

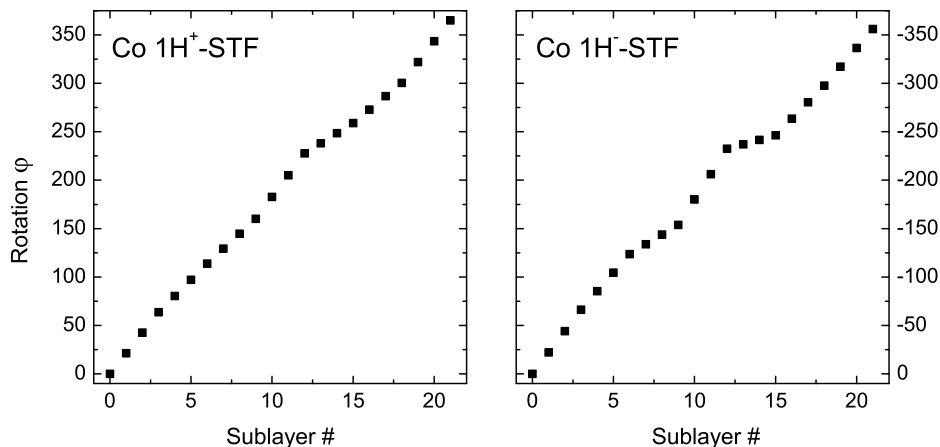


**Figure 6.19:** Non-homogeneous piecewise layer model for rotation of the principal dielectric function along  $z$ .

rotation  $\delta\varphi$  between two nodes was an additional free parameter during best-match model calculations (Fig. 6.19). Sample  $1H^+$ -STF reveals fairly homogeneous rotation with a small disturbance around  $225^\circ$ . Sample  $1H^-$ -STF reveals a similar profile with a more pronounced disturbance around the same  $\varphi$  rotation. These deviations from a homogeneous  $z$ -profile might be due to a sample wobble during substrate rotation.

Experimental and best-match model calculated GE Mueller matrix data for four different angles of incidence obtained from the Co  $H^+$ - and  $H^-$ -STF are shown in Fig. 6.20(a) and Fig. 6.20(b), respectively. The graph depicts selected Mueller matrix elements versus sample azimuth at an exemplary wavelength  $\lambda = 630$  nm. No pseudo-isotropic sample orientations can be identified.

Similar to the Ti chiral 2F2-STFs with opposite handedness, in case of ideal structures, off-diagonal elements  $M_{13}$ ,  $M_{14}$ ,  $M_{23}$ , and  $M_{24}$  from the  $H^+$ -STF can be transferred into the same elements of the  $H^-$ -STF by inversion around  $(180^\circ, 0)$  whereas a mirror operation at  $\phi = 180^\circ$  is necessary for elements  $M_{12}$ ,  $M_{22}$ ,  $M_{33}$ , and  $M_{34}$ . Another characteristics for these chiral STF is that there is no symmetry within a single Mueller matrix elements as compared to other achiral STF discussed above.

Optical constants obtained from both nanostructured thin films compare well and are depicted in Fig. 6.21. Note that the order of  $k_a$  and  $k_b$  is exchanged between both chiral H-STFs.

Other optically determined best-match parameters for both  $H^+$ - and  $H^-$ -STF are summarized in Table 6.3. Note that here the major polarizabilities within an orthorhombic arrangement are rotated with all three Euler angles and hence no principal

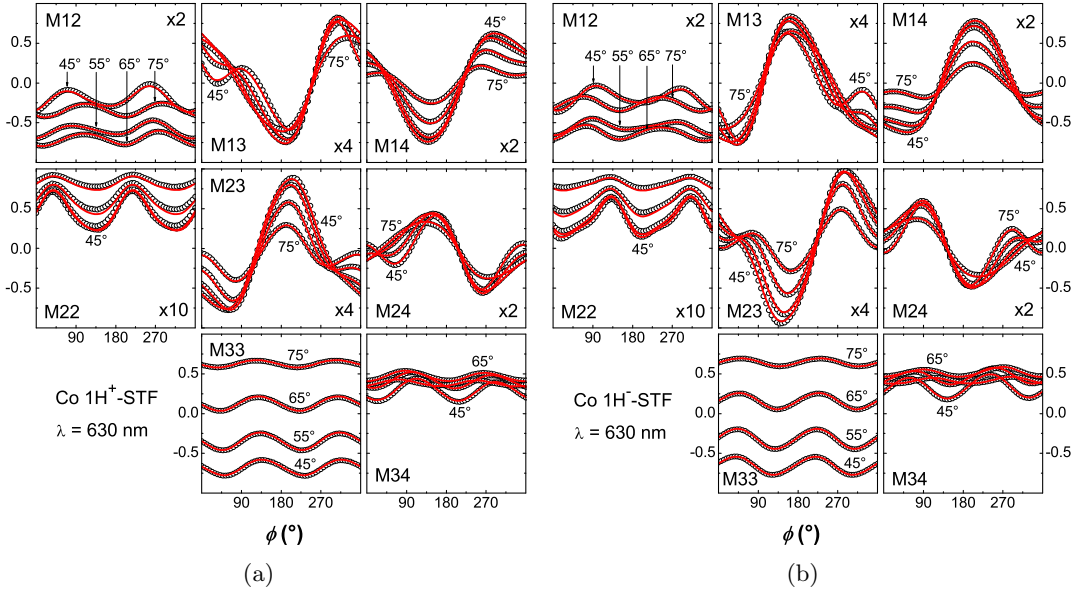


**Figure 6.20:** Exemplary experimental (circles) and best-match calculated (solid lines) GE data of a Co  $H^+$ -STF (a) and a Co  $H^-$ -STF (b) versus sample azimuth angle  $\phi$  at  $\lambda = 630$  nm. The four graphs for each Mueller matrix element are four different angles of incidence  $\Phi_a = 45^\circ, 55^\circ, 65^\circ, 75^\circ$ . Note that for both chiral H-STFs no pseudo-isotropic orientation is present. Numbers in upper or lower right corner of elements denote the factor with which data are magnified.

axis is parallel to the substrate interface anymore. The inclination angle  $\theta$  is representative of the tilt of the  $\mathbf{c}$ -axis, which determines the slope of the helical “windings”. The  $\mathbf{a}$ - and  $\mathbf{b}$ -axes orientations with respect to the substrate surface normal can be understood as effective polarization radii (due to the coordinate system rotation) of the chiral nanostructures. One may interpret these radii as effective coupling distances within which the individual nanostructures couple their dielectric polarization response.

**Helix diameter estimation.** Together with the total film thickness  $d$ , the inclination angle  $\theta$ , and the overall in-plane rotation  $\varphi_{\text{tot}}$  the pitch  $P = \frac{2\pi}{\varphi_{\text{tot}}} \cdot d$  and consequently the diameter  $\varnothing_h$  of a single helix can be computed as  $\varnothing_h = P / \tan \theta$ . This calculated diameter is not accounting for any “wire” thickness and has to be compared with an average between inner ( $\varnothing_{\text{in}}$ ) and outer ( $\varnothing_{\text{out}}$ ) diameter of the true helix determined from SEM image analysis [ $\varnothing_h \hat{=} \varnothing_{\text{avg}} = 0.5 \cdot (\varnothing_{\text{in}} + \varnothing_{\text{out}})$ ]. The calculated diameters for both H-STFs are with approximately 45 nm in good agreement with a SEM image estimates of the averaged diameter of  $\varnothing_{\text{avg}} = 50 \pm 5$  nm.

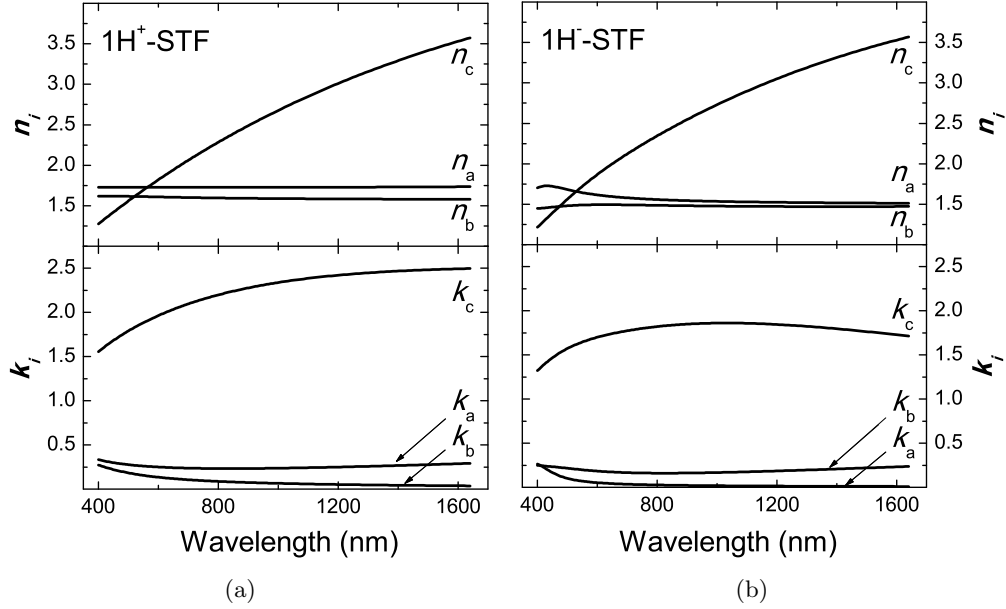


**Figure 6.21:** Refractive indices  $n_j$  and extinction coefficients  $k_j$  along major polarizability axes **a**, **b**, **c** with orthorhombic arrangement of (a) a Co  $H^+$ -STF and (b) a Co  $H^-$ -STF. Optical constants depicted here are in good agreement with optical constants of Co F1-STFs and Co 3F4-STFs shown in Fig. 6.2 and Fig. 6.17, respectively.

**Table 6.3:** Best-match model results for the Co  $H^+$ - and  $H^-$ -STF. The error limits given in parentheses denote the uncertainty of the last digit (90% reliability).

Parameters	$H^+$ -STF	$H^-$ -STF
$d$ (nm)	70.7(2)	76.2(2)
$\delta d$ (nm)	3.37	3.63
$\varphi_{\text{tot}}$ ( $^\circ$ )	365(3)	356(3)
$\theta$ ( $^\circ$ )	55.1(1)	59.6(1)
$\psi$ ( $^\circ$ )	25.4(9)	-15.2(5)
$\varnothing_h$ (nm)	48.6	45.2
MSE	8.457	6.353

### 6.3.5 Summary

- Complex layered STFs made with sequential substrate rotations can be considered cascaded F1-STFs. A piecewise homogeneous model comprising appropriately stacked F1-STF model layers can be used to predict the optical response of arbitrarily complex layered STFs.
- Achiral 2F2-STF have similar optical properties compared to F1-STF, especially pseudo-isotropic orientations are still present because both layers share the same slanting plane.
- Chiral 2F4- and 3F3-STFs do not exhibit any pseudo-isotropic orientation anymore; however, the Euler angle  $\psi = 0$  for all involved layers.
- The piecewise homogeneous biaxial layer approach can also be applied to chiral helical structures (H-STFs). A discretization level of approximately 30 sublayers per 100 nm thin film thickness results in very good agreement of experimental and best-match model data. H-STFs are the only STFs discussed here where  $\psi \neq 0$ . Also for H-STFs, no pseudo-isotropic sample orientations exist. Based on attained structural parameters from the best-match model calculations, the diameter of a single helix can be computed.

## 6.4 Host Variation

### 6.4.1 Environmental Influences

In Fig. 6.22 optical constants of the Co F1-STF (sample #1) determined from measurements taken 1 h after deposition are plotted (same as Fig. 6.2) and compared to  $n_j$  and  $k_j$  resulting from measurements acquired 90 d after deposition (for model and analysis details see Sect. 6.1.1). Between both measurements, the sample was stored in a closed yet not airtight container and thus exposed to ambient air. Therefore, differences between both results are attributed to growth of an oxide layer, changes in ambient humidity, and airborne contaminations\*.

In general, directions **a** and **b** show a very similar dispersion. In both cases,  $n_{a,b}$  and  $k_{a,b}$  from data taken after 90 d exhibit a positive offset, fairly constant over the investigated spectral region with respect to data acquired 1 h after deposition. No common trend is observed along direction **c**. The MDF parameterization delivered excellent

\*It is known that STFs are very sensitive to ambient changes and have been shown to be good candidates for sensitive and fast humidity sensors with capacitive or optical based readout<sup>6,119,120</sup>.

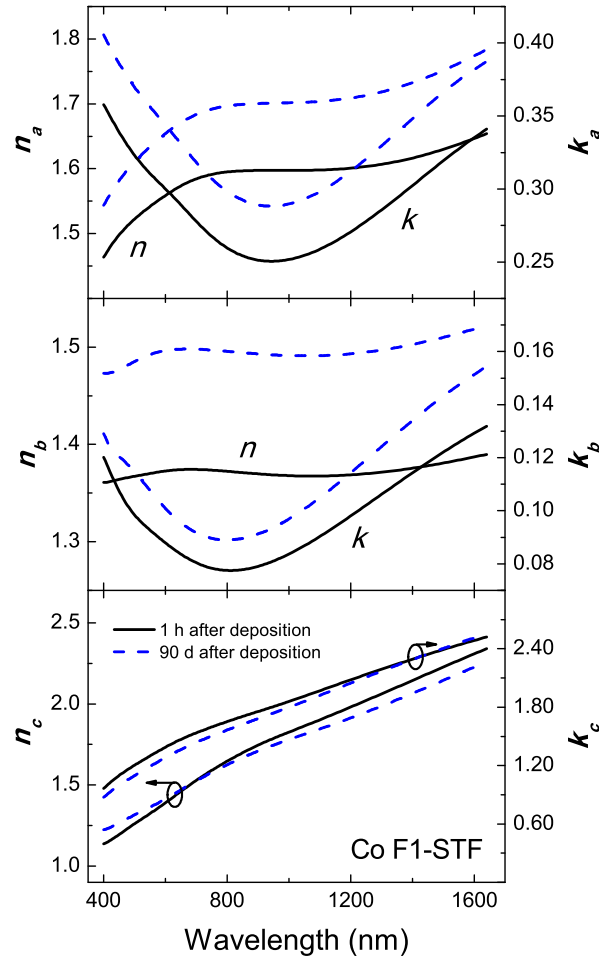


**Figure 6.22:** Comparison between refractive indices  $n_j$  and extinction coefficients  $k_j$  along major polarizability axes **a**, **b**, **c** with monoclinic arrangement of a Co F1-STF determined from measurements taken 1 h (solid line; same as Fig. 6.2) and 90 d (dashed line) after deposition, respectively.

results for both measurements and best-match model parameters are summarized in Table 6.4. Structural parameters are in very good agreement with SEM micrograph analysis ( $d = 114 \pm 4$  nm and  $\theta = 65 \pm 3^\circ$ ).

### 6.4.2 Hybridization by Polymer Infiltration

The optical constants of nanoporous thin films are effective optical constants, which depend not only on the STF geometry but also on the dielectric properties of the host material. Hence, optical properties of STFs can be influenced and tuned by combining

**Table 6.4:** Best-match model results for Co F1-STF 1 h and 90 d after deposition, respectively. Parameters  $A_j, E_{c_j}, \gamma_j$  correspond to amplitude, center energy, and broadening of the  $j$ th Lorentzian-type oscillator, respectively, whereas  $\rho, \tau$  represent the resistivity and scattering time of a Drude term, respectively. The error limits given in parentheses denote the uncertainty of the last digit (90% reliability).

	Structural Parameters	MDF Parameters along Direction			
		<b>a</b>	<b>b</b>	<b>c</b>	
1 h after deposition (MSE = 7.77)	$d = 106.9(1)$ nm	$A_1$ (eV)	1.00(1)	0.348(4)	0.3(3)
	$\theta = 63.68(1)^\circ$	$E_{c1}$ (eV)	0.633(4)	0.685(6)	1.43(6)
	$\beta = 83.69(9)^\circ$	$\gamma_1$ (eV)	0.90(3)	1.18(5)	0.6(3)
		$A_2$ (eV)	0.08(1)	0.12(2)	0.7(6)
		$E_{c2}$ (eV)	1.96(1)	2.56(9)	1.83(4)
		$\gamma_2$ (eV)	1.1(1)	2.4(2)	1.2(5)
		$A_3$ (eV)	0.88(1)	0.416(8)	0.8(7)
		$E_{c3}$ (eV)	5.2(1)	4.18(9)	2.7(1)
		$\gamma_3$ (eV)	8.2(5)	2.2(3)	2(1)
		$A_4$ (eV)	–	–	1.5(5)
		$E_{c4}$ (eV)	–	–	5(2)
		$\gamma_4$ (eV)	–	–	3(5)
		$\rho$ ( $\Omega\text{cm}$ )	–	–	$7.58(4) \times 10^{-4}$
		$\tau$ (fs)	–	–	0.325(3)
	$\varepsilon_{\text{off}}$	1.41(1)	1.62(1)	1.2(4)	
90 d after deposition (MSE = 6.77)	$d = 106.5(1)$ nm	$A_1$ (eV)	1.13(1)	0.435(4)	0.5(5)
	$\theta = 62.95(3)^\circ$	$E_{c1}$ (eV)	0.672(3)	0.700(5)	1.42(9)
	$\beta = 80.92(9)^\circ$	$\gamma_1$ (eV)	0.89(2)	1.16(4)	0.9(3)
		$A_2$ (eV)	0.13(2)	0.25(2)	0.8(8)
		$E_{c2}$ (eV)	2.02(1)	2.89(8)	1.85(5)
		$\gamma_2$ (eV)	1.4(1)	2.7(1)	1.3(6)
		$A_3$ (eV)	1.05(1)	0.47(2)	1.0(7)
		$E_{c3}$ (eV)	5.2(1)	3.90(9)	2.8(1)
		$\gamma_3$ (eV)	8.2(5)	1.0(2)	2.3(9)
		$A_4$ (eV)	–	–	1.5(4)
		$E_{c4}$ (eV)	–	–	5.6(1.5)
		$\gamma_4$ (eV)	–	–	3.2(4.6)
		$\rho$ ( $\Omega\text{cm}$ )	–	–	$7.11(4) \times 10^{-4}$
		$\tau$ (fs)	–	–	0.459(4)
	$\varepsilon_{\text{off}}$	1.50(2)	1.97(1)	1.5(3)	

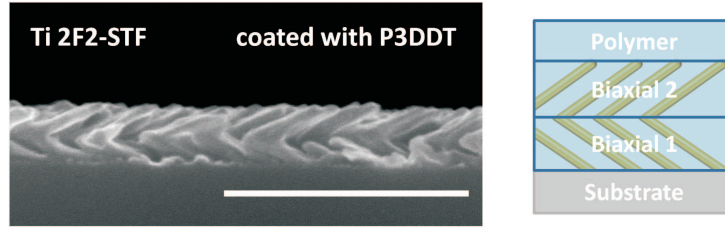


**Figure 6.23:** Cross-sectional SEM micrographs of the Ti 2F2-STF (sample #1) after hybridization with the semiconducting polymer P3DDT and schematic drawing of the ellipsometric layer model. The scale bar is 500 nm.

the inorganic nanoscaffold with an organic material thereby creating hybrid materials. The Ti 2F2-STF (sample #4) has been hybridized by infiltrating semiconducting P3DDT as described in Sect. 4.2, and changes of the anisotropic optical response are reported here. The optical model for the hybridized Ti 2F2-STF is similar to the as-deposited thin film discussed in Sect. 6.3.1, with an additional isotropic layer on top accounting for a polymer capping (Fig. 6.23). It was assumed that the nanoscaffold is not affected by the hybridization process and hence experimental data of both measurements (before and after hybridization) were modeled simultaneously with a multi-sample analysis. The multi-sample analysis allows for using the same Euler angles  $\theta_{1,2}$  and layer thicknesses  $d_{1,2}$  in the both models for as-deposited and hybridized Ti 2F2-STF.

Refractive indices  $n_j$  and extinction coefficients  $k_j$  depicted in Fig. 6.24 are obtained with parameterized MDFs. Significant changes upon hybridization are observed and  $n_j$  and  $k_j$  are increased in the investigated spectral region with respect to the as-deposited 2F2-STF. The additional shoulders in the short wavelength region appearing in the hybridized optical constants might be due to the infiltrated polymer. Birefringence and dichroism changes are observed upon P3DDT infiltration and are depicted in Fig. 6.25. The P3DDT capping layer thickness of the hybridized Ti 2F2-STF is  $d_{\text{cap}} = 0.90 \pm 0.05$  nm and other optically determined parameters are summarized in Table 6.5. Note that  $n_j$  and  $k_j$  of the as-deposited film were determined from angle-resolved GE measurements acquired approximately 60 d after the deposition and prior to the hybridization process. Differences in the optical constants and structural properties determined immediately after deposition (Fig. 6.11) and prior to hybridization are similar to what has been found in the previous section for Co F1-STFs. The monoclinic angle of the bottom layer ( $\beta_1$ ) increased after the hybridization process from  $55^\circ$  to almost  $70^\circ$ , which might be due to additional charge transfer channels through



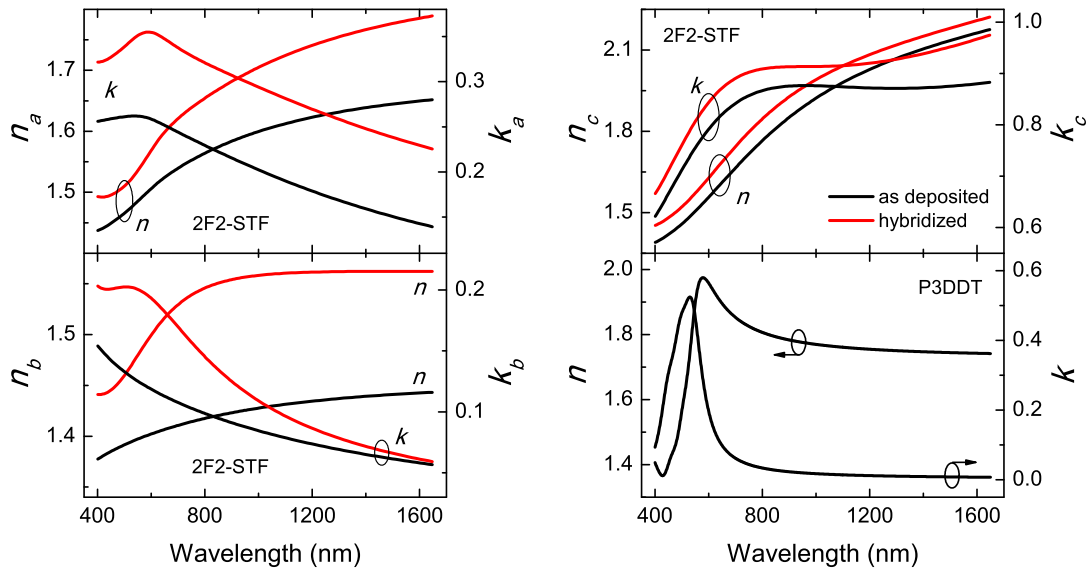


**Figure 6.24:** Refractive indices  $n_j$  and extinction coefficients  $k_j$  along major polarizability axes **a**, **b**, **c** of the as-deposited (black) and hybridized Ti chevron nanostructures (red), respectively. The estimated uncertainty of the determined  $n$  and  $k$  values for both samples is less than 1%. The lower right graph depicts the optical constants from P3DDT (adapted from Müller *et al.*<sup>108</sup>).

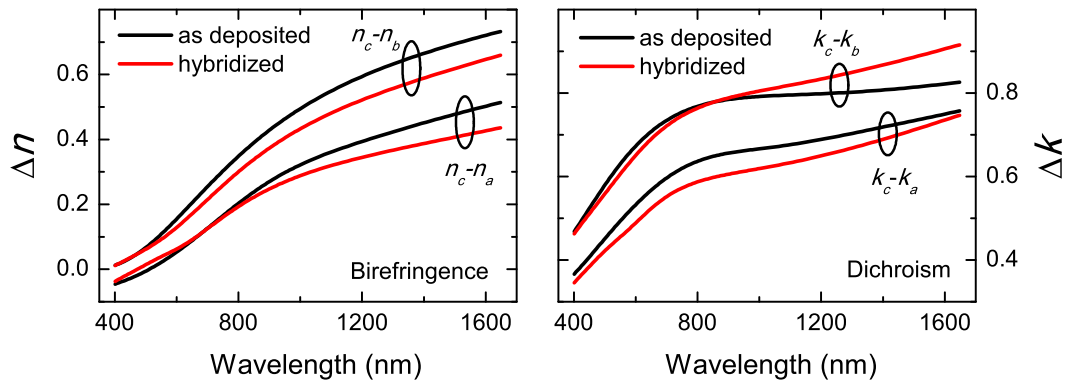


**Figure 6.25:** Birefringence and dichroism of the Ti 2F2-STF before and after hybridization with P3DDT.

the semiconducting polymer P3DDT. Cross-sectional SEM images after hybridization reveal that the voids are only partially filled and the polymer homogeneously covers the 2F2 nanostructures (Fig. 6.23, compare to the SEM image of the as-deposited thin film depicted in Fig. 6.9). It can be expected that if voids are completely filled with semi-

conducting polymer, individual layers of the hybrid thin film will exhibit orthorhombic optical properties.

In average, the relative changes in  $n_c$  and  $k_c$  upon hybridization are smallest compared to  $n_{a,b}$  and  $k_{a,b}$ , which might be due to the fact that rather the diameter of the chevron nanostructures is changed than their length. Strong changes upon polymer infiltration of more than 6% and 50% for  $n_a$  and  $k_a$ , respectively, in the near infrared spectral region could be exploited for new optical sensor concepts. Furthermore, such investigations on hybrid nanostructures might be particularly interesting for the emerging field of hybrid photovoltaic applications<sup>17</sup>.

**Table 6.5:** Best-match model results for Ti 2F2-STF comparing parameters determined with a two-layer monoclinic model approach after deposition, and before (60 d after deposition) and after hybridization with SEM image analysis from the as-deposited 2F2-STF. Parameters  $d_j$ ,  $\theta_j$ , and the MSE are identical for measurements before and after hybridization because they are results from a multi-sample analysis. The error limits given in parentheses denote the uncertainty of the last digit (90% reliability).

Parameters	1 h After Deposition	Before Hybridization	After	SEM
$d_1$ (nm)	49.1(5)	48.4(2)		55(5)
$d_2$ (nm)	65.0(4)	65.9(2)		64(5)
$\theta_1$ (°)	61.8(2)	62.7(1)		62(5)
$\theta_2$ (°)	63.1(2)	61.6(1)		65(6)
$\beta_1$ (°)	58(1)	55.2(4)	69.6(6)	–
$\beta_2$ (°)	88.4(3)	89.4(1)	87.6(2)	–
$\delta\varphi$ (°)	177.80(7)	177.67(5)	178.15(6)	–
MSE	7.987	16.31		–

### 6.4.3 Summary

- Optical constants of STFs are very sensitive to host (environmental) variations, which in turn can be exploited for optical sensor concepts.
- Birefringence and dichroism changes are observed upon hybridization of Ti 2F2-STFs with the semiconducting polymer P3DDT. The monoclinic angle  $\beta$  is also affected and increases upon polymer infiltration into voids.

## 6.5 Effective Medium Approximations for F1-STFs

Bulk material optical constants can be modified using effective medium approximations (EMAs) to attain approximate effective optical constant of a thin film comprising more than one constituent. The advantage of using EMAs for ellipsometric data analysis is the direct access to a material fraction parameter related to the amount of the mixed constituents. The anisotropic Bruggeman EMA<sup>83,121</sup> (AB-EMA) has been applied here to estimate the void fraction in F1-STFs by mixing bulk optical constants (inclusions) with void (host). The thereby obtained anisotropic optical constants are compared to results obtained with the homogeneous biaxial layer approach (for details on both model approaches see Sect 3.2.6). When comparing both approaches one must bear in mind that the homogeneous biaxial layer approach allows for monoclinic optical properties, whereas the AB-EMA is forced to model orthorhombic optical properties only. Thus, to a certain degree, the AB-EMA will not match the observed ellipsometric response as good as the here developed homogeneous biaxial layer approach.

Investigations on complex STFs (other than F1-STFs) have shown that structural properties such as slanting angles and film thicknesses determined with the AB-EMA approach are too far off from SEM micrograph analysis and no reasonable match between experimental and best-match model data could be achieved. Therefore, the AB-EMA approach is only presented for F1-STFs here.

**Model description.** The optical model for F1-STFs comprises a single biaxial (orthorhombic) layer. Optical constants of the respective bulk material are mixed with fractions of void  $f_v$  (optical constants  $n_v = 1, k_v = 0$ ) and weighted with depolarization factors ( $L_j^D, j = a, b, c$ ) for the three biaxial effective dielectric functions.  $L_j^D$  define the shape of the aligned “inclusions” and hence the difference between  $n_j$  and  $k_j$  along axes **a**, **b**, **c**. Euler angles  $\varphi, \theta, \psi$  transform the Cartesian laboratory coordinate frame into the material coordinate frame. The total film thickness  $d$  completes the best-match model parameter list.

### 6.5.1 Cobalt F1-STF

Cobalt bulk optical constants for the AB-EMA layer have been taken from Palik<sup>117</sup> and are depicted in Fig. 6.2. Optical constants determined with the AB-EMA are compared to data obtained with the homogeneous biaxial layer approach (Sect. 6.1.1)\*

---

\*Here, data is compared that has been taken immediately after deposition and consequently no oxide layer was included within the AB-EMA.

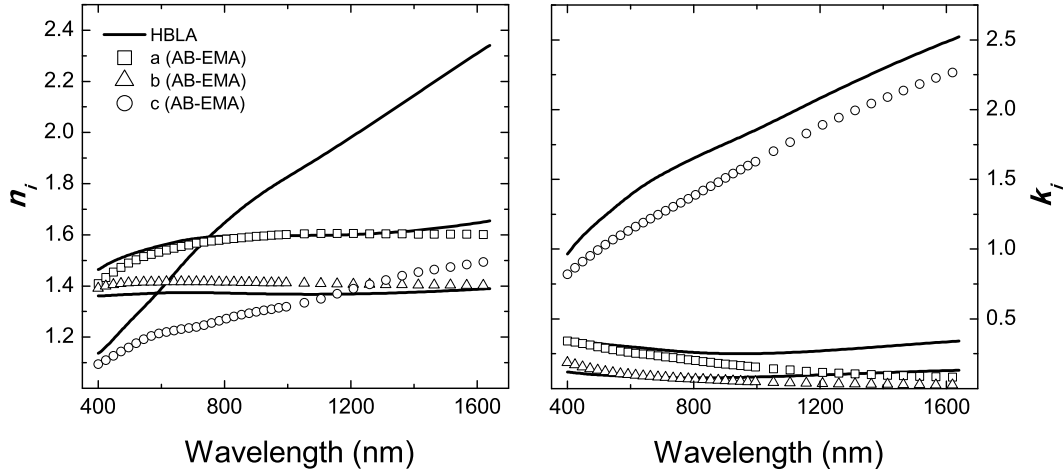


**Figure 6.26:** Refractive indices  $n_j$  and extinction coefficients  $k_j$  along major polarizability axes **a**, **b**, **c** of a Co F1-STF determined by the homogeneous biaxial layer approach (HBLA, monoclinic; solid line) compared to optical constants determined by the AB-EMA (orthorhombic; symbols).

and plotted in Fig 6.26. The general trend of optical constants determined with both approaches is in good agreement, however, the refractive index  $n_c$  differs strongly. This mismatch is also reflected in the MSE, which is with 66.7 almost nine times higher than for the homogeneous biaxial layer approach (MSE = 7.77, see Table 6.4). However, structural parameters such as thickness  $d = 104.1 \pm 0.1$  nm and columnar slanting angle  $\theta = 59.16 \pm 0.04^\circ$  are in good agreement with values determined with the homogeneous biaxial layer approach. The void fraction  $f_v = 76.85 \pm 0.03\%$  reflects the high porosity of the film. The depolarization factors ( $L_c^D = 0.125$ ,  $L_a^D = 0.392$ , and  $L_b^D = 0.483$ ) show that the structural unit is extended in the **c**-direction since  $L_c^D$  is considerably smaller than the other two parameters, and the fact that  $L_a^D \neq L_b^D$  indicates that the film is rendered with biaxial properties<sup>122</sup>.

Based on existing literature<sup>122,123</sup> and investigations presented in this thesis an empirically found order of depolarization factors is  $L_a^D > L_b^D > L_c^D \neq 0$ . Because the columns are not infinitely long along the **c**-axis the depolarization factor  $L_c^D$  should not be assumed to be equal to zero. These depolarization factors then are representative for a structural unit extended along the **c**-axis, since  $L_c^D$  is smaller than the other two parameters, and  $L_a^D \neq L_b^D$  shows that the film has biaxial properties.  $L_a^D > L_b^D$  is also in agreement with the observed elliptical shape of the columns with a longer axis perpendicular to the incoming vapor flux due to anisotropic shadowing effects during oblique angle deposition<sup>47,81</sup>. In general, structural parameters and void fraction at-

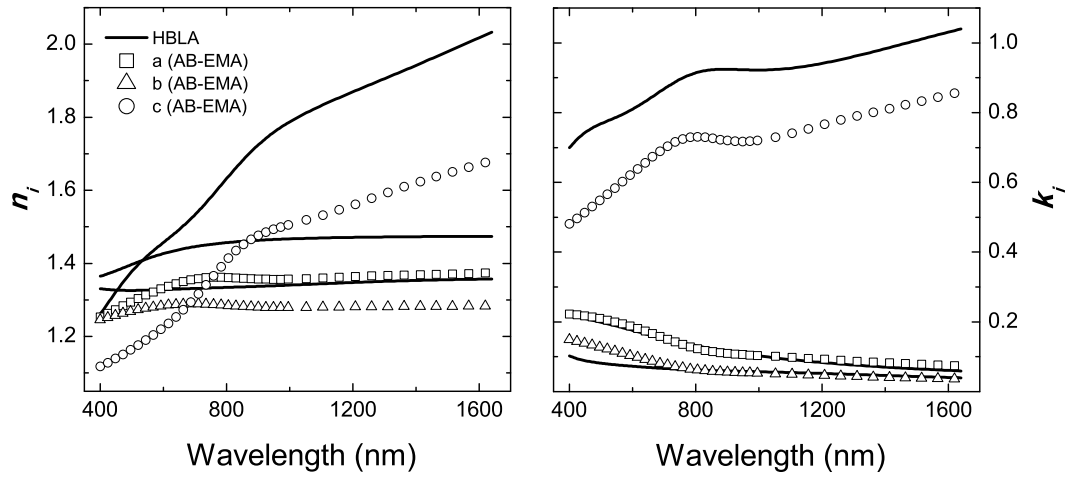


**Figure 6.27:** Refractive indices  $n_j$  and extinction coefficients  $k_j$  along major polarizability axes **a**, **b**, **c** of a Ti F1-STF determined by the homogeneous biaxial layer approach (HBLA, monoclinic; solid line) compared to optical constants determined by the AB-EMA (orthorhombic; symbols).

tained with the AB-EMA are in fair agreement with SEM analysis and may serve as a good estimate.

### 6.5.2 Titanium F1-STF

Titanium bulk optical constants for the AB-EMA layer have been taken from Palik<sup>117</sup> and are depicted in Fig. 6.6. Figure 6.27 shows the optical constants determined with the homogeneous biaxial layer approach and with the AB-EMA for Ti F1-STFs. Parameters for the Ti F1-STF obtained with both approaches as well as SEM image analysis are summarized in Table 6.6. In general, depolarization factors compare well to  $L_j^D$  determined for the Co F1-STF above.

### 6.5.3 Supermalloy F1-STF

Supermalloy bulk optical constants for the AB-EMA layer have been generated as described in Sect. 6.2.2 and are depicted in Fig. 6.8. Figure 6.28 shows the optical constants determined with the homogeneous biaxial layer approach and with the AB-EMA for supermalloy F1-STFs. Obtained parameters with both approaches as well as SEM image analysis are summarized in Table 6.7.

**Table 6.6:** Best-match model results from homogeneous biaxial layer approach (HBLA), AB-EMA, and SEM analysis for the Ti F1-STF. The error limits given in parentheses denote the uncertainty of the last digit (90% reliability).

Parameters	HBLA	AB-EMA	SEM
$d$ (nm)	100.2(2)	114.5(1)	112(4)
$\theta$ ( $^\circ$ )	57.27(6)	55.43(5)	58(4)
$\beta$ ( $^\circ$ )	80.2(1)	90 (fix)	–
$f_v$ (%)	–	80.96(2)	–
$L_a^D$	–	0.390(1)	–
$L_b^D$	–	0.477(1)	–
$L_c^D$	–	0.133(1)	–
MSE	6.23	31.35	–

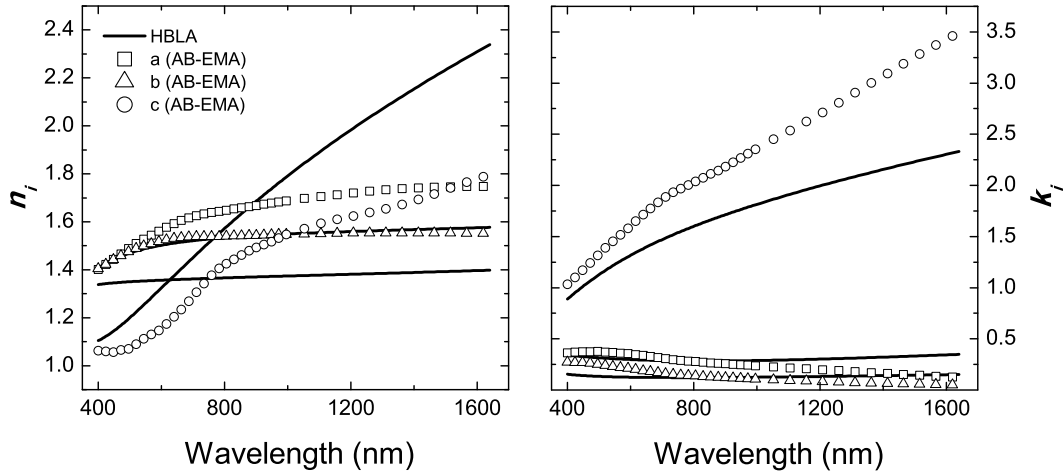


**Figure 6.28:** Refractive indices  $n_j$  and extinction coefficients  $k_j$  along major polarizability axes **a**, **b**, **c** of a NiFeMo F1-STF determined by the homogeneous biaxial layer approach (HBLA, monoclinic; solid line) compared to optical constants determined by the AB-EMA (orthorhombic; symbols).

**Table 6.7:** Best-match model results from homogeneous biaxial layer approach (HBLA), AB-EMA, and SEM analysis for the NiFeMo F1-STF. The error limits given in parentheses denote the uncertainty of the last digit (90% reliability).

Parameters	HBLA	AB-EMA	SEM
$d$ (nm)	88.4(1)	79.1(1)	100(4)
$\theta$ ( $^\circ$ )	63.16(3)	57.47(6)	64(4)
$\beta$ ( $^\circ$ )	89.53(8)	90 (fix)	–
$f_v$ (%)	–	70.8(1)	–
$L_a^D$	–	0.447(1)	–
$L_b^D$	–	0.514(1)	–
$L_c^D$	–	0.039(1)	–
MSE	5.18	44.5	–

#### 6.5.4 Summary

- Optically determined structural properties obtained with the AB-EMA may serve as good estimates and have the advantage of a direct access to the void fraction. However, since the current AB-EMA formalism is forced to model orthorhombic optical properties, no access to the monoclinic angle is provided and the error bar on best-match model calculations is considerably higher compared to the homogeneous biaxial layer approach. Therefore, optical constants determined with the AB-EMA may only serve as estimates.
- The empirically found order of depolarization factors for metal F1-STFs is  $L_a^D > L_b^D > L_c^D \neq 0$ .  $L_c^D$  should not be zero because the column has a finite length.
- The AB-EMA approach fails completely for complex STFs other than F1-STFs.

## 6.6 Literature Discussion

### 6.6.1 Early Optical Investigations on Sculptured Thin Films

Kundt<sup>25</sup> reported on birefringence in metal thin films deposited at oblique angles already in 1886 and concluded that the specific microstructure may be the origin, while electron microscopy or similar techniques were unavailable. Smith, Cohen, and Weiss<sup>124</sup> determined with polarized transmission measurements that the absorption coefficient in obliquely deposited metal films is a periodic function of the sample azimuth and that the differential absorption (parallel versus perpendicular to the slanting plane of the

columns) increases with increasing deposition angle  $\theta_i$ . King and Talim<sup>125</sup> considered the effect of columnar microstructure on the optical anisotropy of thin films deposited onto substrates at normal incidence with the help of ellipsometry and other techniques and postulated an uniaxial model. Inspired by this work, Hodgkinson *et al.*<sup>126</sup> performed polarization dependent reflection measurements on obliquely deposited transparent ZrO<sub>2</sub> and TiO<sub>2</sub> F1-STFs. They proposed an orthorhombic biaxial model due to the existence of form birefringence; i.e., the obliquely deposited columns do not exhibit a perfectly round shape but are rather elliptically in shape. The authors realized that there is no mode coupling between  $p$  and  $s$  polarization for light incident in the plane containing the direction of deposition and the substrate normal. These orientations are equivalent to the pseudo-isotropic orientations discussed for example in Sect. 6.1 (Fig. 6.1).

### 6.6.2 Effective Medium Approximations for F1-STFs

In order to quantify birefringence and porosity values of F1-STFs in the visible spectral region from transparent oxides (metal oxides and SiO<sub>2</sub>), initially empirical equations<sup>127,128</sup> have been reported and then existing EMAs applied (Bragg-Pippard<sup>81,129</sup>, Maxwell-Garnett<sup>89,130</sup>, and AB-EMA<sup>131,132,133,134</sup>).

Hodgkinson and Wu<sup>81</sup> reported based on optical constants determination with EMAs that in dielectric biaxial F1-STF the optical constants generally follow the empirically found order  $n_c > n_a > n_b$ . The same order is found here for all investigated STFs in the near infrared spectral region. However, presented data in this thesis over an extended spectral region reveal the order of refractive indices for metal STFs is different in the visible spectral region since  $n_c$  is intersecting with  $n_a$  and  $n_b$ .

Depolarization factors deliver information about the shape of the inclusions. However, it is not understood, which value of  $L_c^D$  should be used for F1-STF. Often, it is claimed that the depolarization factor along the long axis of ellipsoids ( $\mathbf{c}$ -axis) should be zero because of minimum charge screening effects along this direction and many authors have therefore assumed  $L_c^D = 0$  for their best-match model calculations in order to determine optical constants and porosity values of F1-STFs<sup>81,87,129,130,131,132,135,136</sup>. Mbise *et al.*, however, reported on analysis of polarized transmittance measurements using an AB-EMA to quantify optical anisotropy of Cr F1-STFs. The authors determined depolarization factor values  $0.14 < L_c^D < 0.45$  and found that optically determined structural properties such as film thickness and structure inclination are in fair agreement with SEM investigations<sup>122,123</sup>.



### 6.6.3 Optical Properties of Complex and Hybrid STFs

**Chevron-like nanostructures (*l* F2-STFs).** Motohiro and Yaga<sup>137</sup> rotated their sample manually by 180° to grow two successive F1-STF layers with opposite slanting direction and experimentally determined that a non-absorbing metal oxide 2F2-STF can be used as a quarter-wave plate and can compete with conventional types of retardation plates. The authors realized that 2F2-STFs show superior retardation properties with respect to F1-STFs.

Podraza *et al.*<sup>89</sup> matched Jones matrix data of a non-absorbing MgF<sub>2</sub> 2F2-STF with a similar approach than the one used in this thesis and found good agreement between optically determined structural properties and their SEM analysis. However, they assumed uniaxial properties in the transparent region of their MgF<sub>2</sub> films and included measured data from only one in-plane orientation into their best-match model calculations. For determination of optical properties and thin film birefringence the authors used an Maxwell-Garnett EMA<sup>87,138</sup> with depolarization factors 0 and 1 parallel and perpendicular to the long axis of the nanostructure, respectively, to parameterize both principal dielectric functions.

**Four-fold staircase nanostructures (*l* F4-STFs).** The geometry of a 3F4-STF can be seen as the three-dimensional equivalent of a two-dimensional split ring resonator<sup>139,140,141</sup>. Such three-dimensional metamaterials from metal have gained research interest because effective negative index and magnetic resonances have been proposed<sup>142,143</sup>. Besides that, dielectric (4F4)<sub>*x*</sub>-STFs with  $x = 4, 5$  are found to act as three-dimensional photonic bandgap crystals with wide bandgaps<sup>144</sup>. However, no reports on intrinsic optical properties of F4-STFs have been found.

**Helical nanostructures (*t* H-STFs).** In search of new materials to miniaturize existing polarization rotators (Reusch rotator) and potentially create thin film Šolc color filters<sup>145</sup>, Young and Kowal<sup>29</sup> were the first ones to report on in-situ substrate rotation during oblique angle evaporation thereby creating CaF<sub>2</sub> H-STFs. However, even though optical activity and large polarization rotation was experimentally confirmed their paper from 1959 went largely unnoticed. Recently efforts have been made mostly in the theoretical description of light propagation in H-STFs lead by Lakhtakia<sup>27,146,147</sup>. Experimental reports about chiral H-STFs are dealing with selective transmission of left- and right- circularly polarized light and optical rotary power. H-STFs, which can be physically considered as “frozen” cholesteric liquid crystals<sup>105</sup> are found to be good

circular polarizers since light with the same handedness as the helix is blocked, whereas it transmits the other (within a certain frequency range)<sup>148,149,150,151,152,153</sup>.

However, except for Zhong *et al.*<sup>154</sup>, who modeled the optical properties of helical ITO thin films with a Cauchy dispersion model, all other reports mentioned above do not report on intrinsic optical properties of the investigated H-STFs.

**Hybrid STFs.** Photonic characteristics, for example, may be modified and tuned by infiltrating a dielectric material in void<sup>129,155,156</sup>. Active control over optical properties of hybrid materials can be achieved by either combining nanoparticles with polymers, which change their properties upon exposure to gases<sup>157</sup> or inorganic porous layers with temperature sensitive liquid crystals<sup>158</sup>, for example. Therefore, optical constants of hybrid nanoporous thin films are effective optical constants, which depend not only on the geometry but also on the dielectric properties of the material infiltrated into void.

The decrease in birefringence observed upon infiltration of the conductive polymer P3DDT is in agreement with a recent report on TiO<sub>2</sub> F1-STFs: May *et al.*<sup>129</sup> observed decreased birefringence values with increasing filling fraction of void spaces when substituting air with toluene.

# Chapter 7

## Magneto-Optical Properties of Co F1-STFs

Magneto-optic generalized ellipsometry (MOGE), a non-destructive and non-invasive optical technique, has been shown to be highly suitable for determination of the complex anisotropic dielectric function tensor of complex and multilayered samples<sup>96,97,159</sup>.

In this chapter, spectroscopic MOGE in the traditional polar and longitudinal magneto-optical Kerr effect (MOKE) configuration on a Co F1-STF (sample #1) is discussed. The anisotropic dielectric tensor has been determined, giant Kerr rotation calculated and measured, and the resulting magnetization direction estimated upon exposure to longitudinal and polar external magnetic fields. Furthermore, an outlook into vector magneto optical generalized ellipsometry (VMOGE) is given and analysis of first data presented.

### 7.1 Polar Kerr Effect Geometry

#### 7.1.1 Experiment

MOGE measurements and data analysis of the Co F1-STF were done in three steps, to minimize cross-correlation between varying parameters. First, multiple angle of incidence Mueller matrix ellipsometry measurements were carried out on the M2000VI ellipsometer without an external magnetic field and sample analysis for monoclinic F1-STFs done as discussed in Sect. 6.1.1. Parameters determined from this investigation are total film thickness  $d = 107.9$  nm, slanting angle  $\theta = 63.3^\circ$ , and monoclinic angle  $\beta = 81.0^\circ$ . Subsequently, the sample was transferred to the polar magneto-optic Kerr effect setup (Sect. 3.3.5.1) and spectroscopic Mueller matrix measurements at  $\mu_0 H = 0$  T were analyzed using the model obtained in the first step, in order to accurately determine sample azimuth and angle of incidence parameters. Spectroscopic GE measurements were then taken with applied external magnetic fields for several azimuthal sample positions and only the wavelength-dependent complex magneto-optic

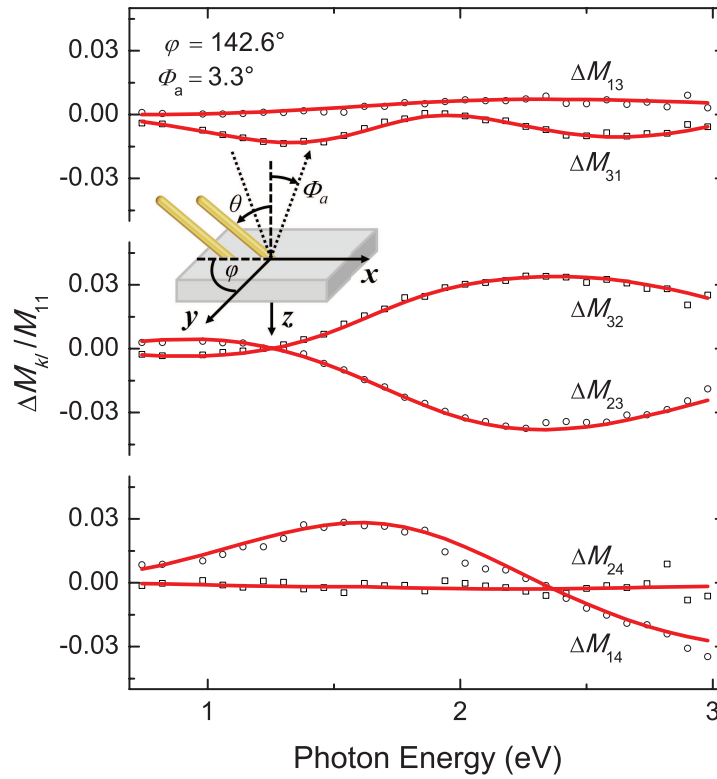


**Figure 7.1:** Experimental (symbols) and best-match model calculated (solid line) magnetic field-induced difference data  $\Delta M_{kl} = M_{kl}(\mu_0 H = -1.8 \text{ T}) - M_{kl}(\mu_0 H = 1.8 \text{ T})$  normalized to  $M_{11}$  for a Co F1-STF. The inset shows a schematic drawing of the sample with in-plane orientation  $\varphi$ , column tilt  $\theta$ , and angle of incidence  $\Phi_a$ .

polarizability parameter  $\varepsilon_{xy}^P$  was determined by matching the calculated Mueller matrix difference  $\Delta M_{kl} = M_{kl}(-\mu_0 H) - M_{kl}(\mu_0 H)$  with the experiment. Data analysis of this final step was done both on a wavelength-by-wavelength basis as well as with a parameterized MDF while data for all measured in-plane orientations were matched simultaneously with a multi-parameter analysis.

### 7.1.2 Giant Magneto-Optical Polarizability

Figure 7.1 shows experimental data as well as best-match model data of selected elements of the Mueller matrix difference  $\Delta M_{kl}$  normalized to  $M_{11}$  for a Co F1-STF at an external magnetic field  $\mu_0 H = \pm 1.8 \text{ T}$  and in-plane orientation of  $\varphi = 142.6^\circ$ . Note that an in-plane orientation of  $\varphi = 90^\circ$  represents the situation where the slanted columns are parallel to the plane of incidence and pointing toward the source (see inset).

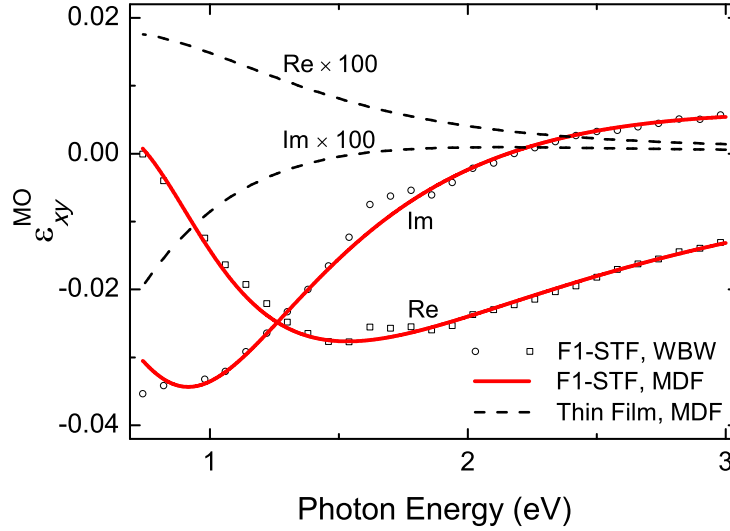


**Figure 7.2:** Real (Re) and imaginary (Im) parts of functions  $\varepsilon_{xy}^{\text{MO}}$  from a Co F1-STF ( $\mu_0H = 1.8$  T) and a 60 nm thick solid Co film ( $\mu_0H = 1.5$  T; spectra multiplied by 100). Symbols and solid lines for the F1-STF are results from a wavelength-by-wavelength (WBW) and a model dielectric function (MDF) analysis, respectively, and experimental data shown in Fig. 7.1.

Generated and experimental data are in excellent agreement.

While data at different in-plane orientations  $\varphi$  differ due to the monoclinic anisotropy, measurements at multiple in-plane orientations,  $\varphi = 0^\circ, \pm 45^\circ,$  and  $180^\circ$ , revealed no magneto-optic in-plane anisotropy. That is, it was sufficient to add  $\varepsilon^{\text{MO}}$  to the dielectric part  $\varepsilon^{\text{D}}$  after Euler angle rotation to model different in-plane orientations. Therefore, it is concluded that magnetic domains orient along the external magnetic field regardless of  $\varphi$  (i.e., not along the columns) and the corresponding model scenario is represented by (3.57), where  $\varepsilon^{\text{MO}}$  possesses no  $\varphi$  dependence and  $\varepsilon_{xz}^{\text{T}} = \varepsilon_{yz}^{\text{L}} = 0$ .

Real and imaginary parts of the complex magneto-optic polarizability function  $\varepsilon_{xy}^{\text{P}}$  at  $\mu_0H = 1.8$  T are depicted in Fig. 7.2, also in comparison with data obtained from the Co reference sample at  $\mu_0H = 1.5$  T, which are in agreement with existing literature<sup>160</sup>. Symbols and solid lines represent results from a wavelength-by-wavelength and parameterized MDF analysis, respectively. The Kramers-Kronig consistent MDF for  $\varepsilon_{xy}^{\text{P}}$  consists of two Lorentz oscillators centered at photon energies 0.84 eV and 1.64 eV, which represent the difference in the left- and right circularly polarized light response of the sample. Note that  $\varepsilon_{xy}^{\text{P}}$  differs substantially between F1-STF and a 60 nm Co thin solid reference film.

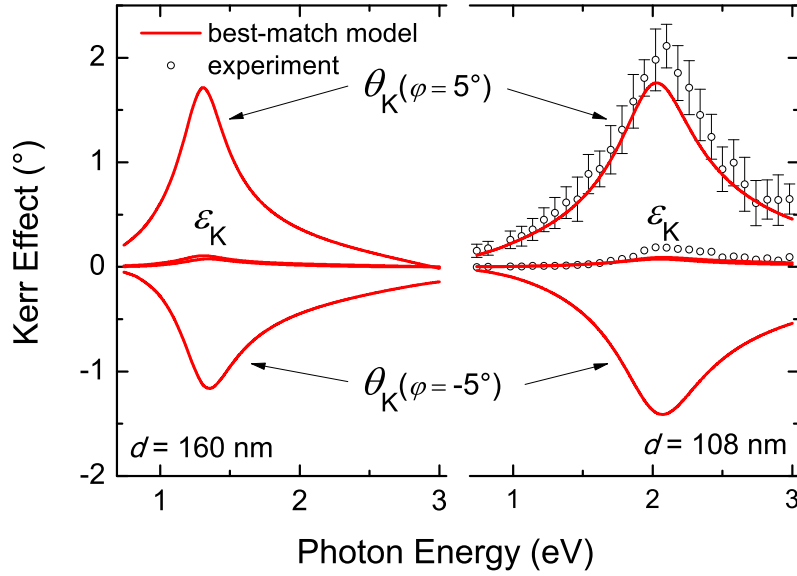
### 7.1.3 Giant Kerr Rotation

Figure 7.3 depicts calculated Kerr rotation  $\theta_K$  and Kerr ellipticity  $\varepsilon_K$  using functions  $\varepsilon_{xy}^P$  (MDF) and experimental data at  $\mu_0 H = 1.8$  T and at  $\Phi_a = 3^\circ$ . The calculated spectra are shown for two different F1-STF thickness values (left and right panel, respectively), as well as for two in-plane orientations  $\varphi$ , where the incident linear polarization is perpendicular to the columns at  $\varphi = 0$ . Peak Kerr rotation values obtained for the Co F1-STF are one order of magnitude larger than those reported for solid Co thin films<sup>161</sup>. These peaks in  $\theta_K$  and  $\varepsilon_K$  are caused by spectral minima in the  $p-p$  polarized reflectance coefficients,  $r_{pp}$ , due to anisotropic interference within the F1-STF. The anisotropic mode coupling described by the symmetric part of  $\varepsilon$  in (3.57) enhances the Kerr effect generated by  $\varepsilon^{MO}$ , and results in well measurable rotation and ellipticity signals. In order to achieve comparable large Kerr rotation values, complex rare-earth metal containing multilayer thin films have been necessary previously<sup>162</sup>. Notably, an azimuthal rotation of  $10^\circ$  causes  $\theta_K$  to alter orientation and has almost no influence on  $\varepsilon_K$ . Maxima in  $\theta_K$  and  $\varepsilon_K$  coincide spectrally for a given thickness and can be shifted conveniently by varying the film thickness over the entire spectral range investigated here. Interestingly, due to the dielectric anisotropy, sample azimuth variations with respect to the incident linear polarization have similar effects on Kerr parameters as a change in the external magnetic field direction.

## 7.2 Longitudinal Kerr Effect Geometry

### 7.2.1 Experiment

Generalized ellipsometry measurements of the Co F1-STF (sample #1) in the longitudinal Kerr effect have been carried out in a similar successive analysis routine as used for the polar Kerr effect discussed above to minimize cross-correlation of varying parameters. Results from the initial step (angle resolver Mueller matrix measurements) are total film thickness  $d = 108.8$  nm, slanting angle  $\theta = 63.5^\circ$ , monoclinic angle  $\beta = 81.6^\circ$  and the anisotropic dielectric function tensor. Subsequently, the sample was transferred to the *polar* magneto-optic Kerr effect setup and spectroscopic Mueller matrix measurements at  $\mu_0 H = 0$  T were analyzed using the model obtained in the first step, in order to determine sample azimuth and angle of incidence parameters. Measurements were then taken with applied external magnetic fields  $\mu_0 H = \pm 1.5$  T. A total of four different in-plane orientations have been measured at  $\varphi = 0^\circ, 45^\circ$ , and  $\pm 135^\circ$ . After rotating the magnet by  $90^\circ$ , measurements in the *longitudinal* geometry



**Figure 7.3:** Experimental (symbols) and calculated (lines) data of Kerr rotation  $\theta_K$  and Kerr ellipticity  $\varepsilon_K$  at  $\mu_0 H = 1.8$  T and  $\Phi_a = 3^\circ$  of a Co F1-STF at two different in-plane orientations  $\varphi$  and thicknesses  $d$ .

have been carried out in the same manner at sample in-plane orientations  $\varphi = \pm 45^\circ$ ,  $\pm 90^\circ$ , and  $\pm 135^\circ$ . In the final step only the wavelength-dependent complex magneto-optic polarizability tensor  $\varepsilon^{\text{MO}}$  was determined by matching the calculated Mueller matrix difference  $\Delta M_{kl} = M_{kl}(-\mu_0 H) - M_{kl}(\mu_0 H)$  with the experiment. All ten different measured scenarios (polar *and* longitudinal) have been included in a best-match multi-sample configuration analysis.

### 7.2.2 Estimation of Magnetization Direction

Figure 7.4 shows experimental data as well as generated MDF data of selected elements of the Mueller matrix difference  $\Delta M_{kl}$  normalized to  $M_{11}$  for the Co F1-STF at an external magnetic field  $\mu_0 H = \pm 1.5$  T along the  $x$ -axis (longitudinal configuration). The two different in-plane orientations ( $\varphi = 273.6^\circ$  and  $\varphi = 93.3^\circ$ ) depict measurement geometries in which the slanted columns are nearly parallel to the plane of incidence and pointing toward the detector and the source, respectively.

Note that the magnitude of Mueller matrix difference spectra is approximately half of what has been measured in the polar geometry (Fig. 7.1), which is in accordance with MOKE observations for thin solid film where the polar measurements are usually much larger than the longitudinal ones<sup>106</sup>.

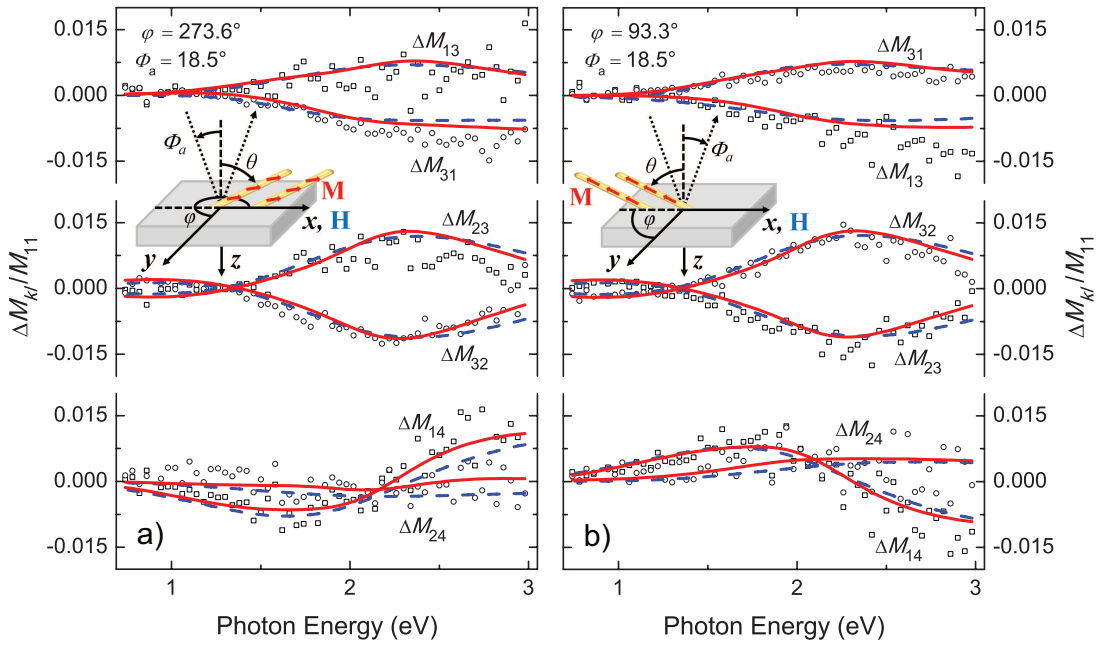


**Figure 7.4:** Experimental (acquired in the longitudinal Kerr geometry; symbols) and best-match model calculated (solid and dashed lines) magnetic field-induced difference data  $\Delta M_{kl} = M_{kl}(\mu_0 H = -1.5 \text{ T}) - M_{kl}(\mu_0 H = 1.5 \text{ T})$  normalized to  $M_{11}$  for two opposite in-plane orientations  $\varphi$  and  $\varphi + 180^\circ$  of the Co F1-STF. The insets schematically depict the respective in-plane orientation  $\varphi$  of the sample, column tilt  $\theta$ , angle of incidence  $\Phi_a$ , magnetic field  $\mathbf{H}$  (longitudinal configuration), and possible sample magnetization  $\mathbf{M}$  directions with respect to the laboratory coordinate frame  $(x, y, z)$ . Best-match model data (blue dashed lines) were calculated with  $\varepsilon_{xy}^P$  only, and the corresponding magnetization  $\mathbf{M}$  is indicated in the inset in a). The model with both  $\varepsilon_{xy}^P$  and  $\varepsilon_{yz}^L$  (red solid lines), as shown in Fig. 7.2, corresponds to the direction of  $\mathbf{M}$  indicated in the inset in b).

Best-match multi-sample configuration model calculations reveal that even in the longitudinal geometry the polar contribution ( $\varepsilon_{xy}^P$ ) is predominant and there is no transverse contribution, i.e.,  $\varepsilon_{xz}^T = 0$ . This is due to the slanted nature of the film and hence the strong magnetic anisotropy. Therefore, an out-of-plane component is present even though a relatively strong ( $\mu_0 H = \pm 1.5 \text{ T}$ ) magnetic field is applied in-plane and parallel to the plane of incidence. Two best-model scenarios are discussed, which both match the experimental data well.

**Model Scenario I ( $\varepsilon_{xy}^P \neq \varepsilon_{xz}^T = \varepsilon_{yz}^L = 0$ ).** Best-match model data in Fig. 7.4 graphed with dashed lines were generated with a polar magneto-optical contribution only,  $\varepsilon_{xy}^P \neq 0$ , and  $\varepsilon_{xz}^T = \varepsilon_{yz}^L = 0$ . However, in order to match experimental data in the longitudinal geometry and at different sample orientations  $\varphi$ , the polar magneto-optical



polarizability has to take the form  $\varepsilon_{xy}^P \cos(72.9^\circ) \sin \varphi$ . The decrease of  $\varepsilon_{xy}^P$  by  $m_z = \cos(72.9^\circ \pm 0.3^\circ) \sin \varphi$  (with respect to  $\varepsilon_{xy}^P$  measured in the polar geometry) might be representative for the magnetization direction (tilted  $72.9^\circ$  away from the substrate normal) at sample orientations parallel to the external magnetic field ( $\varphi = 90^\circ$  and  $270^\circ$ ). This orientation could be close to the easy axis, which was found not to be along the long axis of the nanocolumns but further tilted toward the substrate interface<sup>80,163,164,165,166,167</sup>. Hence, the resulting magnetization direction to a magnetic field in the substrate surface would be tilted away from the column axis by almost  $10^\circ$  as indicated in the inset in Fig. 7.4a. The additional sinusoidal behavior of  $\varepsilon_{xy}^P$  with respect to the in-plane orientation  $\varphi$  is needed to correctly model Mueller matrix elements, for example, at  $\varphi$  and  $\varphi + 180^\circ$  depicted in Fig. 7.4. Hence, the cylindrical symmetry around the  $z$ -axis of  $\varepsilon_{xy}^P$  observed in the polar geometry is not preserved in the longitudinal geometry. Therefore, the polar contribution vanishes completely when the direction of the slanted columns is perpendicular to the plane of incidence. Hence, no magneto-optical polarizability is measured in this particular configuration. Similar observations have been made by Tang *et al.*<sup>20</sup> when measuring MOKE hysteresis loops of comparable Co F1 nanostructures.

**Model Scenario II ( $\varepsilon_{xy}^P \neq \varepsilon_{yz}^L \neq \varepsilon_{xz}^T = 0$ ).** Data in Fig. 7.4 depicted by solid lines are generated with a best-match model where  $\varepsilon^{\text{MO}}$  comprises complex magneto-optic polarizability functions  $\varepsilon_{xy}^P$  and  $\varepsilon_{yz}^L$  ( $\varepsilon_{xz}^T = 0$ ). The consideration of an additional longitudinal component  $\varepsilon_{yz}^L$  improves the match between experiment and model data marginally. As a result, a polar component  $\varepsilon_{xy}^P \cos(65.8^\circ) \sin \varphi$  was determined, which depends on the sample azimuth  $\varphi$  and an orientationally independent longitudinal component  $\varepsilon_{yz}^L$ . Real and imaginary parts of both functions are plotted in Fig. 7.2. The decrease of  $\varepsilon_{xy}^P$  by a factor of  $m_z = \cos(65.8^\circ \pm 1^\circ) \sin \varphi$  indicates that at sample orientations  $\varphi = 90^\circ$  and  $\varphi = 270^\circ$  the magnetization direction is closer to the long axis of the nanocolumns ( $\theta = 63.5^\circ$ ) yet still tilted toward the substrate normal.

**Discussion.** The magneto-optical tensor valid for both model scenarios may be written as

$$\varepsilon^{\text{MO}} = i \begin{pmatrix} 0 & m_z \varepsilon_{xy}^P & -m_y \varepsilon_{xz}^T \\ -m_z \varepsilon_{xy}^P & 0 & m_x \varepsilon_{yz}^L \\ m_y \varepsilon_{xz}^T & -m_x \varepsilon_{yz}^L & 0 \end{pmatrix}, \quad (7.1)$$

where the first scenario is described by  $m_z = \cos(72.9^\circ \pm 0.3^\circ) \sin \varphi$  and  $m_x = m_y = 0$ , and the second by  $m_z = \cos(65.8^\circ \pm 1^\circ) \sin \varphi$ ,  $m_x = 1$ , and  $m_y = 0$ .

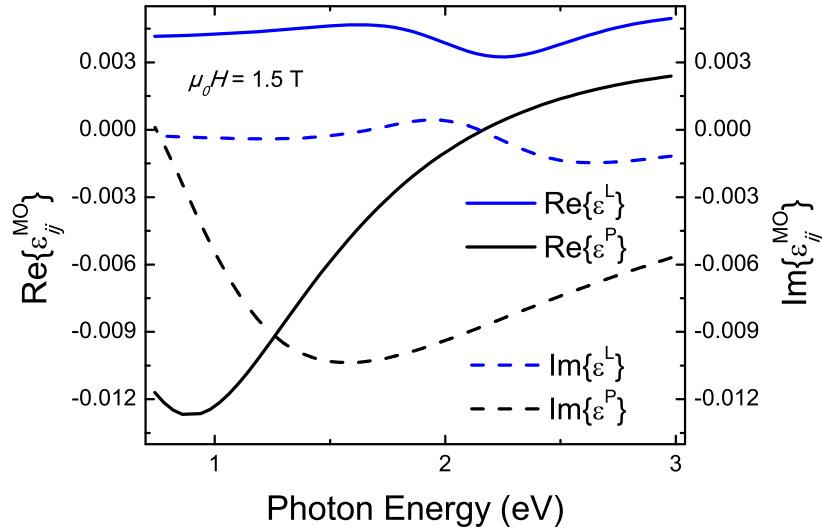


**Figure 7.5:** Real (Re) and imaginary (Im) parts of the best-match model dielectric functions  $\varepsilon_{xy}^P \cos(65.8^\circ)$  and  $\varepsilon_{yz}^L$  from a Co F1-STF ( $\mu_0 H = 1.5$  T).

A comparison between data generated with the two different model scenarios discussed above illustrates the similar results and due to the experimental data noise no scenario can be favored (Fig. 7.4). Hence, two possible magnetization scenarios can be found. The two orientations are determined based on the different scaling factors  $m_z$  of the polar component measured in the longitudinal geometry, i.e., the ratio between  $\varepsilon_{xy}^P$  in the polar and longitudinal configuration, respectively. In order to gain more sensitivity to the longitudinal component, accessibility to larger angles of incidence ( $\Phi_a > 30^\circ$ ) is required. Simulations with both model scenarios discussed above at  $\Phi_a = 35^\circ$  have shown that calculated Mueller matrix difference spectra exhibit significant differences and therefore the correct optical model will be determinable. Furthermore, dynamically controllable external magnetic field directions are desired to unambiguously determine the orientation of the magnetization orientation and to additionally observe magnetic switching behavior.

### 7.3 Octupole Vector-Magnet

The octupole vector magnet is the three-dimensional advancement of existing two-dimensional quadrupole setups used for longitudinal and transverse MOKE<sup>168</sup>. While the quadrupole magnet allows for arbitrary magnetic field directions in the sample surface only, no limitations on the direction of the externally applied magnetic field  $\mathbf{H}$

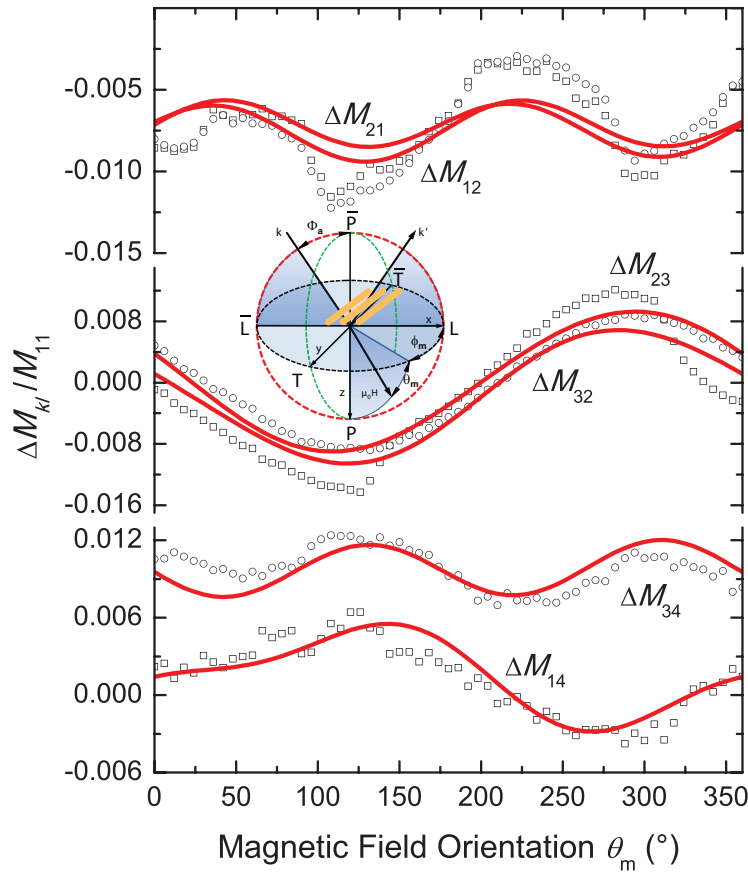


**Figure 7.6:** Experimental (symbols) and best-match model calculated (solid line) LP-VMOGE difference data  $\Delta M_{kl} = M_{kl}(\mu_0 H = 0.39 \text{ T}) - M_{kl}(\mu_0 H = 0 \text{ T})$  normalized to  $M_{11}$  for a Co F1-STF at  $\Phi_a = 45^\circ$  and  $\lambda = 442 \text{ nm}$ . The inset shows the VMOGE definition and depicts the orientation of the slanted columns.

are imposed. Hence,  $\mathbf{H}$  is freely rotatable in space and at the same time a wide range of angles of incidence are accessible due to the particular arrangement of the four solenoid pairs (Fig. 3.13(a)).

### 7.3.1 Experiment

After deposition (similar to sample #1 but 8:30 min growth time), multiple angle of incidence Mueller matrix ellipsometry measurements were carried out on the M2000VI ellipsometer and sample analysis for monoclinic F1-STFs done as discussed in Sect. 6.1.1. Before starting the vector magneto-optical measurements, Mueller matrix data have been recorded for  $\Phi_a = 45^\circ$  within  $400 < \lambda < 1240 \text{ nm}$ . Based on these measurements, initially determined parameters after deposition have been recalculated in a best-match

model calculation procedure to account for variations due to “environmental influences” and variations were in the range of what has been observed for Co F1-STFs when exposed to ambient air (Sect. 6.4.1). The last in-plane orientation was also the final sample position for the VMOGE measurements. The determined sample azimuth  $\varphi = 272.8^\circ$  tells that slanting plane of the Co nanocolumns was rotated mathematically positive by  $2.8^\circ$  away from the plane of incidence. Further best-match parameters from this investigation are total film thickness  $d = 86.5$  nm, slanting angle  $\theta = 63.8^\circ$ , and monoclinic angle  $\beta = 85.1^\circ$ . Subsequently, LP-VMOGE ( $\phi_m = 0^\circ, \theta_m = 0 \dots 360^\circ$ ) Mueller matrix measurements were carried out at a single wavelength 442 nm and  $\Phi_a = 45^\circ$  while the magnetic field vector  $\mathbf{H}$  was rotated on the LP-loop in steps of  $\delta\theta_m = 6^\circ$  with a constant amplitude of  $\mu_0 H = 0.39$  T after each optical measurement. The complex magneto-optic polarizability tensor  $\epsilon^{\text{MO}}$  was determined by matching the calculated Mueller matrix difference  $\Delta M_{kl} = M_{kl}(\mu_0 H) - M_{kl}(\mu_0 H = 0 \text{ T})$  for all orientations of  $\mathbf{H}$  with the experiment.

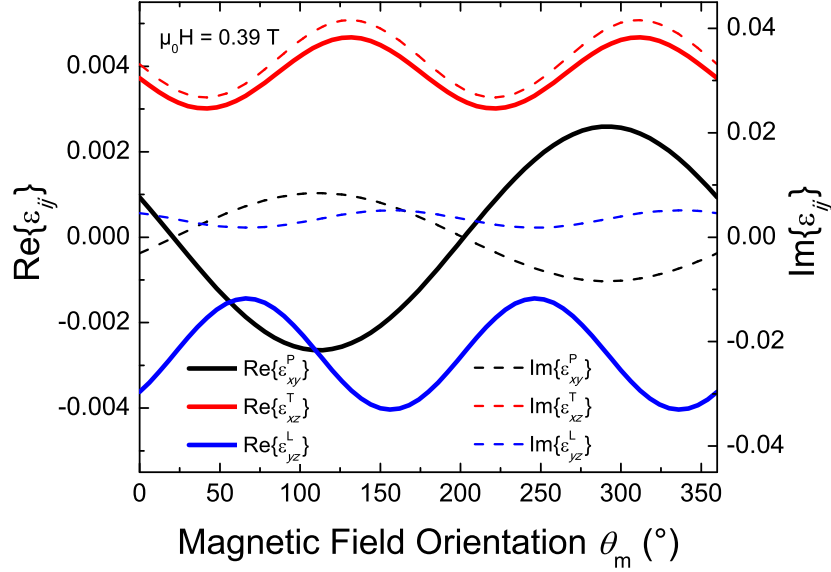
### 7.3.2 Results

Figure 7.6 shows experimental data as well as generated data of selected elements of the Mueller matrix difference  $\Delta M_{kl}$  normalized to  $M_{11}$  at  $\lambda = 442$  nm for a Co F1-STF with respect to the magnetic field orientation  $\theta_m$ . All depicted elements are, apart from small deviations, periodic functions and elements  $\Delta M_{12}$ ,  $\Delta M_{21}$ , and  $\Delta M_{34}$  show a period of  $180^\circ$  whereas the other depicted elements exhibit a period of  $360^\circ$ . In order to match the magnetic field orientation dependent data, in first approximation simple cosine and sine dependencies of the sample magnetization were assumed. The experimental data can be matched with model calculations, if certain directional dependencies of the magneto-optical functions  $\epsilon_{ij}^{\text{MO}}$  were assumed. Even though the external magnetic field is only rotating in the  $xz$ -plane, which is also the slanting plane of the columns, all three magneto-optical polarizabilities are needed to match experimental data. Hence, the empirically determined magneto-optical permittivity tensor takes the form of (7.1) with

$$m_x = \cos(\theta_m - \theta_{x0}) \sin(\theta_m - \theta_{x0}) + m_{x0}, \quad (7.2a)$$

$$m_y = \cos(\theta_m - \theta_{y0}) \sin(\theta_m - \theta_{y0}) + m_{y0}, \quad (7.2b)$$

$$m_z = \cos(\theta_m - \theta_{z0}) + m_{z0}, \quad (7.2c)$$



**Figure 7.7:** Real (Re) and imaginary (Im) parts of the best-match model magneto-optical polarizabilities  $\varepsilon_{xy}^P m_z$ ,  $\varepsilon_{xz}^T m_y$ , and  $\varepsilon_{yz}^L m_x$  from a Co F1-STF ( $\mu_0 H = 0.39$  T) determined at a single wavelength 442 nm.

such that the polar magneto-optical component is proportional to the cosine of the magnetic field direction ( $\varepsilon_{xy}^P \propto \cos$ ). Longitudinal and transversal magneto-optical components exhibit more complex proportionalities to the magnetic field direction ( $\varepsilon_{yz}^L \propto \text{cossin}$ ,  $\varepsilon_{xz}^T \propto \text{cossin}$ ), and which are needed to match the  $180^\circ$  period of certain Mueller matrix elements. Additional parameters  $\theta_{j0}$  and  $m_{j0}$  with  $j = x, y, z$  were needed to offset the periodic function, however,  $\theta_{x0} = \theta_{z0}$  and  $m_{x0} = 0$ . Real and imaginary parts of the complete magneto-optical permittivity tensor are depicted in Fig. 7.7.

Further analysis of VMOGE measurements has yet to be done and results presented here should be considered as outlook and highlight the potential of VMOGE with respect to the determination of the full dielectric tensor and dynamic magnetization switching behavior in complex STFs.

## 7.4 Summary

- The quantified polar magneto-optical polarizability component for ferromagnetic Co F1-STFs is two orders of magnitude larger than for Co solid thin films. Furthermore, Co F1-STFs exhibit a highly anisotropic polar Kerr effect with peak

Kerr rotations at near normal incidence one order of magnitude larger than what has been reported for solid Co thin films.

- A large polar magneto-optical polarizability component depending on the sample azimuth can be measured even though a relatively strong magnetic field ( $\mu_0 H = \pm 1.5$  T) is applied in the sample surface and parallel to the plane of incidence (traditional longitudinal Kerr geometry). This reveals that the sample magnetization is not parallel to the externally applied magnetic field. Based on the ratio of the polar magneto-optical polarizability component measured in polar and longitudinal geometry, the sample magnetization direction can be estimated.
- Vector-magneto-optical generalized ellipsometry measurements reveal a strong directional dependence of the magneto-optical functions on the externally applied magnetic field. Empirical sine and cosine dependencies have been found which describe the experimental data.

## 7.5 Literature Discussion

Physical properties of materials with decreasing structure size are becoming more sensitive to the particular geometry of the system. Ferromagnetic materials with structure sizes in the nanometer regime, for example, possess interesting magnetic properties, significantly different from bulk, due to the increasing influence of surface and domain confinement effects<sup>169,170</sup>.

Driven by the need for new memory storage units for high-speed computational devices, it was recognized that ferromagnetic F1-STFs exhibit strong magnetic uniaxial anisotropy with the axis of easy magnetization normal to the direction of the metal vapor stream<sup>171,172</sup>. Further investigation showed that the dependence of the easy axis on the direction of the particle flux is only valid for deposition angles  $\theta_i < 50^\circ$ . With increasing  $\theta_i$ , therefore increasing column tilt as well as void fraction, the easy axis starts to rotate toward the substrate interface<sup>80,163,164,165,166,167,173</sup>.

Magneto-optical investigations on slanted columnar thin films have shown that also the Kerr effect, the change of an incident linear polarization state upon reflection due to sample magnetization, strongly depends on the sample in-plane rotation and F1-STFs were proposed to be potential candidates for magneto-optical recording<sup>20,174,175</sup>. In general, ferromagnetic STFs could be particularly interesting for future magneto-optical applications since anisotropic magnetic and optical properties may be tailored at the same time<sup>45,176</sup>. Due to relatively small and anisotropic extinction coefficients, high

penetration depths can be achieved in metal F1-STFs for electromagnetic radiation at visible wavelengths. In contrast to highly absorbing solid metal thin films, the magnetic field-induced birefringence is no longer probed only at the near surface. Therefore, such ferromagnetic nanostructures may be interesting not only for magneto-optical data storage but also for thin film low-loss transmission magneto-optical modulators, for example.

## Chapter 8

### Summary and Outlook

*Glancing angle deposition* was presented as an advanced physical vapor deposition technique capable of bottom-up fabrication of three-dimensionally shaped, highly spatially coherent nanostructures. Paired with a dynamic substrate motion, this technique allows for engineering self-assembled, self-organized highly spatially coherent achiral and chiral *sculptured thin films*. Detailed descriptions of the in-house built ultrahigh vacuum deposition chamber and peripheral equipment are provided. A new nomenclature scheme has been proposed based on basic building blocks to unambiguously identify sculptured thin film geometries by their name.

*Spectroscopic generalized ellipsometry* in the visible and near-infrared spectral region was demonstrated to be a highly suitable, non-destructive tool for investigation of low-symmetry and highly anisotropic absorbing sculptured thin films. The intrinsic polarizabilities inherent to the biaxial nanostructured materials examined here have been determined for a series of different metal sculptured thin film geometries and effective principal optical constants are reported. Strong optical birefringence and dichroism are quantified for different sculptured thin film samples, and the complex-valued dielectric function tensor differs significantly from the respective bulk material. In particular, achiral metal slanted columnar thin films (F1-STFs) are found *monoclinic* due to dielectric polarization charge coupling effects across neighboring slanted but electrically isolated nanocolumns. The validity of the homogeneous biaxial layer approach applied to model the anisotropic electromagnetic plane wave response of metal F1-STFs was discussed for F1-STFs from three different materials: cobalt, titanium and supermalloy ( $\text{Ni}_{80}\text{Fe}_{15}\text{Mo}_5$ ). Physical properties such as birefringence, dichroism, and monoclinicity, for example, are found to be common amongst all F1-STFs discussed here (*universality*).

For the first time, accurate sets of optical constants for complex manifold and helical sculptured thin films are presented. It is found that complex sculptured thin films may be considered cascaded F1-STFs building blocks and can be optically approximated as



a stratified medium comprising F1-STFs with different slanting orientations. Therefore, once the building blocks are characterized the anisotropic polarization response of complex layered sculptured thin films can be predicted by a modular conception. The piecewise homogeneous layer approach enables modular assembly of F1-STF building blocks thereby creating an optical model that mimics the true geometry of the sculptured thin film. The *modularity* was exemplarily discussed for a total of six different sculptured thin film geometries from cobalt and titanium.

Variations in the host medium have been discussed, and birefringence and dichroism changes observed upon hybridization by partially filling void spaces with the hole conducting polymer P3DDT. Since STF layers are very fragile and might need to be embedded in a resin to prevent damage due to environmental influences (dust, humidity, mechanical stress, etc.), knowledge of device optical properties after passivation are desired. Investigations presented here suggest that the polarization response of a device stack can be determined and the anisotropic properties are preserved upon polymer infiltration.

It has been shown that structural properties including void fractions of F1-STFs determined with the anisotropic Bruggemann effective medium approximation may serve as good estimates. However, the optical constants deviate from those determined with the homogeneous biaxial layer approach with monoclinic arrangement. Based on existing literature and investigations presented in this thesis an empirically found order of depolarization factors is presented ( $L_a^D > L_b^D > L_c^D \neq 0$ ), which is in accordance with the shape of the columns (ellipsoids).

Room-temperature magneto-optical generalized ellipsometry on ferromagnetic Co F1-STFs in the visible and near-infrared wavelength region are presented. For the first time, the magneto-optical polarizability in such highly anisotropic sculptured thin films is quantified in the traditional polar Kerr geometry and cylindrical symmetry observed of the magnetic field-induced off-diagonal part of the dielectric tensor. In contrast, due to intrinsic dielectric anisotropy a highly anisotropic Kerr effect was calculated and observed by variations of the in-plane orientation, and which produces *giant Kerr rotation* angles. Combined analysis of measurements taken in the polar and longitudinal Kerr geometry led to estimates of the resulting sample magnetization due to an externally applied magnetic field.

The concept of *vector-magneto-optical generalized ellipsometry* was introduced and initial investigations are discussed. The octupole vector magnet allows for freely rotatable external magnetic fields and measurements of a single loop have revealed interesting dynamics.

With the findings presented in this work it is now possible to predict optical and magneto-optical properties of sculptured thin films with arbitrary geometry. This will allow for engineering desired anisotropic physical properties of three-dimensionally nanostructured thin films and pave the way for next generation micro- and nanosystems, especially with respect to the exploitation of nanohybrid functional materials for novel detection principles.

Ferromagnetic sculptured thin films are potential candidates for nanomagnetic memory and logic devices, magneto-optical modulators, and magneto-optical storage devices. Here, great potential for the vector-magneto-optical generalized ellipsometry setup is foreseen because with arbitrarily rotatable external magnetic fields and access to a wider range of incident angles, this novel instrument combination will be capable of measuring the dynamic magnetization properties of highly anisotropic magnetic nanostructures.

## References

- [1] O. Toader and S. John, *Science* **292**, 1133 (2001). [1](#)
- [2] J. P. Singh, D.-L. Li, D.-X. Ye, R. C. Picu, T.-M. Lu, and G.-C. Wang, *Appl. Phys. Lett.* **84**, 3657 (2004). [1](#)
- [3] M. T. Umlor, *Appl. Phys. Lett.* **87**, 082505 (2005). [1](#)
- [4] D. J. Bell, J. Dong, Y. Sun, L. Zhang, B. J. Nelson, and D. Grützmacher, in *Proc. 5th IEEE Conf. Nanotechnol.* (IEEE, Nagoya, Japan, 2005), p. 15. [1](#)
- [5] S. V. Kesapragada, P. Victor, O. Nalamasu, and D. Gall, *Nano Lett.* **6**, 854 (2006). [1](#)
- [6] J. J. Steele, A. C. van Popta, M. M. Hawkeye, J. C. Sit, and M. J. Brett, *Sensor Actuat. B-Chem.* **120**, 213 (2006). [1](#), [7](#), [87](#)
- [7] J. A. Dobrowolski, D. Poitras, P. Ma, H. Vakil, and M. Acree, *Appl. Optics* **41**, 3075 (2002). [1](#)
- [8] D. Poitras and J. A. Dobrowolski, *Appl. Optics* **43**, 1286 (2004). [1](#)
- [9] J.-Q. Xi, M. Ojha, J. L. Plawsky, W. N. Gill, J. K. Kim, and E. F. Schubert, *Appl. Phys. Lett.* **87**, 031111 (2005). [1](#)
- [10] J.-Q. Xi, M. Ojha, W. Cho, J. L. Plawsky, W. N. Gill, T. Gessmann, and E. F. Schubert, *Opt. Lett.* **30**, 1518 (2005). [1](#)
- [11] S.-T. Ho, S. L. McCall, R. E. Slusher, L. N. Pfeiffer, K. W. West, A. F. J. Levi, G. E. Blonder, and J. L. Jewell, *Appl. Phys. Lett.* **57**, 1387 (1990). [1](#)
- [12] R. Sharma, E. D. Haberer, C. Meier, E. L. Hu, and S. Nakamura, *Appl. Phys. Lett.* **87**, 051107 (2005). [1](#)
- [13] Q. Xu, V. R. Almeida, R. R. Panepucci, and M. Lipson, *Opt. Lett.* **29**, 1626 (2004). [2](#)

- 
- [14] J. K. Kim, T. Gessmann, E. F. Schubert, J.-Q. Xi, H. Luo, J. Cho, C. Sone, and Y. Park, *Appl. Phys. Lett.* **88**, 013501 (2006). [2](#)
- [15] A. Jain, S. Rogojevic, S. Ponoth, N. Agarwal, I. Matthew, W. N. Gill, P. Persans, M. Tomozawa, J. L. Plawsky, and E. Simonyi, *Thin Solid Films* **398-399**, 513 (2001). [2](#)
- [16] G. K. Kiema, M. J. Colgan, and M. J. Brett, *Sol. Energ. Mat. Sol. C.* **85**, 321 (2005). [2](#)
- [17] J. Bouclé, P. Ravirajan, and J. Nelson, *J. Mater. Chem.* **17**, 3141 (2007). [2](#), [92](#)
- [18] H.-Y. Yang, M.-F. Lee, C.-H. Huang, Y.-S. Lo, Y.-J. Chen, and M.-S. Wong, *Thin Solid Films* **518**, 1590 (2009). [2](#)
- [19] M. D. Fleischauer, J. Li, and M. J. Brett, *J. Electrochem. Soc.* **156**, A33 (2009). [2](#)
- [20] F. Tang, D.-L. Liu, D.-X. Ye, T.-M. Lu, and G.-C. Wang, *J. Mag. Mag. Mat.* **283**, 65 (2004). [2](#), [107](#), [112](#)
- [21] E. Schubert, *CAREER: Chiral Nanostructure Hybrid Materials for Applications in Terahertz Resonator and Magnetic Storage Devices*, ECCS-0846329, National Science Foundation Award (2009-2014). [2](#)
- [22] F. F. Choobineh, *RII Project: Nanohybrid Materials & Algal Biology*, EPS-1004094, National Science Foundation Award (2010-2015). [2](#)
- [23] <http://en.wikipedia.org/wiki/Capsid>, November 10, 2010. [2](#)
- [24] T. D. Goddard, C. C. Huang, and T. E. Ferrin, *Structure* **13**, 473 (2005). [2](#)
- [25] A. Kundt, *Ann. Phys.* **263**, 59 (1886). [5](#), [34](#), [97](#)
- [26] H. König and G. Helwig, *Optik* **6**, 111 (1950). [5](#)
- [27] A. Lakhtakia and R. Messier, *Sculptured Thin Films: Nanoengineered Morphology and Optics* (SPIE Press, Bellingham, 2005). [5](#), [7](#), [13](#), [37](#), [99](#)
- [28] M. M. Hawkeye and M. J. Brett, *J. Vac. Sci. Technol. A* **25**, 1317 (2007). [5](#), [7](#)
- [29] N. O. Young and J. Kowal, *Nature* **183**, 104 (1959). [5](#), [99](#)
- [30] B. Goldstein and L. Pensak, *J. Appl. Phys.* **30**, 155 (1959). [6](#)

- 
- [31] J. M. Nieuwenhuizen and H. B. Haanstra, *Philips Tech. Rev.* **27**, 87 (1966). [6](#), [58](#)
- [32] K. Robbie, L. J. Friedrich, S. K. Dew, T. Smy, and M. J. Brett, *J. Vac. Sci. Technol. A* **13**, 1032 (1995). [6](#)
- [33] K. Robbie, M. J. Brett, and A. Lakhtakia, *J. Vac. Sci. Technol. A* **13**, 2991 (1995). [6](#)
- [34] K. Kaminska, T. Brown, G. Beydaghyan, and K. Robbie, *Appl. Optics* **42**, 4212 (2003). [7](#)
- [35] B. Dick, M. J. Brett, and T. Smy, *J. Vac. Sci. Technol. B* **21**, 23 (2003). [7](#)
- [36] E. Schubert, F. Frost, H. Neumann, B. Rauschenbach, B. Fuhrmann, F. Heyroth, J. Rivory, E. Charron, B. Gallas, and M. Schubert, *Adv. Solid State Phys.* **46**, 309 (2007). [7](#)
- [37] F. Tang, T. Karabacak, L. Li, M. Pelliccione, G.-C. Wang, and T.-M. Lu, *J. Vac. Sci. Technol. A* **25**, 160 (2007). [7](#)
- [38] D. Vick, Y. Y. Tsui, M. J. Brett, and R. Fedosejevs, *Thin Solid Films* **350**, 49 (1999). [7](#)
- [39] K. Robbie, J. C. Sit, and M. J. Brett, *J. Vac. Sci. Technol. B* **16**, 1115 (1998). [7](#)
- [40] K. Robbie, G. Beydaghyan, T. Brown, C. Dean, J. Adams, and C. Buzea, *Rev. Sci. Instrum.* **75**, 1089 (2004). [7](#), [9](#)
- [41] T. Karabacak, G.-C. Wang, and T.-M. Lu, *J. Appl. Phys.* **94**, 7723 (2003). [7](#)
- [42] T. Karabacak, G.-C. Wang, and T.-M. Lu, *J. Vac. Sci. Technol. A* **22**, 1778 (2004). [7](#)
- [43] M. O. Jensen and M. J. Brett, *IEEE T. Nanotechnol.* **4**, 269 (2005). [7](#)
- [44] M. Malac, R. F. Egerton, M. J. Brett, and B. Dick, *J. Vac. Sci. Technol. B* **17**, 2671 (1999). [7](#)
- [45] B. Dick, M. J. Brett, T. J. Smy, M. R. Freeman, M. Malac, and R. F. Egerton, *J. Vac. Sci. Technol. A* **18**, 1838 (2000). [7](#), [59](#), [112](#)

- 
- [46] E. Schubert, T. Höche, F. Frost, and B. Rauschenbach, *Appl. Phys. A-Mater.* **81**, 481 (2005). [7](#)
- [47] M. A. Summers and M. J. Brett, *Nanotechnology* **19**, 415203 (2008). [7](#), [55](#), [94](#)
- [48] Y. P. Zhao, D. X. Ye, G. C. Wang, and T. M. Lu, *Nano Lett.* **2**, 351 (2002). [7](#)
- [49] R. Glass, M. Möller, and J. P. Spatz, *Nanotechnology* **14**, 1153 (2003). [7](#), [9](#), [57](#)
- [50] R. Glass, M. Arnold, E. A. Cavalcanti-Adam, J. Blümmel, C. Haferkemper, C. Dodd, and J. P. Spatz, *New J. Phys.* **6**, 101 (2004). [7](#), [9](#), [57](#)
- [51] C. Patzig, B. Rauschenbach, B. Fuhrmann, and H. S. Leipner, *J. Appl. Phys.* **103**, 024313 (2008). [7](#)
- [52] C. Patzig, B. Rauschenbach, B. Fuhrmann, and H. S. Leipner, *J. Nanosci. Nanotechnol.* **9**, 1985 (2009). [7](#)
- [53] L. Chi, ed., *Nanostructured Surfaces*, vol. 8 of *Nanotechnology* (Wiley-VCH, Weinheim, 2010). [7](#), [9](#)
- [54] B. N. Mbenkum, *On the Anomalies in Gold Nanoparticles Prepared by Micelle Nanolithography and Their Impact on One-Dimensional Material Synthesis Role of Substrate, Size Effects and Impurity*, Ph.D. thesis, Ruperto-Carola University of Heidelberg (2007). [9](#), [57](#)
- [55] G. Sauerbrey, *Z. Phys. A-Hadron Nucl.* **155**, 206 (1959). [16](#)
- [56] C. Lu and O. Lewis, *J. Appl. Phys.* **43**, 4385 (1972). [16](#)
- [57] J. I. Goldstein, D. E. Newbury, P. Echlin, D. C. Joy, C. E. Lyman, E. Lifshin, L. Sawyer, and J. R. Michael, *Scanning Electron Microscopy and X-ray Microanalysis* (Springer, New York, 2003), 3rd ed. [17](#)
- [58] T. E. Everhart and R. F. M. Thornley, *J. Sci. Instrum.* **37**, 246 (1960). [17](#)
- [59] B. E. Warren, *X-ray Diffraction* (Dover Publications, Mineola, 1990). [19](#)
- [60] R. M. A. Azzam and N. M. Bashara, *Ellipsometry and Polarized Light* (North-Holland Publ. Co., Amsterdam, 1984). [19](#), [21](#), [22](#), [31](#), [39](#)
- [61] D. Kliger, J. Lewis, and C. Randall, *Polarized Light in Optics and Spectroscopy* (Academic Press, New York, 1990). [19](#)

- [62] H. G. Tompkins, *A User's Guide to Ellipsometry* (Academic Press, New York, 1993). [19](#)
- [63] H. G. Tompkins and E. A. Irene, eds., *Handbook of Ellipsometry* (William Andrew Publishing, Norwich, 2005). [19](#), [41](#), [43](#)
- [64] H. Fujiwara, *Spectroscopic Ellipsometry: Principles and Applications* (Wiley, Chichester, 2007). [19](#), [22](#), [37](#), [43](#)
- [65] M. Schubert, in *Handbook of Ellipsometry*, edited by E. A. Irene and H. G. Tompkins (William Andrew Publishing, Norwich, 2005). [21](#), [24](#), [32](#)
- [66] P. Yeh, *Optical Waves in Layered Media* (Wiley, New York, 1988). [21](#), [31](#)
- [67] M. Schubert, *Infrared Ellipsometry on Semiconductor Layer Structures: Phonons, Plasmons, and Polaritons*, vol. 209 of *Springer Tracts in Modern Physics* (Springer, Berlin, 2004). [21](#), [27](#), [31](#), [32](#), [41](#)
- [68] M. Schubert, *Thin Solid Films* **313-314**, 323 (1998). [21](#), [39](#)
- [69] A. Röseler, *Infrared Spectroscopic Ellipsometry* (Akademie-Verlag, Berlin, 1990). [22](#)
- [70] D. Goldstein, *Polarized Light* (Marcel Dekker, New York, 2003), 2nd ed. [22](#), [25](#), [30](#)
- [71] G. E. Jellison and F. A. Modine, *Appl. Optics* **36**, 8184 (1998). [22](#)
- [72] G. E. Jellison and F. A. Modine, *Appl. Optics* **36**, 8190 (1998). [22](#)
- [73] G. E. Jellison, in *Handbook of Ellipsometry*, edited by E. A. Irene and H. G. Tompkins (William Andrew Publishing, Norwich, 2005). [22](#), [23](#)
- [74] W. S. Weiglhofer, in *Introduction to Complex Mediums for Optics and Electromagnetics*, edited by W. S. Weiglhofer and A. Lakhtakia (SPIE Press, Bellingham, 2003). [25](#)
- [75] M. de Graef and M. E. McHenry, *Structure of Materials: An Introduction to Crystallography, Diffraction, and Symmetry* (Cambridge University Press, Cambridge, 2007). [28](#)
- [76] J. A. Woollam Co., Inc., *Guide to Using WVASE32<sup>®</sup>: Spectroscopic Ellipsometry Data Acquisition and Analysis Software* (2008). [28](#), [44](#)

- 
- [77] M. Born and E. Wolf, *Principles of Optics* (Cambridge University Press, Cambridge, 2003), 7th ed. [30](#)
- [78] D. W. Berreman, *J. Opt. Soc. Am.* **62**, 502 (1972). [31](#)
- [79] M. Schubert, *Phys. Rev. B* **53**, 4265 (1996). [31](#), [32](#), [38](#), [39](#)
- [80] M. S. Cohen, *J. Appl. Phys.* **32**, S87 (1961). [34](#), [107](#), [112](#)
- [81] I. J. Hodgkinson and Q. H. Wu, *Birefringent Thin Films and Polarizing Elements* (World Scientific, Singapore, 1997). [34](#), [36](#), [37](#), [94](#), [98](#)
- [82] L. I. Epstein, *J. Opt. Soc. Am.* **42**, 806 (1952). [34](#)
- [83] D. A. G. Bruggeman, *Ann. Physik (Leipzig)* **24**, 636 (1953). [35](#), [36](#), [37](#), [93](#)
- [84] O. Wiener, *Abh. Sächs. Ges. Akad. Wiss., Math.-Phys. Kl.* **32**, 509 (1912). [37](#)
- [85] W. L. Bragg and A. B. Pippard, *Act. Cryst.* **6**, 865 (1953). [37](#)
- [86] H. K. Pulker and E. Jung, *Thin Solid Films* **7**, 57 (1971). [37](#)
- [87] A. Shivola, *Electromagnetic mixing formulas and applications*, vol. 47 of *Electromagnetic Waves* (The Institution of Electrical Engineers, London, 1999). [37](#), [98](#), [99](#)
- [88] D. E. Aspnes, *Thin Solid Films* **89**, 249 (1982). [37](#)
- [89] N. J. Podraza, C. Chen, I. An, G. M. Ferreira, P. I. Rovira, R. Messier, and R. W. Collins, *Thin Solid Films* **455-456**, 571 (2004). [37](#), [98](#), [99](#)
- [90] M. Schubert, B. Rheinländer, C. Cramer, H. Schmiedel, J. A. Woollam, C. M. Herzinger, and B. Johs, *J. Opt. Soc. Am. A* **13**, 1930 (1996). [38](#)
- [91] M. Schubert and C. M. Herzinger, *Phys. Status Solidi (a)* **188**, 1563 (2001). [38](#)
- [92] W. H. Press, B. P. Flannery, S. A. Teukolsky, and W. T. Vetterling, *Numerical Recipes: The Art of Scientific Computing* (Cambridge University Press, Cambridge, 1988). [41](#)
- [93] C. M. Herzinger, P. G. Snyder, B. Johs, and J. A. Woollam, *J. Appl. Phys.* **77**, 1715 (1995). [41](#)



- 
- [94] C. M. Herzinger, H. Yao, P. G. Snyder, F. G. Celii, Y.-C. Kao, B. Johs, and J. A. Woollam, *J. Appl. Phys.* **77**, 4677 (1995). [41](#)
- [95] B. Johs, *Thin Solid Films* **234**, 395 (1993). [42](#)
- [96] A. Berger and M. R. Pufall, *Appl. Phys. Lett.* **71**, 965 (1997). [44](#), [101](#)
- [97] M. Schubert, T. E. Tiwald, and J. A. Woollam, *Appl. Optics* **38**, 177 (1999). [44](#), [47](#), [101](#)
- [98] L. D. Landau, L. P. Pitaevskii, and E. M. Lifshitz, *Electrodynamics of continuous media* (Elsevier, Oxford, 2004), 2nd ed. [45](#)
- [99] Š. Višňovský, *Czech. J. Phys. B* **36**, 625 (1986). [45](#)
- [100] M. Mansuripur, *The Physical Principles of Magneto-Optical Recording* (University Press, Cambridge, 1995). [45](#), [49](#)
- [101] K. Shinagawa, in *Magneto-Optics*, edited by S. Sugamo and N. Kojima (Springer, New York, 2000). [45](#)
- [102] R. J. Potton, *Rep. Prog. Phys.* **67**, 717 (2004). [46](#)
- [103] É. du Trémolet de LaCheisserie, D. Gignoux, and M. Schlenker, eds., *Magnetism: Fundamentals* (Springer, New York, 2005). [46](#)
- [104] W. A. McGahan, P. He, J. A. Woollam, and F. O. Sequeda, *Appl. Phys. Commun.* **11**, 375 (1992). [47](#)
- [105] M. Schubert, T. Hofmann, and C. M. Herzinger, *J. Opt. Soc. Am. A* **20**, 347 (2003). [47](#), [99](#)
- [106] S. D. Bader, *J. Mag. Mag. Mat.* **100**, 440 (1991). [49](#), [105](#)
- [107] K. Mok and H. Schmidt, *Vector-magneto-optical generalized ellipsometry*, unpublished. [50](#)
- [108] C. Müller, T. A. M. Ferenczi, M. Campoy-Quiles, J. M. Frost, D. D. C. Bradley, P. Smith, N. Stingelin-Stutzmann, and J. Nelson, *Adv. Mater.* **20**, 3510 (2008). [53](#), [91](#)
- [109] M. O. Jensen and M. J. Brett, *Appl. Phys. A* **80**, 763 (2004). [55](#)
- [110] R. N. Tait, T. Smy, and M. J. Brett, *Thin Solid Films* **226**, 196 (1993). [58](#), [60](#)

- 
- [111] D. X. Ye, Y. P. Zhao, G. R. Yang, Y. G. Zhao, G. C. Wang, and T. M. Lu, *Nanotechnology* **13**, 615 (2002). [58](#)
- [112] S. Lichter and J. Chen, *Phys. Rev. Lett.* **56**, 1396 (1986). [58](#)
- [113] K. Hara, M. Kamiya, T. Hashimoto, K. Okamoto, and H. Fujiwara, *J. Mag. Mag. Mat.* **73**, 161 (1988). [58](#)
- [114] F. Liu, C. Yu, L. Shen, J. A. Barnard, and G. J. Mankey, *IEEE T. Magn.* **36**, 2939 (2000). [59](#)
- [115] Y. Henry, K. Ounadjela, L. Piraux, S. Dubois, J.-M. George, and J.-L. Duvail, *Eur. Phys. J. B* **20**, 35 (2001). [59](#)
- [116] M. Darques, L. Piraux, A. Encinas, P. Bayle-Guillemaud, A. Popa, and U. Ebels, *Appl. Phys. Lett.* **86**, 072508 (2005). [59](#)
- [117] E. D. Palik, ed., *Handbook of Optical Constants of Solids* (Academic Press, Boston, 1991). [64](#), [69](#), [70](#), [93](#), [95](#)
- [118] D. W. Lynch, C. G. Olson, and J. H. Weaver, *Phys. Rev. B* **11**, 3617 (1975). [69](#), [75](#)
- [119] J. J. Steele, J. P. Gospodyn, J. C. Sit, and M. J. Brett, *IEEE Sens. J.* **6**, 24 (2006). [87](#)
- [120] M. M. Hawkeye, K. M. Krause, and M. J. Brett, *Proc. of SPIE* **7356**, 73560G (2009). [87](#)
- [121] G. B. Smith, *Opt. Commun.* **71**, 279 (1989). [93](#)
- [122] G. W. Mbise, G. A. Niklasson, C. G. Granqvist, and S. Palmer, *J. Appl. Phys.* **80**, 5361 (1996). [94](#), [98](#)
- [123] G. W. Mbise, D. L. Bellac, G. A. Niklasson, and C. G. Granqvist, *J. Phys. D: Appl. Phys.* **30**, 2103 (1997). [94](#), [98](#)
- [124] D. O. Smith, M. S. Cohen, and G. P. Weiss, *J. Appl. Phys.* **31**, 1755 (1960). [97](#)
- [125] R. J. King and S. P. Talim, *Opt. Acta* **28**, 1107 (1981). [98](#)
- [126] I. Hodgkinson, F. Horowitz, H. A. Macleod, M. Sikkens, and J. J. Wharton, *J. Opt. Soc. Am. A* **2**, 1693 (1985). [98](#)

- 
- [127] I. Hodgkinson, Q. H. Wu, and J. Hazel, *Appl. Optics* **37**, 2653 (1998). [98](#)
- [128] I. Hodgkinson and Q. H. Wu, *Appl. Optics* **38**, 3621 (1999). [98](#)
- [129] R. A. May, D. W. Flaherty, C. B. Mullins, and K. J. Stevenson, *J. Phys. Chem. Lett.* **1**, 1264 (2010). [98](#), [100](#)
- [130] K. Y. Bang, E. H. Choi, J. S. Kyung, I. An, S.-H. Woo, Y. J. Park, and C. K. Hwangbo, *J. Korean Phys. Soc.* **46**, 137 (2005). [98](#)
- [131] G. Beydaghyan, K. Kaminska, T. Brown, and K. Robbie, *Appl. Optics* **43**, 5343 (2004). [98](#)
- [132] K. Kaminska, A. Amassian, L. Martinu, and K. Robbie, *J. Appl. Phys.* **97**, 013511 (2005). [98](#)
- [133] J. Gospodyn and J. C. Sit, *Opt. Mater.* **29**, 318 (2006). [98](#)
- [134] S.-H. Hsu, E.-S. Liu, Y.-C. Chang, J. N. Hilfiker, Y. D. Kim, T. J. Kim, C.-J. Lin, and G.-R. Lin, *Phys. Status Solidi (a)* **205**, 876 (2008). [98](#)
- [135] G. Beydaghyan, C. Buzea, Y. Chi, C. Elliott, and K. Robbie, *Appl. Phys. Lett.* **87**, 153103 (2005). [98](#)
- [136] M. Mansour, A.-S. Keita, B. Gallas, J. Rivory, A. Besnard, and N. Martin, *Opt. Mater.* **32**, 1146 (2010). [98](#)
- [137] T. Motohiro and Y. Yaga, *Appl. Optics* **28**, 2466 (1989). [99](#)
- [138] J. C. M. Garnett, *Phil. Trans. Soc. Lond. A* **203**, 385 (1904). [99](#)
- [139] S. Linden, C. Enkrich, M. Wegener, J. Zhou, T. Koschny, and C. M. Soukoulis, *Science* **306**, 1351 (2004). [99](#)
- [140] C. Rockstuhl, F. Lederer, C. Etrich, T. Zentgraf, J. Kuhl, and H. Giessen, *Opt. Express* **14**, 8827 (2006). [99](#)
- [141] C. Rockstuhl, T. Zentgraf, E. Pshenay-Severin, J. Petschulat, A. Chipouline, J. Kuhl, T. Pertsch, H. Giessen, and F. Lederer, *Opt. Express* **15**, 8871 (2007). [99](#)
- [142] R. Abdeddaïm, G. Guida, A. Priou, B. Gallas, and J. Rivory, *Appl. Phys. Lett.* **94**, 081907 (2009). [99](#)

- [143] B. Gallas, J. Rivory, H. Arwin, R. Magnusson, G. Guida, J. Yang, and K. Robbie (ICSE-V, Albany, NY, 2010). [99](#)
- [144] M. O. Jensen and M. J. Brett, *Opt. Express* **13**, 3348 (2005). [99](#)
- [145] I. Šolc, *J. Opt. Soc. Am.* **55**, 621 (1965). [99](#)
- [146] A. Lakhtakia and W. Weiglhofer, *Proc. R. Soc. Lond. A* **448**, 419 (1995). [99](#)
- [147] F. Chiadini and A. Lakhtakia, *Microw. Opt. Techn. Lett.* **42**, 135 (2004). [99](#)
- [148] P. I. Rovira, R. A. Yarussi, R. W. Collins, R. Messier, V. C. Venugopal, A. Lakhtakia, K. Robbie, and M. J. Brett, *Appl. Phys. Lett.* **71**, 1180 (1997). [100](#)
- [149] K. Robbie, D. J. Broer, and M. J. Brett, *Nature* **399**, 764 (1999). [100](#)
- [150] A. C. van Popta, J. C. Sit, and M. J. Brett, *Appl. Optics* **43**, 3632 (2004). [100](#)
- [151] J. B. Sorge, A. C. van Popta, J. C. Sit, and M. J. Brett, *Opt. Express* **14**, 10550 (2006). [100](#)
- [152] K. M. Krause and M. J. Brett, *Adv. Funct. Mater.* **18**, 3111 (2008). [100](#)
- [153] J. K. Gansel, M. Thiel, M. S. Rill, M. Decker, K. Bade, V. Saile, G. von Freymann, S. Linden, and M. Wegener, *Science* **325**, 1513 (2009). [100](#)
- [154] Y. Zong, Y. C. Shin, C. M. Kim, B. G. Lee, E. H. Kim, Y. J. Park, K. M. A. Sobahan, C. K. Hwangbo, Y. P. Lee, and T. G. Kim, *J. Mater. Res.* **23**, 2500 (2008). [100](#)
- [155] X. Chen and K. Jiang, *Nanotechnology* **19**, 215305 (2008). [100](#)
- [156] D. W. Flaherty, R. A. May, S. P. Berglund, K. J. Stevenson, and C. B. Mullins, *Chem. Mater.* **22**, 319 (2010). [100](#)
- [157] N. A. Luechinger, S. Loher, E. K. Athanassiou, R. N. Grass, and W. J. Stark, *Langmuir* **23**, 3473 (2005). [100](#)
- [158] G. Mertens, R. B. Wehrspohn, H.-S. Kitzerowa, S. Matthias, C. Jamois, and U. Gösele, *Appl. Phys. Lett.* **87**, 241108 (2005). [100](#)
- [159] M. Schubert, T. Hofmann, and C. M. Herzinger, *Thin Solid Films* **455-456**, 563 (2004). [101](#)

- 
- [160] R. M. Osgood, K. T. Riggs, A. E. Johnson, J. E. Mattson, C. H. Sowers, and S. D. Bader, *Phys. Rev. B* **56**, 2627 (1997). [103](#)
- [161] D. Weller, G. R. Harp, R. F. C. Farrow, A. Cebollada, and J. Sticht, *Phys. Rev. Lett.* **72**, 2097 (1994). [104](#)
- [162] A. K. Zvezdin and V. A. Kotov, *Modern Magneto-optics and Magneto-optical Materials* (IOP Publishing Ltd, Bristol, 1997). [104](#)
- [163] V. Kamberský, Z. Málek, Z. Frait, and M. Ondris, *Czech. J. Phys. B* **11**, 171 (1961). [107](#), [112](#)
- [164] K. Okamoto, T. Hashimoto, K. Hara, and E. Tatsumoto, *J. Phys. Soc. Jpn.* **31**, 1374 (1971). [107](#), [112](#)
- [165] J. S. Gau and C. F. Brucker, *J. Appl. Phys.* **57**, 3988 (1985). [107](#), [112](#)
- [166] J. S. Gau and W. E. Yetter, *J. Appl. Phys.* **61**, 3807 (1987). [107](#), [112](#)
- [167] A. Tasaki, K. Tagawa, and E. Kita, *Jpn. J. Appl. Phys.* **26**, 2037 (1987). [107](#), [112](#)
- [168] A. Westphalen, M.-S. Lee, A. Remhof, and H. Zabel, *Rev. Sci. Instrum.* **78**, 121301 (2007). [108](#)
- [169] D. J. Sellmyer, M. Zheng, and R. Skomski, *J. Phys.: Condens. Matter* **13**, R433 (2001). [112](#)
- [170] R. Skomski, *J. Phys.: Condens. Matter* **15**, R841 (2003). [112](#)
- [171] D. O. Smith, *J. Appl. Phys.* **30**, S264 (1959). [112](#)
- [172] T. G. Knorr and R. W. Hoffman, *Phys. Rev.* **113**, 1039 (1959). [112](#)
- [173] K. Okamoto, K. Itoh, and T. Hashimoto, *J. Mag. Mag. Mat.* **87**, 379 (1990). [112](#)
- [174] K. Okamoto and N. Miura, *IEEE T. Magn.* **MAG-20**, 1048 (1984). [112](#)
- [175] F. Tang, D.-L. Liu, D.-X. Ye, Y.-P. Zhao, T.-M. Lu, G.-C. Wang, and A. Vijayaraghavan, *J. Appl. Phys.* **93**, 4194 (2003). [112](#)
- [176] F. Liu, M. T. Umlor, L. Shen, J. Weston, W. Eads, J. A. Barnard, and G. J. Mankey, *J. Appl. Phys.* **85**, 5486 (1999). [112](#)

## List of Own Publications

- (1) D. Schmidt, E. Schubert, and M. Schubert, “*Generalized Ellipsometry Determination of Non-reciprocity in Chiral Silicon Sculptured Thin Films*”, Phys. Status Solidi (a) **205**, 748 (2008).
- (2) T. Hofmann, M. Schubert, D. Schmidt, and E. Schubert, “*Infrared behavior of aluminum nanostructure sculptured thin films*”, Mat. Res. Soc. Symp. Proc. **1080E**, 1080-O04-16 (2008).
- (3) D. Schmidt, B. Booso, T. Hofmann, E. Schubert, A. Sarangan, and M. Schubert, “*Monoclinic optical constants, birefringence, and dichroism of slanted titanium nanocolumns determined by generalized ellipsometry*”, Appl. Phys. Lett. **94**, 011914 (2009).
- (4) D. Schmidt, B. Booso, T. Hofmann, E. Schubert, A. Sarangan, and M. Schubert, “*Generalized ellipsometry for monoclinic absorbing materials: determination of optical constants of Cr columnar thin films*”, Opt. Lett. **34**, 992 (2009).
- (5) D. Schmidt, A. C. Kjerstad, T. Hofmann, R. Skomski, E. Schubert, and M. Schubert, “*Optical, structural, and magnetic properties of cobalt nanostructure thin films*”, J. Appl. Phys. **105**, 113508 (2009).
- (6) D. Schmidt, T. Hofmann, A. C. Kjerstad, M. Schubert, and E. Schubert, “*Optical and magnetic properties of Co nanostructure thin films*”, Mat. Res. Soc. Symp. Proc. **1142**, 1142-JJ09-04 (2009).
- (7) L. Makinistian, E.A. Albanesi, N.V. Gonzalez Lemus, A.G. Petukhov, D. Schmidt, E. Schubert, M. Schubert, Ya.B. Losovyj, P. Galiy, and P. Dowben, “*Ab-initio calculations and ellipsometry measurements of the optical properties of the layered semiconductor  $In_4Se_3$* ”, Phys. Rev. B **81**, 075217 (2010).
- (8) D. Schmidt, T. Hofmann, C. M. Herzinger, E. Schubert, and M. Schubert, “*Magneto-optical Properties of Cobalt Slanted Columnar Thin Films*”, Appl. Phys. Lett. **96**, 091906 (2010).

- (9) D. Schmidt, C. Müller, T. Hofmann, O. Inganäs, H. Arwin, E. Schubert, and M. Schubert, “*Optical properties of hybrid titanium chevron sculptured thin films coated with a semiconducting polymer*”, Thin Solid Films (*accepted for publication*).
- (10) D. Schmidt, T. Hofmann, E. Schubert, and M. Schubert, “*Magnetization Orientation Estimation in Transparent Ferromagnetic Cobalt Slanted Columnar Thin Films by Magneto-Optical Generalized Ellipsometry*”, Thin Solid Films (*in submission*).